Cell

The local microenvironment drives activation of neutrophils in human brain tumors

Graphical abstract

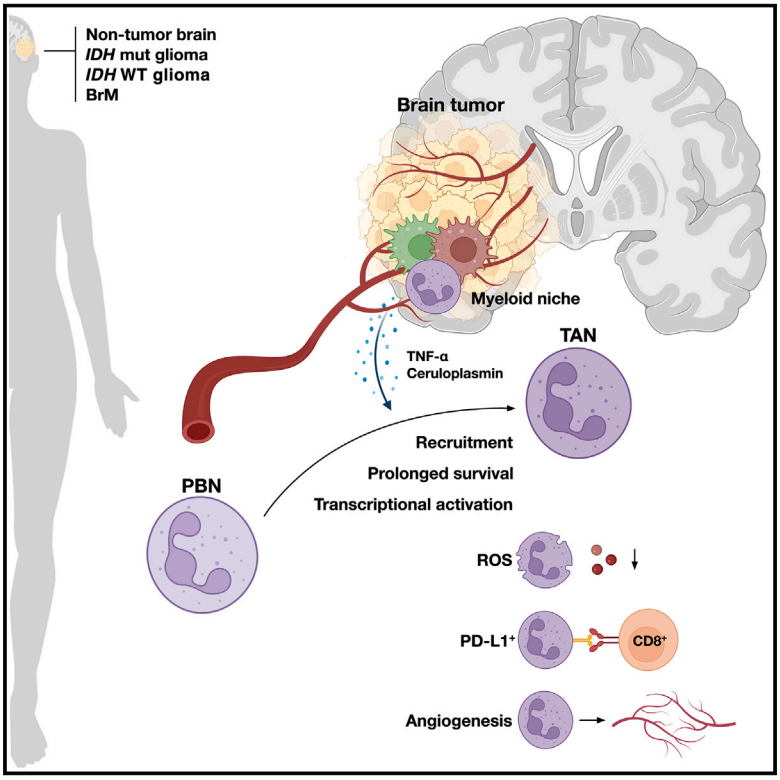

Highlights

- Neutrophils infiltrate human *IDH* WT gliomas and brain metastasis in substantial numbers
- Pro-inflammatory pathways are enriched in brain tumor-associated neutrophils (TANs)
- Brain TANs have a prolonged survival and immunosuppressive and pro-angiogenic phenotype
- TNF-α and Ceruloplasmin secreted by tumor-associated myeloid cells induce TAN phenotypes

Authors

Roeltje R. Maas, Klara Soukup, Nadine Fournier, ..., Roy T. Daniel, Monika E. Hegi, Johanna A. Joyce

Correspondence

johanna.joyce@unil.ch

In brief

Comprehensive analyses of brain tumor-associated neutrophils in humans and mice reveal a multifaceted pro-tumoral phenotype, which is induced by soluble factors secreted by tumor-associated myeloid cells.

Maas et al., 2023, Cell *186*, 4546–4566
October 12, 2023
https://doi.org/10.1016/j.cell.2023.08.043

CellPress

CellPress
OPEN ACCESS

Cell

Article

The local microenvironment drives activation of neutrophils in human brain tumors

Roeltje R. Maas,[1,2,3,4,5,6] Klara Soukup,[1,2,3] Nadine Fournier,[3,7,8,14] Matteo Massara,[1,2,3,4,14] Sabine Galland,[1,2,3,4,9] Mara Kornete,[1,2,3] Vladimir Wischnewski,[1,2,3,4] Joao Lourenco,[3,7] Davide Croci,[1,2,3] Ángel F. Álvarez-Prado,[1,2,3,4] Damien N. Marie,[1,2,3] Johanna Lilja,[1,2,3] Rachel Marcone,[3,7] Gabriel F. Calvo,[10] Rui Santalla Mendez,[1,2,3,4] Pauline Aubel,[1,2,3,4] Leire Bejarano,[1,2,3,4] Pratyaksha Wirapati,[3,8] Iván Ballesteros,[11] Andrés Hidalgo,[11,12] Andreas F. Hottinger,[1,2,3,9] Jean-Philippe Brouland,[13] Roy T. Daniel,[4,6] Monika E. Hegi,[4,5,6] and Johanna A. Joyce[1,2,3,4,15,*]

[1]Department of Oncology, University of Lausanne, Lausanne 1011, Switzerland
[2]Ludwig Institute for Cancer Research, University of Lausanne, Lausanne 1011, Switzerland
[3]Agora Cancer Research Centre Lausanne, Lausanne 1011, Switzerland
[4]L. Lundin and Family Brain Tumor Research Center, Departments of Oncology and Clinical Neurosciences, Centre Hospitalier Universitaire Vaudois, Lausanne 1011, Switzerland
[5]Neuroscience Research Center, Centre Hospitalier Universitaire Vaudois, Lausanne 1011, Switzerland
[6]Department of Neurosurgery, Centre Hospitalier Universitaire Vaudois, Lausanne 1011, Switzerland
[7]Translational Data Science Group, Swiss Institute of Bioinformatics, Lausanne 1011, Switzerland
[8]Bioinformatics Core Facility, Swiss Institute of Bioinformatics, Lausanne 1011, Switzerland
[9]Department of Oncology, Centre Hospitalier Universitaire Vaudois, Lausanne 1011, Switzerland
[10]Department of Mathematics & MOLAB-Mathematical Oncology Laboratory, University of Castilla-La Mancha, Ciudad Real 13071, Spain
[11]Program of Cardiovascular Regeneration, Centro Nacional de Investigaciones Cardiovasculares Carlos III, Madrid 28029, Spain
[12]Vascular Biology and Therapeutics Program and Department of Immunobiology, Yale University School of Medicine, New Haven, CT 06519, USA
[13]Department of Pathology, Centre Hospitalier Universitaire Vaudois, University of Lausanne, Lausanne 1011, Switzerland
[14]These authors contributed equally
[15]Lead contact
*Correspondence: johanna.joyce@unil.ch
https://doi.org/10.1016/j.cell.2023.08.043

SUMMARY

Neutrophils are abundant immune cells in the circulation and frequently infiltrate tumors in substantial numbers. However, their precise functions in different cancer types remain incompletely understood, including in the brain microenvironment. We therefore investigated neutrophils in tumor tissue of glioma and brain metastasis patients, with matched peripheral blood, and herein describe the first in-depth analysis of neutrophil phenotypes and functions in these tissues. Orthogonal profiling strategies in humans and mice revealed that brain tumor-associated neutrophils (TANs) differ significantly from blood neutrophils and have a prolonged lifespan and immune-suppressive and pro-angiogenic capacity. TANs exhibit a distinct inflammatory signature, driven by a combination of soluble inflammatory mediators including tumor necrosis factor alpha (TNF-α) and Ceruloplasmin, which is more pronounced in TANs from brain metastasis versus glioma. Myeloid cells, including tumor-associated macrophages, emerge at the core of this network of pro-inflammatory mediators, supporting the concept of a critical myeloid niche regulating overall immune suppression in human brain tumors.

INTRODUCTION

Central nervous system tumors comprise primary and metastatic malignancies and often confer a poor prognosis. Among primary brain tumors, diffuse gliomas represent the most aggressive types and are classified based on the occurrence of isocitrate dehydrogenase 1 and 2 (*IDH*) mutations.[1] *IDH* mutant (mut) tumors are generally low-grade gliomas, whereas *IDH* wild-type (WT) tumors represent high-grade aggressive glioblastomas (GBMs). Brain metastases (BrMs) are more frequent and originate predominantly from primary lung, breast, melanoma, and kidney tumors.[2] Prognosis following the current standard of care therapy remains poor,[3,4] and ongoing trials to identify new treatment strategies increasingly focus on immuno- and targeted therapies, which have shown some efficacy in a subset of BrMs but only very limited effects in gliomas.[5–7] The suboptimal efficacy of these treatments is likely driven in part by immune-suppressive mechanisms operating in the brain.[8]

The brain tumor microenvironment (TME) is a critical regulator of cancer progression and metastasis,[9] with unique cell types

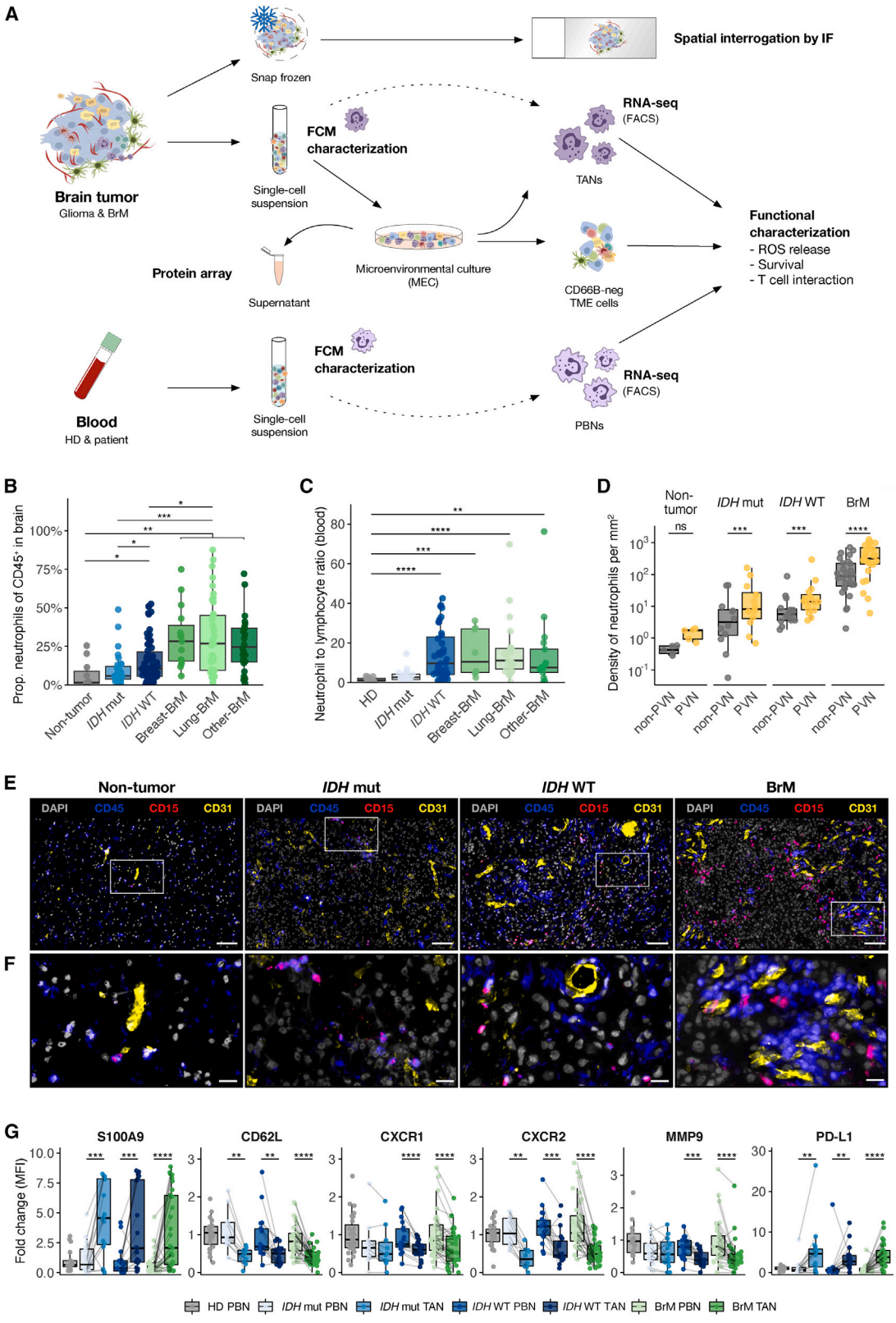

(legend on next page)

(e.g., microglia [MG], astrocytes, and neurons), a specialized immune composition,[10,11] and physiological regulation by the blood-brain barrier (BBB).[12] The overall tumor immune landscape of human gliomas and BrMs has been recently reported,[10,11] with a particular focus on analyzing MG and monocyte-derived macrophages (MDMs). Importantly, a substantial proportion of tumor-associated neutrophils (TANs) among brain-infiltrating immune cells was evident, specifically in human *IDH* WT gliomas and BrMs.[10]

However, to date, only a handful of studies have explored the roles of TANs in brain tumors, and mostly reported pro-tumoral roles in mouse models of gliomas[13–16] and BrM.[17,18] Given certain differences between mouse and human neutrophil biology,[19] a comprehensive and multifaceted investigation of TANs in human brain tumors is of critical importance and currently lacking. Moreover, considering the diversity of neutrophil functions in distinct organ environments, in both health[20] and disease,[21] an emphasis must be placed on understanding the contribution of TANs to each specific tumor type and stage.[22]

Here, we present the first in-depth analysis of neutrophils in patients with diverse brain malignancies. We identified commonalities and differences between neutrophils in blood vs. tumor tissue and determined how primary vs. metastatic brain TMEs co-opt these cells. We were thereby able to address the following questions: (1) what determines neutrophil abundance in human brain tumors, (2) where do TANs localize within the brain TME and which cell types do they interact with, and (3) how do specific tissue vs. tumor types dictate neutrophil phenotypes and functionalities.

RESULTS

Neutrophils are more abundant in human BrMs than primary gliomas and their phenotype is altered within the brain TME

In this study, we investigated whether neutrophils are altered by distinct brain TMEs in tumors of intracranial vs. extracranial origin. We analyzed freshly resected human glioma and BrMs, matched blood samples, and non-tumor brain tissue (epilepsy lobectomies) using a range of complementary approaches (flow cytometry [FCM], immunofluorescence [IF] staining for spatial TME analyses, RNA sequencing [RNA-seq], microenvironmental cultures [MECs], protein arrays, and various *ex vivo* functional assays) (Figure 1A). This allowed us to comprehensively interrogate the phenotype, transcriptome, and functionality of brain TANs and peripheral blood neutrophils (PBNs) for the first time.

Analysis of 192 human samples by FCM revealed a significant increase in relative TAN abundance in *IDH* WT gliomas and BrMs compared with *IDH* mut gliomas and non-tumor tissue, with the highest TAN proportions in BrMs (Figures 1B and S1A; Table S1A; methodology for detailed sample processing and gating strategy of different immune cell populations is described in Maas et al.[23]). Similarly, the blood neutrophil-to-lymphocyte ratio (NLR) was significantly higher in both *IDH* WT glioma and BrM patients vs. healthy donors (HDs; Figures 1C and S1B; Table S1A) and also elevated compared with *IDH* mut glioma patients. High NLR is associated with reduced patient survival in various cancer types including brain tumors.[24–27]

Considering the increased relative abundance of PBNs in *IDH* WT glioma and BrM patients, we investigated whether neutrophils infiltrate the tumor parenchyma or primarily remain within blood vessels in the brain TME. By employing IF staining of whole tissue sections, we analyzed neutrophil ($CD15^+$ $CD45^+$) localization relative to the vasculature ($CD31^+$) and demonstrated that neutrophils indeed penetrate the brain (tumor) tissue (Figures 1D–1F). Quantifying neutrophil proximity to blood vessels revealed that they localize at higher densities within the perivascular niche (PVN = within 20 μm distance of vessels) in brain tumor tissue (Figures 1D and S1C). Notably, BrMs exhibited the highest spatial TAN density (Figure 1D), confirming their overall elevated abundance as determined by FCM (Figure 1B).

Given the differential abundance of TANs between BrMs and gliomas, we next asked whether neutrophils were phenotypically altered (1) compared with HDs, (2) in different tissues (blood vs. tumors), and (3) in distinct brain tumor types (gliomas vs. BrMs). We first analyzed canonical neutrophil activation markers and functional molecules, previously reported to be differentially expressed by TANs in other tumors.[17,18,26,28–32] Using FCM, we found that brain TANs—independent of tumor type—exhibited a pronounced activation profile characterized by increased

Figure 1. Neutrophils are more abundant in the TME of human BrMs than primary gliomas and are phenotypically altered

(A) Experimental design and methodology for analysis of human brain tumor tissue and matched blood.

Abbreviations: BrM, brain metastasis; TANs, tumor-associated neutrophils; PBNs, peripheral blood neutrophils; IF, immunofluorescence; FCM, flow cytometry; RNA-seq, RNA sequencing; FACS, fluorescence-activated cell sorting; MEC, microenvironmental culture; TME, tumor microenvironment; ROS, reactive oxygen species; HD, healthy donor.

(B) Neutrophil proportion among $CD45^+$ immune cells in non-tumor ($n = 11$) and tumor tissue ($n_{IDH\ mut}$ glioma = 31, $n_{IDH\ WT}$ glioma = 70, $n_{Breast\text{-}BrM} = 15$, $n_{Lung\text{-}BrM} = 41$, $n_{Other\text{-}BrM} = 24$) using FCM. Wilcoxon rank-sum test.

(C) Neutrophil-to-lymphocyte ratio measured in whole blood from HD ($n = 12$) vs. brain tumor bearing patients ($n_{IDH\ mut} = 20$, $n_{IDH\ WT} = 43$, $n_{Breast\text{-}BrM} = 8$, $n_{Lung\text{-}BrM} = 25$, $n_{Other\text{-}BrM} = 17$). Wilcoxon rank-sum test.

(D) Density of neutrophils (per mm^2) in the non-perivascular niche (non-PVN) and PVN in non-tumor ($n = 5$) and tumor tissue ($n_{IDH\ mut} = 12$, $n_{IDH\ WT} = 15$, $n_{BrM} = 27$) using IF as shown in (E), (F), and Figure S1C. Wilcoxon signed-rank test.

(E and F) (E) Representative IF images of neutrophils ($CD45^+$, $CD15^+$) in relation to the vasculature ($CD31^+$) in non-tumor, *IDH* mut and WT glioma, and a lung-BrM. Scale bars: 100 μm, highlighted boxed areas are shown at higher magnification in (F). Scale bars: 20 μm.

(G) Fold-change median fluorescence intensity (MFI) in matched PBNs and TANs from tumor-bearing patients ($n_{IDH\ mut} > 10$, $n_{IDH\ WT} = 19$, $n_{BrM} > 31$) normalized to HD PBNs ($n > 14$). Wilcoxon signed-rank test, comparing matched patient PBNs and TANs only. Data in (B)–(D) and (G) are represented as mean ± SD and p.adj values: *$p < 0.05$, **$p < 0.01$, ***$p < 0.001$, ****$p < 0.0001$.

See also Figure S1 and Table S1A for clinical details.

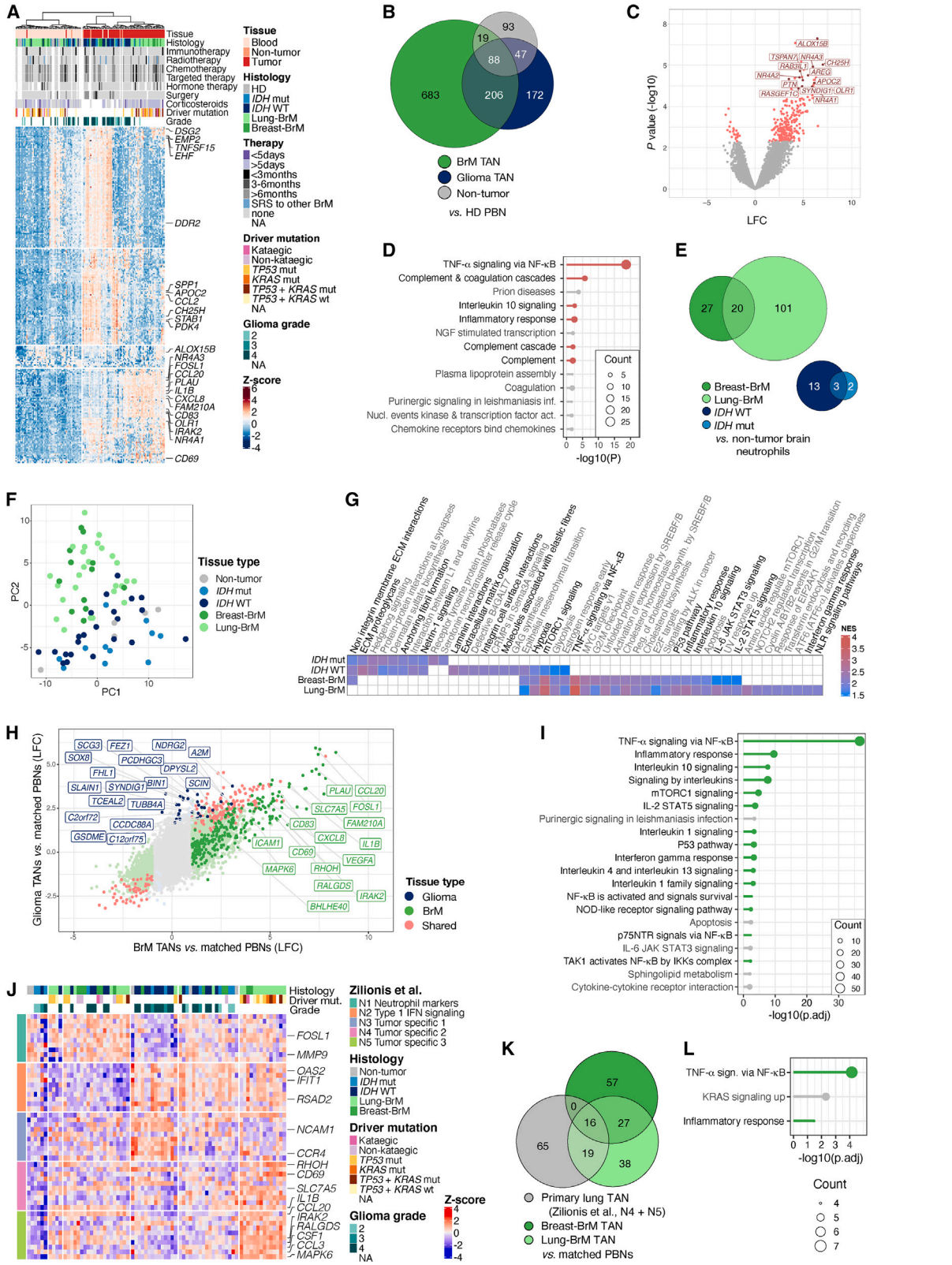

(legend on next page)

expression of CD11B, CD15, CD66B, and S100A9, and decreased expression of CD62L, in parallel with marked alterations in levels of the chemokine receptors CXCR1, CXCR2, and CXCR4, when compared with matched PBNs (Figures 1G and S1D). S100A9 was predominantly expressed by TANs (Figure S1E; IF analysis), and functionally, we observed lower intracellular levels of matrix metalloproteinase 9 (MMP9) and arginase 1 (Arg1) (Figures 1G and S1D), potentially indicating their secretion into the TME, as reported in other contexts.[33,34] TANs also expressed higher levels of programmed death-ligand 1 (PD-L1) (Figure 1G), which not only inhibits T cell[18] but can also delay neutrophil apoptosis.[33,35] While these specific markers exhibited some inter-individual variation, there were no marked differences between TANs in BrMs vs. glioma, nor in PBNs from patients vs. HDs (Figures 1G and S1D).

Brain neutrophils are enriched in inflammatory gene signatures, which become more pronounced in BrMs but not in gliomas

Considering these phenotypic differences, we next took an unsupervised approach to analyze the transcriptome of matched PBNs and TANs from brain tumor patients, PBNs from HD, and neutrophils from non-tumor brain tissue, each isolated by fluroescence-activated cell sorting (FACS) and then subjected to RNA-seq (Table S1B). Unsupervised clustering and principal-component analysis (PCA) revealed that TANs have a distinct transcriptional profile from PBNs (Figures 2A and S2A), while patient PBNs closely resemble HD PBNs. This broad separation was not influenced by treatment history, tumor grade, or mutational status (Figure 2A). Notably, in BrM patients only, specific alterations were observed in PBNs vs. HD PBNs (Figure S2B; Tables S2A and S2B), with a small subset of these changes also evident in the comparison of BrM TANs vs. HD PBNs (Figure S2C; Tables S2A and S2C). Over-representation analysis (ORA) revealed three significant pathways, all broadly related to inflammatory signaling, as shared between BrM PBNs and TANs vs. HD PBNs (Figure S2D; Table S2D).

While low in abundance, neutrophils in non-tumor brain tissue showed a substantially different transcriptional profile compared with HD PBNs, clustering with brain TANs (Figures 2A and S2A), with most differentially expressed genes (DEGs) overlapping with TANs (Figures 2B and S2E; Tables S2C, S2E, and S2F). Several genes elevated in non-tumor brain neutrophils vs. HD PBNs included those associated with altered metabolism (*OLR1/LOX1*, *ALOX15B*, *CH25H*, *AREG*, *PTN*, and *APOC2*) and multiple neurotrophic factors (*NR4A1*, *NR4A2*, *NR4A3*, *RAB3IL1*, *SYNDIG1*, *TSPAN7*, and *RASGEF1C*) (Figures 2C and S2F; Tables S2F and S2G). This signature thus likely reflects the adaptation of neutrophils to the molecular composition and nutrient availability in the brain. These findings, along with previous studies investigating neutrophil phenotypes in different tissues under homeostasis in mouse models,[20] underscore the contribution of distinct organ environments as a key determinant shaping the neutrophil transcriptome.

To assess which transcriptional alterations were shared between non-tumor brain neutrophils and brain TANs vs. HD PBNs (Figure 2B), ORA was performed, predominantly identifying inflammatory pathways (Figure 2D; Table S2H). When investigating the distinguishing features between brain TANs vs. non-tumor brain neutrophils, we found significantly more DEGs in breast- and lung-BrM TANs than in *IDH* mut and *IDH* WT glioma TANs, indicating that glioma TANs undergo few tumor-specific alterations (Figure 2E; Tables S3A–S3D). There was no overlap between BrM and glioma TANs regardless of mutational status (Figure 2E), which was corroborated by PCA (Figure 2F). While breast- and lung-BrM TANs were further enriched in inflammatory and immune-activation signaling pathways (Figure 2G; Tables S3E and S3F), *IDH* mut, and especially

Figure 2. Neutrophil transcription is altered within the brain tissue environment

(A) Unsupervised heatmap depicting the top 250 most variable neutrophil genes, genes of interest indicated on right.

(B) Euler diagram showing intersect of upregulated differentially expressed genes (DEGs) in BrM/glioma TANs, and non-tumor brain neutrophils vs. HD PBNs (cutoff: p.adj < 0.05 for TANs and p < 0.005 for non-tumor brain neutrophils; $\log_2$ fold-change (LFC) > 1).

(C) Volcano plot showing DEGs in non-tumor brain neutrophils vs. HD PBNs. Highlighted are neurotrophic and metabolic genes within the top 20 significantly upregulated genes.

(D) Over-representation analysis (ORA) of pathways from Hallmark, KEGG, and Reactome databases on upregulated DEGs shared between non-tumor brain neutrophils, glioma, and BrM TANs vs. HD PBNs (intersect shown in B). Pro-inflammatory pathways highlighted in red.

(E) Euler diagram depicting intersect of upregulated DEGs in lung-, breast-BrM, *IDH* WT, and *IDH* mut glioma TANs vs. non-tumor brain neutrophils (cutoff: p < 0.005; LFC > 1).

(F) PC plot of neutrophil transcriptional profiles in non-(tumor) brain tissue, calculated based on top 1% most highly variable genes.

(G) Gene set enrichment analysis (GSEA) using Hallmark and Reactome databases on DEGs in lung-, breast-BrM, *IDH* mut, and *IDH* WT glioma TANs vs. non-tumor brain neutrophils. (cutoff: p.adj < 0.05; NES > 2 in at least one of the tumor types). Highlighted are ECM and pro-inflammatory pathways.

(H) Dot plot depicting LFC of individual DEGs between BrM/glioma TANs vs. matched PBNs (cutoff: p.adj < 0.05). Highlighted are significant DEGs of interest in BrM vs. glioma TANs (cutoff: p.adj < 0.05; LFC > 1 or <−1; dark blue, signif. in glioma TANs vs. BrM TANs and glioma PBNs; light blue, signif. in glioma TANs vs. PBNs only; green, signif. in BrM TANs vs. glioma TANs and BrM PBNs; light green, signif. in BrM TANs vs. PBNs only, salmon pink, shared in glioma and BrM TANs).

(I) ORA of top 20 most significant pathways from Hallmark, KEGG, and Reactome databases on DEGs upregulated specifically in BrM-TANs depicted in (H) (cutoff: p.adj < 0.05; NES > 0). Pro-inflammatory pathways in green.

(J) Heatmap depicting non-tumor neutrophils and brain-TANs aligned to top 10 most variable genes per "N" neutrophil cluster as defined by Zilionis et al.[36] Samples were hierarchically clustered and genes of interest are shown on right.

(K) Euler diagram depicting intersect between the top 100 DEGs upregulated in lung- and breast-BrM TANs vs. matched PBNs and the Zilionis et al. dataset of primary lung cancer TANs vs. PBNs.

(L) ORA of significant pathways from Hallmark, KEGG, and Reactome databases on the 27 DEGs shared between breast- and lung-BrM TANs only, as shown in (K) (cutoff: p.adj < 0.05; NES > 0).

See also Figure S2 and Tables S1B, for clinical details, S2, and S3.

IDH WT TANs mostly exhibited increased extracellular matrix-related signatures (Figure 2G; Tables S3G and S3H).

We then extracted a core DEG signature distinguishing BrM from glioma TANs by intersecting DEGs identified from the comparison of BrM vs. glioma TANs (disease-specific alterations), with DEGs in TANs vs. matched PBNs (tissue-specific alterations). While only 30 genes were higher in glioma TANs, 247 genes were BrM TAN specific (Figures 2H, S2G, and S2H; Tables S3I and S3J) and again substantially enriched in pro-inflammatory signaling pathways, particularly tumor necrosis factor alpha (TNF-α) signaling (Figure 2I; Table S3K). While there is substantial overlap in DEGs between lung- and breast-BrM TANs (Figure 2E), their divergence is driven by the enrichment of cell-cycle-associated pathways in breast-BrM TANs and inflammatory signaling pathways in lung-BrM TANs (Figure S2I; Table S3L).

We next compared our data with publicly available single-cell RNA-seq (scRNA-seq) datasets of human TANs in primary lung cancer[36,37] and melanoma-BrM.[38] We found that gene expression signatures of pro-inflammatory and tumor-specific neutrophil clusters N4-5, as identified by Zilionis and colleagues in lung cancer,[36] were particularly enriched in lung-BrM TANs (Figure 2J; Table S3M), suggesting similarity between the microenvironments of primary lung cancer and lung-BrM. Similar observations were made by analyzing an independent lung-TAN scRNA-seq dataset[37] (Figure S2J; Table S3M). Comparison with the melanoma-BrM scRNA-seq dataset showed that glioma TANs are enriched in genes associated with interferon-responsive clusters (Figure S2K), whereas BrM TANs correspond to more pro-inflammatory interleukin (IL)-8- and calprotectin-high clusters (Figure S2K; Table S3M). This integration underscores the transcriptional heterogeneity of TANs not only between gliomas and BrMs with different grade and mutational background (Figures 2J, S2J, and S2K) but also within these tumor types, suggesting the presence of different subsets in each tissue.

To identify a unique BrM TAN signature, we compared the top 100 DEGs of breast- and lung-BrM TANs vs. matched PBNs with those from primary lung cancer TANs[36] (Figure 2K; Table S3N). Indeed, lung cancer TANs shared more similarities with lung-BrM vs. breast-BrM TANs (Figure 2K). ORA of 27 DEGs shared only between breast- and lung-BrM TANs (Figure 2K), revealed TNF-α signaling and broad pro-inflammatory signaling as significantly induced specifically in BrM TANs (Figure 2L; Table S3O). Moreover, TANs in BrMs with *TP53* or *KRAS* mutations were transcriptionally distinct from *TP53*/*KRAS*-WT BrMs and showed increased inflammatory signaling (Figure S2L; Tables S3P and S3Q). This suggests that distinct mutations in the cancer cells can transcriptionally imprint on TANs, either directly or through induced alterations in the TME.[39]

Together, these data show that in addition to the brain tissue environment, the local TME imprints a further layer of alterations onto TANs, which is more pronounced in BrMs compared with gliomas, and predominantly characterized by inflammatory signaling.

ROS release is elevated in circulating neutrophils from BrM-bearing patients and is abrogated within the brain TME

Considering the observed tissue and TME-specific alterations in brain TANs from patients, we further investigated their functional alterations using breast-BrM and GBM mouse models. These fully immunocompetent models closely reflect the increased TAN abundance observed in human tumors (Figure 3A), although the overall proportion is lower in murine brain tumors. Notably, the phenotype of TANs in BrMs and gliomas is similarly altered for those markers conserved between species (Figure 3B). We next examined the capacity of isolated murine PBNs and TANs to produce reactive oxygen species (ROS)—a hallmark property of activated neutrophils associated with cell killing,[40–42] mutagenesis,[21] and T cell suppression.[43,44] Interestingly, we found that BrM and GBM TANs produced less ROS compared with matched PBNs (Figure 3C).

Given certain differences in the murine and human neutrophil ROS pathway,[19] we sought to validate these findings in patient samples. In functional assays, we found that PBNs from BrM patients released more ROS compared with glioma and HD PBNs (Figures 3D, 3E, and S3A). Transcriptional analysis confirmed this result, as BrM PBNs (but not glioma PBNs) showed positive enrichment of ROS-associated pathways compared with HDs (Figure S3B). Notably, TANs isolated from glioma and BrM samples produced substantially less ROS vs. matched PBNs (Figure 3F), similar to our findings in mouse models. This effect was not influenced by prior treatment (Figure S3C). Consistently, at the transcriptional level, brain TANs show pronounced dysregulation of genes related to ROS production and oxidative homeostasis (Figure 3G). Expression of *NCF1*, *NCF2*, and *NCF4* (NADPH oxidase subunits) was decreased in TANs vs. PBNs, while constituents of potent antioxidant response mechanisms were induced (e.g., glutathione pathway members *GCLC*, *GCLM*, *GPX3*, *GPX8*; peroxiredoxins *PRDX1*, *PRDX2*, *PRDX4*; and superoxide dismutase subunits *SOD1*, *SOD2*, and *SOD3*) (Figure 3G). By contrast, non-tumor brain neutrophils expressed high levels of both pro- and anti-ROS-associated genes (Figure 3G), suggesting a modest ROS inhibitory potential of the healthy brain environment.

To examine the effect of the brain TME on neutrophil ROS levels *ex vivo*, we separated TANs ($CD66B^+$) from the rest of the TME (i.e., $CD66B^-$ cells) and found that ROS levels increased immediately (Figure 3H), indicating a partially reversible, transient component to the ROS impairment. Consequently, we found that TAN ROS release was significantly increased in response to phorbol 12-myristate 13-acetate (PMA), a potent driver of neutrophil ROS production, and this activation overcame the $CD66B^-$ TME-driven ROS inhibition (Figure 3H), albeit not to the same extent as for PBNs. To model PBN entry into the brain TME using *ex vivo* cultures, we co-incubated PBNs or TANs with the matched $CD66B^-$ TME, which confirmed an immediate and cell-ratio-dependent inhibition of ROS release (Figures 3H and S3D). In sum, these data show that the brain TME can counteract neutrophil ROS release. Given that ROS act as potent cytotoxic agents,[40–42] ROS neutralization may represent a fast-acting defense mechanism of the brain TME.

Spatial TME analyses reveal the association of TANs with $PD\text{-}1^+$ $CD8^+$ T cells and endothelial cells

We next assessed which cells of the brain TME can be modulated by TANs based on their spatial proximity. First, we addressed the potential effect of TANs on T cell function.

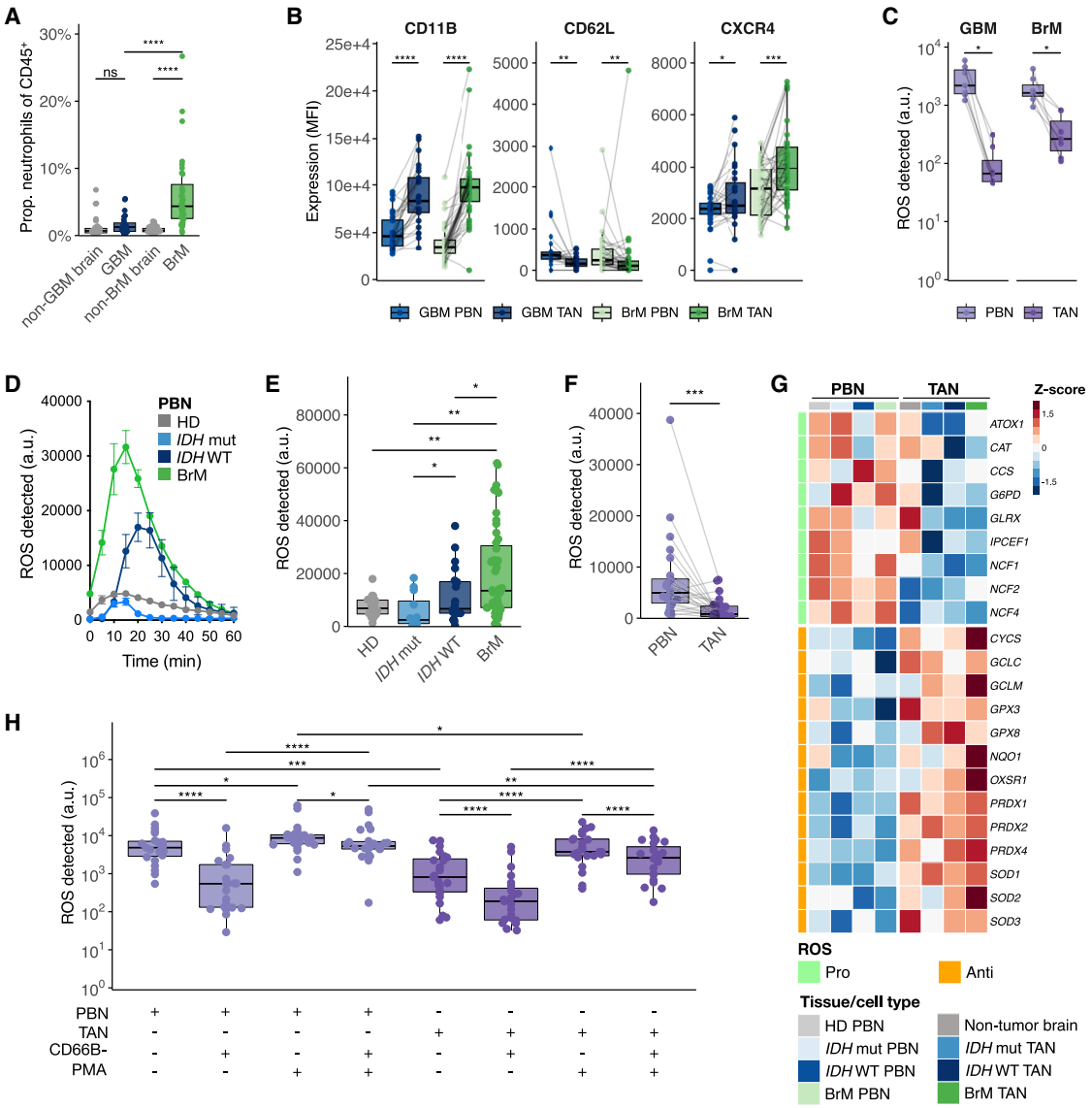

Figure 3. Murine brain TANs are phenotypically and functionally altered, as are human neutrophil ROS levels

(A) Proportion of Ly6G^{+} neutrophils of CD45^{+} immune cells in Ntv-a;iLy6G^{tdTomato} glioblastoma (GBM)$_{(n = 27)}$ and iLy6G^{tdTomato} BrM$_{(n = 40)}$ mouse models and non-tumor bearing mouse brain ($n_{non\text{-}GBM}$ = 27, $n_{non\text{-}BrM}$ = 39). Wilcoxon rank-sum test.

(B) MFI of indicated markers in Ntv-a;iLy6G^{tdTomato} GBM-bearing$_{(n = 27)}$ and iLy6G^{tdTomato} BrM-bearing$_{(n = 40)}$ mice. Wilcoxon signed-rank test.

(C) Detected ROS in arbitrary units (a.u.) in isolated PBNs and TANs in Ntv-a;iLy6G^{tdTomato} GBM-bearing$_{(n = 7)}$ and iLy6G^{tdTomato} BrM-bearing$_{(n = 7)}$ mice. Wilcoxon signed-rank test.

(D) Representative curves of ROS measured over time in PBNs from HD and brain tumor-bearing patients.

(E) Maximum ROS detected in PBNs from HD$_{(n = 18)}$, and tumor-bearing patients ($n_{IDH\ mut}$ = 12, $n_{IDH\ WT}$ = 20, n_{BrM} = 51). Wilcoxon rank-sum test.

(F) ROS detected in matched PBNs and TANs ($n_{IDH\ mut}$ = 6, $n_{IDH\ WT}$ = 9, n_{BrM} = 9). Wilcoxon signed-rank test.

(G) Heatmap depicting ROS-related significant DEGs in BrM and glioma TANs vs. matched PBNs.

(H) ROS detected in cocultures of matched PBNs and TANs with CD66B^{-} TME, activation by phorbol 12-myristate 13-acetate (PMA) ($n_{IDH\ mut}$ = 6, $n_{IDH\ WT}$ = 8, n_{BrM} = 9). Wilcoxon signed-rank test. Data in (A)–(F) and (H) are represented as mean ± SD. p.adj values in (A), (B), (E), and (H): *p < 0.05, **p < 0.01, ***p < 0.001, ****p < 0.0001. p values in (C) and (F): *p < 0.05, ***p < 0.001.

See also Figure S3.

Notably, in early-stage lung cancer, TANs show antigen-presenting capacity.[45] However, only few brain TANs express antigen presentation molecules (e.g., HLA-ABC, HLA-DR, CD80, and CD86) (Figure 4A), similar to matched PBNs (Figure S4A), and significantly lower compared with MG and MDMs (Figure 4A). We also measured CD3^{+} T cell cytokine production in coculture with PBNs or TANs and found no change in secretion of cytotoxic mediators (Figures 4B and S4B), suggesting that

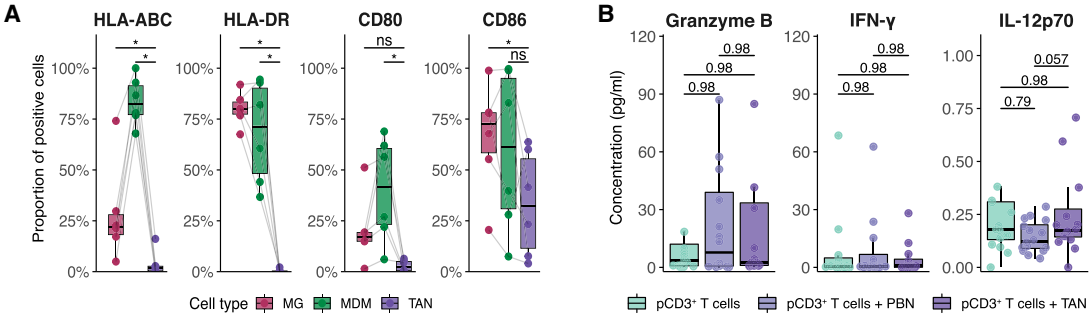

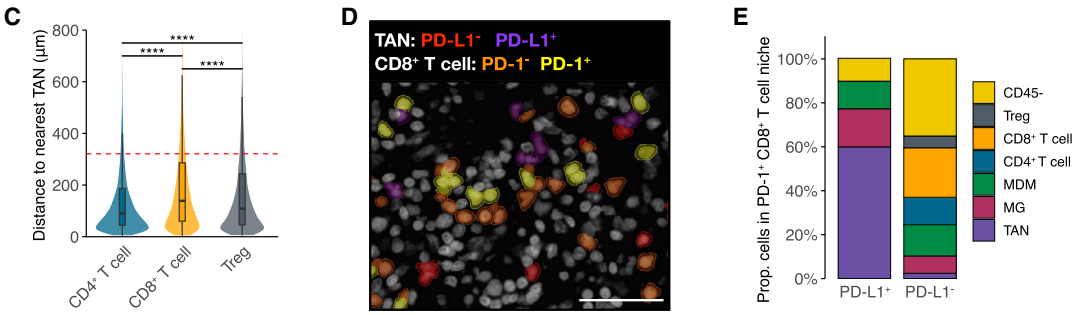

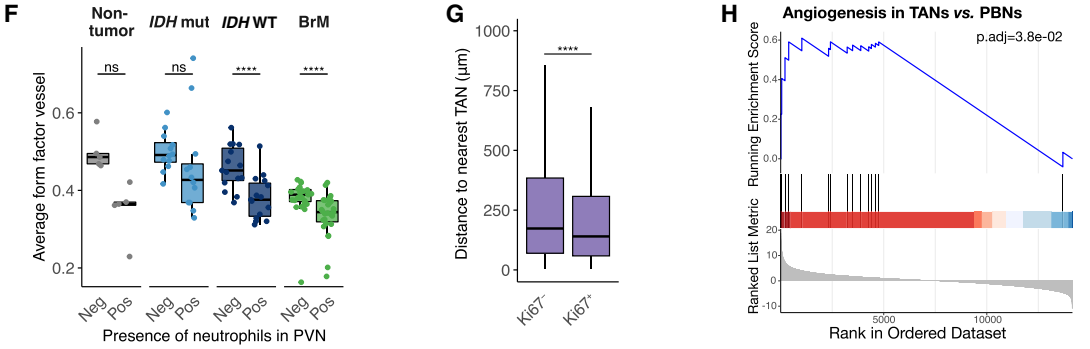

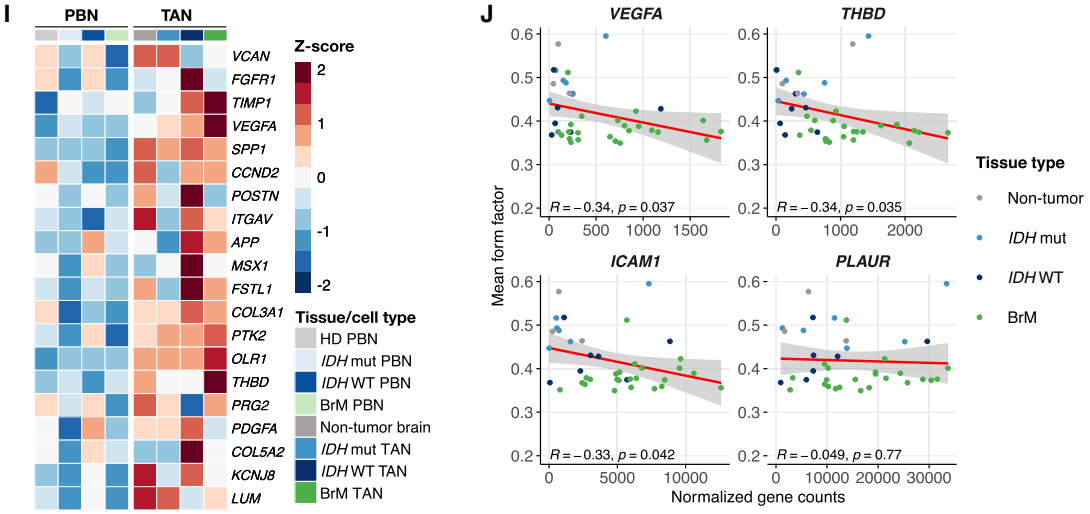

(legend on next page)

brain TANs do not alter CD3$^+$ T cell cytokine secretion, at least in the *ex vivo* setting. However, given that TANs show increased PD-L1 expression (Figure 1G), we also investigated the spatial relationship of TANs and T cells *in situ* using sequential IF. Interrogating *IDH* WT gliomas and BrMs, we found that CD4$^+$ T helper cells, Tregs, and CD8$^+$ T cells are in closer proximity to TANs compared with the average distance of all TME cells to this population (Figure 4C, indicated by the red line, $p < 0.0001$; Figure S4C). Since cell proximity is only suggestive of potential interactions, we also assessed the expression of programmed cell death protein 1 (PD-1) on CD8$^+$ T cells and PD-L1 on TANs. This revealed that PD-L1$^+$ TANs (~52% of TANs, based on IF) are located closest to PD-1$^+$ CD8$^+$ T cells (Figures 4D, S4D, and S4E), and the most abundant PD-L1$^+$ cell type within the PD-1$^+$ CD8$^+$ T cell niche is indeed TANs (Figure 4E). This suggests that TANs may have an immunosuppressive function in the brain TME.

Considering the contributions of neutrophils to angiogenesis regulation in tumors,[46] as well as healthy[47] and inflammatory brain tissue,[48,49] and that TANs reside proximal to the vasculature (Figure 1D), we investigated the relationship between TANs and vessels. We first characterized vessels stratified by the presence of TANs in the PVN, based on the following measurements: (1) form factor, indicating their degree of circularity (Figure S4F), (2) size, and (3) proliferation. As described in other contexts, larger and more deformed vessels (with a form factor < 1) can be less functional and leakier.[50,51] Especially in the brain, where the BBB tightly regulates molecular and cellular transport under homeostatic conditions, the development of leaky vessels can substantially impact the influx of cells.[52] Notably, we found that vessel form factor decreases in *IDH* WT gliomas and BrMs, especially in those vessels containing TANs within their PVN (Figures 4F and S4G). Moreover, TANs, irrespective of brain tumor type, localized preferentially within the PVN of larger vessels (Figure S4H), and in closer proximity to proliferating endothelial cells (Figure 4G).

Additionally, we found significant enrichment of the Hallmark angiogenesis pathway in both glioma and BrM TANs vs. matched PBNs (Figures 4H and 4I). Expression of various pro-angiogenic genes (e.g., *VEGFA, THBD*, and *ICAM1*) was higher in TANs compared with other TME populations (Figure S4I). Several pro-angiogenic factors were also upregulated in non-tumor brain neutrophils, albeit not to the same extent as in *IDH* WT and BrM TANs (Figure 4I). This corresponds with the enrichment of angiogenesis pathways in non-tumor brain neutrophils vs. HD PBNs (Figure S2F). At the protein level, we found that the angiogenesis-associated factor S100A9[53] was enriched in TANs vs. PBNs (Figures 1G and S1E). MMP9, an important VEGF-associated pro-angiogenic metalloprotease,[54] was detected at lower protein levels (Figure 1G), potentially indicating its extracellular release. Notably, *MMP9* mRNA levels were highly elevated in TANs compared with other TME populations, designating TANs as a major MMP9 source in brain tumors (Figure S4I). Moreover, we revealed a significant correlation between vessel deformity (lower form factor) and the expression levels of several pro-angiogenic genes in TANs (Figure 4J), MG, and MDMs (Figure S4J). Together, these findings support important roles for the myeloid compartment in promoting aberrant angiogenesis in gliomas and BrMs, and potentially via distinct pathways in each specific myeloid cell population.

The brain TME has both transient and permanent effects on neutrophils and extends their lifespan

Given the pronounced phenotypic and transcriptional alterations we observed in brain TANs compared with PBNs, and their potential immunosuppressive and pro-angiogenic functions, we considered it critical to assess their longevity and transit time in the brain TME. While neutrophils are generally short-lived cells, a recent study revealed that murine neutrophils in certain organs have a substantially longer half-life/transit time than in blood.[20] Indeed, we found that isolated murine breast-BrM TANs show significantly prolonged survival compared with matched PBNs in culture (Figure 5A). Considering the limitations of assessing neutrophil lifespan *ex vivo*, we next utilized a neutrophil fate-mapping mouse line (iLy6G^{tdTomato})[20] to investigate decay *in vivo*; the first time this has been applied to preclinical cancer models. In both BrM and GBM, we indeed observed a trend toward longer mean lifetimes of brain TANs compared with healthy brain neutrophils (Figures 5B and 5C). Notably, among BrM and GBM TANs, a subset of neutrophils showed a further prolonged maximum lifespan, indicating that a larger fraction of aged neutrophils may persist within the brain tumor

Figure 4. Brain TANs colocalize with PD-1$^+$ CD8$^+$ T cells and the vasculature

(A) Proportion of cells expressing antigen presentation molecules in matched MDMs, MG, and TANs ($n_{IDH\ WT} = 4$, $n_{BrM} = 2$). Wilcoxon signed-rank test.

(B) Cytokine concentration (pg/mL) in coculture supernatant of peripheral CD3$^+$ T cells (pCD3) with PBNs/TANs for 96 h ($n_{IDH\ mut} = 2$, $n_{IDH\ WT} = 8$, $n_{BrM} = 6$). Wilcoxon signed-rank test, p.adj values as shown.

(C) Distance of individual T cells (CD4$^+$ T cells$_{(n = 53,692)}$, CD8$^+$ T cells$_{(n = 54,495)}$, Treg$_{(n = 26,001)}$) to the nearest TAN in BrM$_{(n = 20)}$ and *IDH* WT glioma$_{(n = 7)}$. Dashed line indicates average distance of all cells$_{(n = 2,571,834)}$ to the nearest TAN. Wilcoxon rank-sum test.

(D) Representative lung-BrM image showing IF cell type quantification of TANs (PD-L1$^-$/PD-L1$^+$) and CD8$^+$ T cells (PD-1$^-$/PD-1$^+$). Scale bars: 50 μm.

(E) Mean proportion of cell types identified in 20 μm radius around PD-1$^+$ CD8$^+$ T cells$_{(n = 20,697)}$ in BrM$_{(n = 20)}$ and *IDH* WT glioma$_{(n = 7)}$.

(F) Mean form factor of individual vessels in presence (Pos) or absence (Neg) of neutrophils in their PVN, based on IF as shown in Figures 1E and 1F ($n_{Non\text{-}tumor} = 5$, $n_{IDH\ mut} = 12$, $n_{IDH\ WT} = 15$, $n_{BrM} = 27$). Wilcoxon signed-rank test.

(G) Distance (μm) of Ki67$^-_{(n = 191,077)}$ and Ki67$^+_{(n = 14,718)}$ endothelial cells to the nearest TAN ($n_{IDH\ WT} = 7$, $n_{BrM} = 20$). Wilcoxon rank-sum test, p value: ****$p < 0.0001$.

(H) GSEA of Hallmark angiogenesis pathway in glioma and BrM TANs combined, compared with matched PBNs.

(I) Heatmap of individual genes from leading-edge Hallmark angiogenesis pathway stratified by brain tissue type and PBN/TAN.

(J) Correlation between mean vessel form factor vs. normalized gene counts of angiogenesis-associated genes in brain (tumor) neutrophils ($n_{non\text{-}tumor} = 3$, $n_{IDH\ mut} = 6$, $n_{IDH\ WT} = 7$, $n_{BrM} = 23$) using the Pearson method. Data in (A)–(C), (F), and (G) are represented as mean ± SD, p.adj value in (A), (C), and (F): *$p < 0.05$, ****$p < 0.0001$.

See also Figure S4.

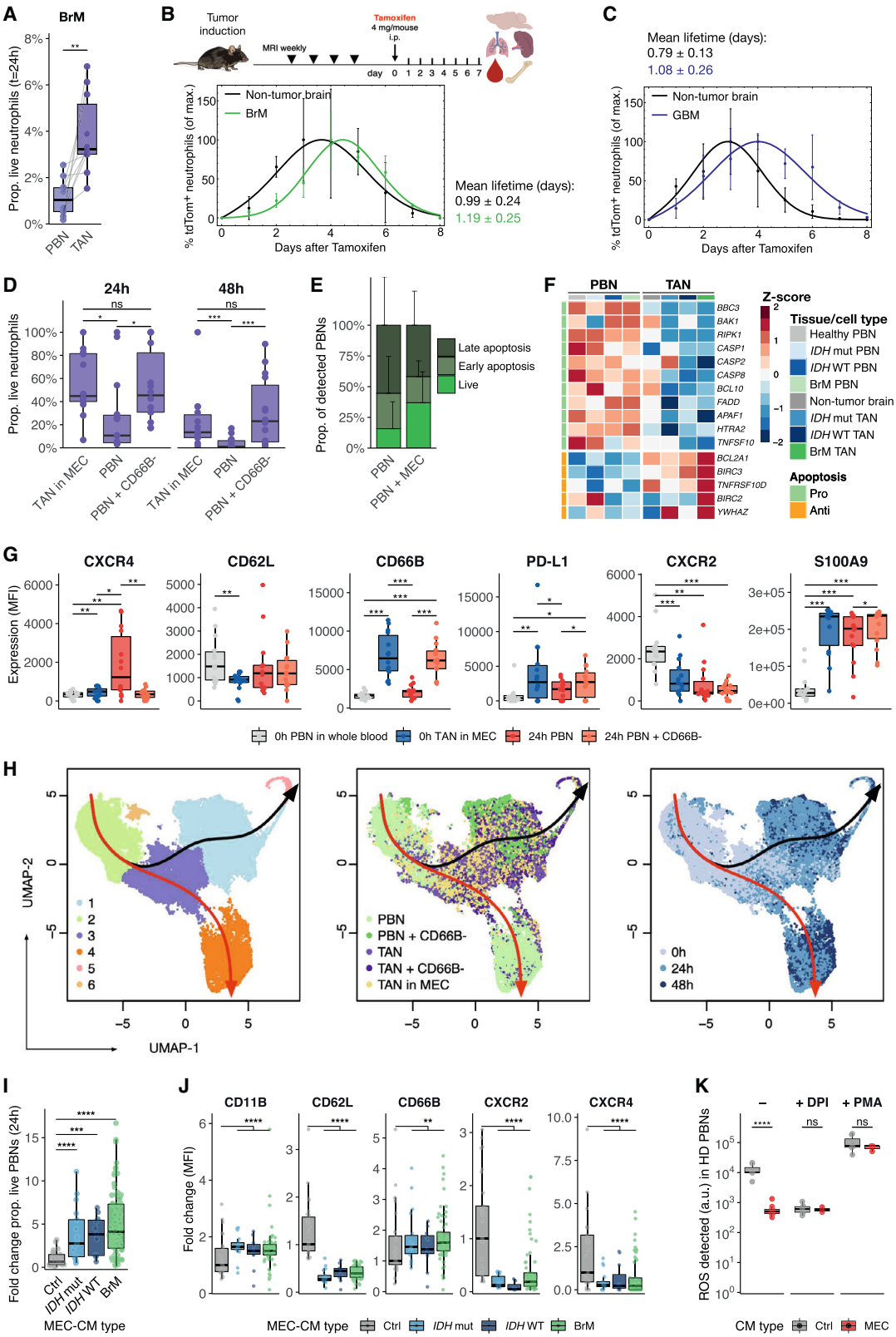

(legend on next page)

niche (Figure S5A). Importantly, TAN lifespan was similarly prolonged in primary mammary fat pad TANs (Figure S5B), and the presence of a growing tumor did not alter neutrophil lifespan in any of the peripheral organs assessed, including blood (Figure S5C).

Next, we analyzed the longevity of human TANs, by isolating and culturing these cells in tumor MECs *ex vivo* over time. We observed that up to 80% of TANs survive for 24 h, and up to 20% remain alive even after 48 h, which was similar across all brain tumor types and independent of treatment history (Figures 5D, S5D, and S5E). As expected, considerably fewer viable PBNs remain at 24 h and almost all PBNs die within 48 h (Figures 5D and S5D). Notably, PBNs cultured within the CD66B$^-$ TME exhibited significantly increased survival, reaching a similar level to TANs (Figure 5D), indicating that the TME indeed prolongs neutrophil longevity. Critically, separating TANs from the TME milieu abrogated this longevity effect (Figure S5F), underscoring the importance of TME-supplied factors.

Neutrophils are continuously released from the bone marrow in vast numbers[55–57]; thus, programmed cell death is critical for maintaining homeostasis. We therefore assessed PBN life cycle stage at 24 h, via annexin V/DAPI staining. This showed that PBNs cultured within TME MECs remain alive/pre-apoptotic for longer compared with PBNs cultured alone (Figure 5E). Corroborating these findings, a pronounced number of pro-apoptotic genes were downregulated in TANs vs. PBNs in both BrMs and gliomas, and conversely, several anti-apoptotic genes were induced especially in BrM-TANs (Figure 5F). Non-tumor brain neutrophils showed an intermediate phenotype between PBNs and TANs, suggesting that the brain environment itself already influences apoptosis pathways in neutrophils (Figure 5F).

Having discovered that the brain-TAN phenotype, ROS production, and lifespan are altered in both patients and mouse models, we next queried how the brain TME induces these changes. Culturing patient PBNs for 24 h within the CD66B$^-$ TME broadly recapitulated the TAN phenotype (Figure 5G). While some alterations were induced in 24-h-old PBNs independent of the presence of the TME (e.g., CD62L, CXCR4, CXCR2, and S100A9), others were modulated only upon incubation within the TME cultures (e.g., CD66B and PD-L1) (Figure 5G). TANs maintain certain phenotypic alterations even when isolated from the TME (Figure S5G). The time-sensitive transition of PBNs to TANs was further confirmed through an unbiased approach. Trajectory analysis on single cells analyzed for 10 TAN phenotype markers (by FCM) demonstrated that PBNs cultured for 24 h in CD66B$^-$ TME converge with TANs (Figure 5H, black arrows), while PBNs cultured alone follow a separate trajectory (red arrows).

Notably, both increased longevity and TAN phenotypes were also induced in HD PBNs when cultured in the presence of conditioned media (CM) from 24 h MECs isolated from different brain tumors (Figures 5I and 5J; Table S1C for clinical information associated with these MEC). In addition, BrM-MEC-CM suppressed PBN-released ROS to a similar extent as diphenyleneiodonium (DPI), a ROS inhibitor (Figure 5K). This effect was reversed by the addition of PMA (Figure 5K). Similar findings regarding suppression of ROS (Figure S5H) and prolonged neutrophil survival (Figure S5I) were obtained for murine PBNs when cultured in MEC-CM derived from breast-BrM or GBM mouse models. Together this implicates soluble factors as the main mediators of these processes, which are conserved between human and mouse. It is furthermore indicative of combined mechanisms of transitory and permanent alterations, which appear partially linked to the persistence of neutrophils in the brain TME.

MEC-derived secreted factors modulate TAN phenotype and lifespan

We next asked which soluble factors are the major drivers of these alterations and began by assessing tumor cells. We derived cell lines from the patient MECs, which were confirmed by whole exome sequencing analysis to represent tumor cells (Figures S6A and S6B). These lines thus enabled an analysis of the effect of soluble factors released exclusively by tumor cells on neutrophils. Surprisingly, when culturing HD PBNs in CM from tumor cell lines (termed TCM), we did not detect any lifespan extension, in contrast to the matched MEC-CM (Figure 6A; Table S1C for clinical information associated with MEC-CM and TCM). We therefore assessed whether CM derived from various

Figure 5. The brain TME modulates both neutrophil survival and phenotype

(A) Proportion of live neutrophils after 24 h based on annexin V viability staining in BrM-bearing$_{(n\ =\ 10)}$ mice. Wilcoxon signed-rank test, p value: **p < 0.01.

(B) Experimental design showing iLy6G^{tdTomato} mice and proportion of tdTomato$^+$ neutrophils normalized to maximum in non-tumor and BrM-bearing mouse brains over 8 days. A minimum of 3 mice from 6 independent experiments are shown per time point, mean lifetime in days is shown on right.

(C) Proportion of tdTomato$^+$ neutrophils normalized to maximum in Ntv-a;iLy6G^{tdTomato} non-tumor and GBM-bearing mouse brains. Minimum of 3 mice from 3 independent experiments are shown per time point, mean lifetime in days is shown on top.

(D) Proportion of live TANs in tumors, matched PBNs and PBNs in coculture with CD66B$^-$ TME population at 24 and 48 h ($n_{IDH\ mut}$ = 5, $n_{IDH\ WT}$ = 5, n_{BrM} = 4). Wilcoxon signed-rank test.

(E) Proportion of PBNs at different viability stages, alone and in cocultures with matched MEC ($n_{IDH\ mut}$ = 2, $n_{IDH\ WT}$ = 2, n_{BrM} = 5).

(F) Heatmap of DEGs associated with apoptosis in PBNs vs. neutrophils from brain (tumor) tissue.

(G) MFI of phenotypic markers in PBNs over time (0 and 24 h) and in the presence of CD66B$^-$ TME ($n_{IDH\ mut}$ = 4, $n_{IDH\ WT}$ = 5, n_{BrM} = 5). Wilcoxon signed-rank test.

(H) Uniform manifold approximation and projection of 10-marker FCM panel (CD11B, CD15, CD16, CD45, CD54, CD62L, CD66B, CXCR1, CXCR2, and CXCR4) on matched TANs and PBNs in coculture with CD66B$^-$ TME over 48 h. Trajectories shown based on Slingshot: red arrow; PBN-trajectory, black arrow; TAN-trajectory.

(I) Fold-change in 24 h survival of HD PBNs (n = 25) after culture in MEC-CM ($n_{IDH\ mut}$ = 4, $n_{IDH\ WT}$ = 4, n_{BrM} = 15). Mixed effects model with MEC type as fixed effect and HD ID as random slope effect: ANOVA p value = 4.12×10^{-8}.

(J) Fold-change MFI in HD PBN (n = 15) cultured in MEC-CM ($n_{IDH\ mut}$ = 4, $n_{IDH\ WT}$ = 4, n_{BrM} = 14) vs. control medium. Mixed effect model as in (I).

(K) ROS measured in HD PBNs (n = 7) cultured in BrM MEC-CM (n = 13) and treated with diphenyleneiodonium (DPI) or PMA. Wilcoxon rank-sum test. Data in (A)–(E), (G), and (I)–(K) are represented as mean ± SD. p.adj values in (D), (G), and (I)–(K): *p < 0.05, **p < 0.01, ***p < 0.001, ****p < 0.0001.

See also Figure S5 and Table S1C for clinical information.

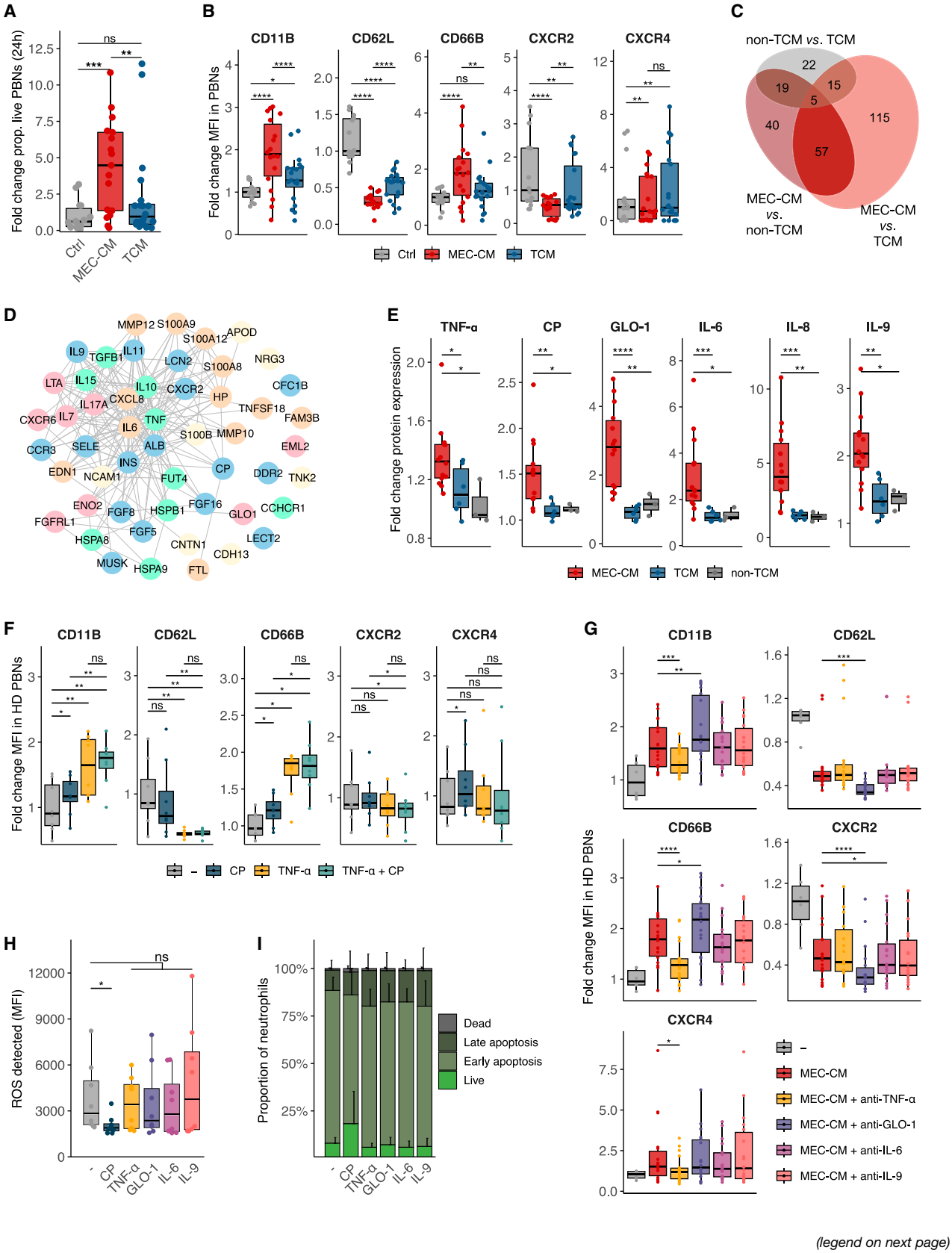

(legend on next page)

normal cell types including human brain microvascular endothelial cells (HBMECs), human umbilical vein endothelial cells (HUVECs), astrocytes (HAs), and *in vitro*-derived unpolarized HD MDMs (collectively referred to as non-TCM), confer the capacity to prolong neutrophil survival. Interestingly, only HBMEC-CM induced prolonged neutrophil lifespan to some extent, indicating that this is in part a brain endothelial-specific effect (Figure S6C). Furthermore, neither TCM nor any of the non-TCM recapitulated the complete phenotypic transition of neutrophils induced by the complete MEC-CM (Figures 6B and S6D). However, it is important to note that these tumor-naive cell lines and *in vitro*-derived MDMs can be transcriptionally distinct from their brain-tumor-associated counterparts, as previously shown for MDMs.[10] Taken together, these results indicate that factors produced by brain microenvironment-educated populations, rather than by tumor cells (alone), drive the observed neutrophil alterations.

To identify such factors, we performed a 1,000-protein array analysis on a panel of 24 h MEC-CM ($n_{IDH\ mut}$ = 2, $n_{IDH\ WT}$ = 3, n_{BrM} = 9), matched TCM ($n_{IDH\ mut}$ = 1, $n_{IDH\ WT}$ = 3, n_{BrM} = 2), and non-TCM (HBMEC, HA, and MDM) compared with media alone (control). Unsupervised clustering analysis showed that MEC-CM overall clustered separately from TCM, non-TCM, and control media, except for one outlier (Figure S6E). Most BrM-MEC clustered closely together, with some distinction from glioma-MEC. Subsetting for upregulated protein expression vs. control, and significant differential expression between CM types, revealed 57 MEC-specific proteins (Figure 6C). Of these, 51 were enriched in MEC-CM compared with both TCM and non-TCM (Figure S6F; Tables S4A–S4C), thereby representing potential drivers of the TAN alterations.

Applying interaction network analysis to these MEC-specific upregulated proteins revealed several clusters, centered on a highly interconnected pro-inflammatory cytokine group (Figure 6D). TNF-α, a potent recruiter and activator of neutrophils,[58,59] is positioned at the core of this cluster (Figures 6D and 6E). We also detected Ceruloplasmin (CP), Glyoxalase 1 (GLO-1), and IL-9 at high levels in MEC-CM (Figures 6D and 6E), which are important regulators of reduced ROS production[60–62] and prolonged neutrophil lifespan.[63] Additionally, we found high levels of major neutrophil chemoattractants IL-6[64] and IL-8[65] in MEC-CM specifically (Figures 6D and 6E).

Notably, we showed that when HD PBNs were exposed to TNF-α, this resulted in a more TAN-like phenotype compared with their untreated counterparts, including CD11B/CD66B upregulation and CD62L shedding, but no alterations in CXCR2/CXCR4 levels (Figure 6F). Moreover, TNF-α signaling was enriched in the brain neutrophil-specific signature (Figure 2D), in BrM and glioma TANs vs. matched PBNs (Figure S6G), and even more pronounced in BrM-TANs vs. gliomas (Figure 2I). Consequently, TNF-α inhibition in MEC-CM partially reversed the TAN-like phenotype by suppressing CD11B/CD66B expression, whereas other inhibitors of pro-inflammatory signaling did not convey such an effect, or even exacerbated it (Figure 6G). CP was the only other soluble factor identified that was similarly able to induce a partial TAN-like phenotype, with increased CD11B/CD66B (Figures 6F and S6H). Combined treatment with TNF-α and CP further increased the TAN-like phenotype, with significant reduction in CXCR2 expression (Figure 6F). Regarding the functional alterations observed in TANs, we found decreased ROS levels in HD PBNs following CP exposure (Figure 6H). Similarly, the proportion of live PBNs increased when incubated with CP (Figure 6I), mimicking the observations made in TANs vs. PBNs *in situ*. Other MEC-CM specific soluble factors (e.g., GLO-1, IL-6, IL-9, and TNF-α) did not confer such functional alterations (Figures 6H and 6I).

In sum, key aspects of the phenotypic and functional alterations in the PBN-to-TAN transition were induced by TNF-α and CP treatment, alone or in combination (Figures 6F, 6H, and 6I), indicating that multiple factors are required to drive the full TAN phenotype.

Neutrophils interact predominantly with the myeloid compartment

Lastly, we investigated which cell populations drive these alterations in TAN phenotype and function. First, we characterized the cellular composition of *ex vivo* MEC. At 24 h, $CD45^-$ cells, and all major immune populations were still present (Figures 7A and 7B), with a gradual reduction in absolute cell counts that was more pronounced for $CD45^-$ cells, MG and MDMs vs. $CD4^+$ and $CD8^+$ T cells (Figure S7A)—but overall indicating that all populations can potentially contribute to the effects observed *in situ* and upon exposure of PBNs to MEC-CM *ex vivo*.

Second, we analyzed our brain TME RNA-seq data to identify which cell types produce these MEC-CM-specific factors (Figure 6D). This revealed the myeloid compartment, including MDMs, MG, and TANs themselves, as the highest expressers of most MEC-specific pro-inflammatory cytokines (Figure 7C).

Figure 6. Neutrophil alterations are induced by soluble factors in the brain TME

(A) Fold-change in HD PBN survival (n = 12) after culture in MEC- or matched tumor cell line CM (TCM, $n_{IDH\ mut}$ = 1, $n_{IDH\ WT}$ = 3, $n_{melanoma\text{-}BrM}$ = 2) vs. control medium pooled from 6 independent experiments. Mixed-effect model with CM type as fixed effect and HD ID as random slope effect: ANOVA p value = 0.0011.

(B) Fold-change MFI of indicated markers in HD PBNs. Mixed effect model as in (A).

(C) Euler plot depicting overlap in differentially detected proteins (cutoff: $p < 0.05$) between MEC-CM, TCM, and non-TCM.

(D) Protein interaction network of the 51 differentially expressed proteins in MEC-CM vs. TCM and non-TCM. Color codes based on the unbiased clustering of protein pathways shown in Figure 7C.

(E) Detection of the proteins indicated (a.u.) normalized to control media. Wilcoxon rank-sum test.

(F) Fold-change MFI of indicated markers measured in HD PBNs (n = 8) treated with TNF-α and/or CP. Wilcoxon signed-rank test.

(G) Fold-change MFI of the indicated proteins in HD PBNs (n = 6) cultured in MEC-CM (n = 3) and the indicated inhibitors. Wilcoxon signed-rank test.

(H) ROS detected (MFI) in HD PBNs (n = 10) treated with MEC-CM specific mediators. Wilcoxon signed-rank test, p value: *p < 0.05.

(I) Proportion of PBNs (n = 10) at different viability stages after treatment with MEC-CM specific soluble factors.

Data in (A), (B), and (E)–(I) are represented as mean ± SD. p.adj values in (A), (B), and (E)–(G): *p < 0.05, **p < 0.01, ***p < 0.001, ****p < 0.0001.

See also Figure S6 and Tables S1C, for clinical information and S4.

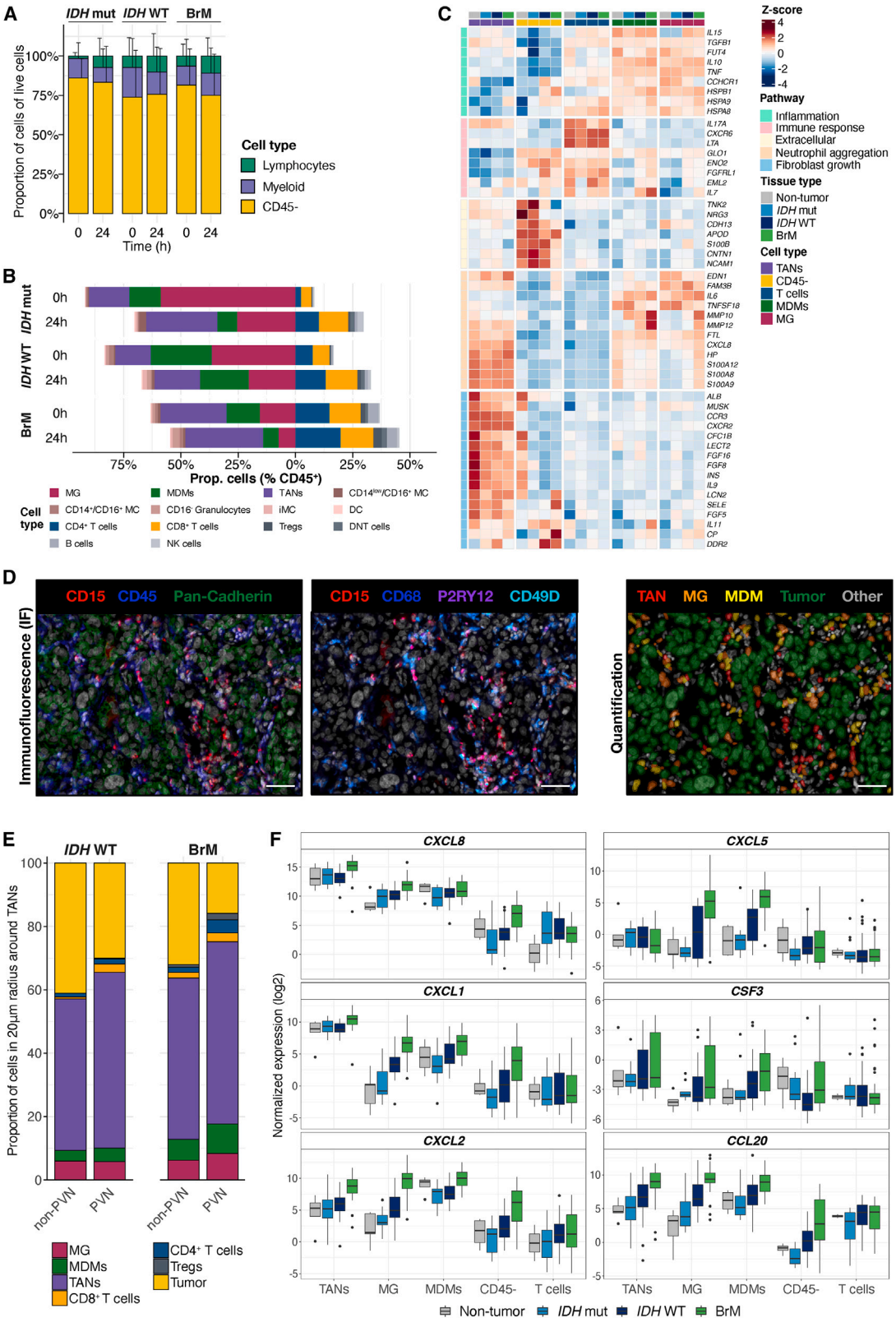

(legend on next page)

Three myeloid-specific clusters emerged: (1) pro-inflammatory factors produced mainly by TAMs (e.g., *TNF*, *IL6*, and *IL10*), (2) factors associated with recruitment and myeloid activation produced predominantly by neutrophils (e.g., *CXCR2*, *IL9*, *IL11*, and *CP*), and (3) activating/recruitment factors produced by the entire myeloid compartment (e.g., *MMP10*, *MMP12*, *CXCL8*, *S100A8*, *S100A9*, and *S100A12*) (Figures 6D and 7C). The TAM-specific inflammatory cluster was of interest as it contains many factors also found at the core of the secreted protein network (Figures 6D and 7C), suggesting a key role in shaping the MEC-CM. By contrast, and consistent with our TCM experiments, the $CD45^-$ population does not appear to be a major source of these cytokines specifically; however, it is a producer of extracellular-matrix-associated factors as well as CP in BrMs specifically (Figure 7C). Together, this led us to consider that the myeloid compartment is a predominant source of soluble factors driving brain-TAN alterations.

To explore the interactions within the myeloid compartment, we assessed whether TANs have a close spatial relationship with TAMs. Both TANs (Figures 1D, 1F, and S1C) and TAMs[10] are predominantly localized in the PVN; however, their spatial orientation in relation to each other has not been studied to date across different brain tumors. In a cohort of *IDH* WT glioma and BrM tissue samples, we quantified the cell types present within a radius of 20 μm around TANs, using sequential IF. We observed that TANs predominantly interact with other TANs both inside and outside the PVN (Figures 7D and 7E). Interactions with tumor cells were mostly observed in the non-PVN area. By contrast, MG and MDMs represent the most abundant non-TAN immune cells proximal to TANs, particularly in the BrM PVN, where they account for ~20% of the cellular neighborhoods (Figure 7E). Querying our RNA-seq data for neutrophil recruitment factors (Figure 7F), we found that TANs and TAMs show the highest expression of these chemokines (*CXCL8*, *CXCL5*, *CXCL1*, *CSF3*, *CXCL2*, and *CCL20*), with a progressive increase in more malignant tumor types (*IDH* WT gliomas and BrMs). Together, this revealed a highly interactive network within the myeloid cell niche of brain tumors, which is especially pronounced in the PVN. This myeloid network is not only crucial for the PBN-to-TAN phenotypic and functional transition but also for the recruitment of neutrophils to the brain TME itself.

DISCUSSION

In this study, we have analyzed the phenotypes and functions of neutrophils across diverse human brain tumors, comprising >190 clinical samples. By interrogating neutrophils in the periphery (PBNs) and the tumor (TANs), we found that brain TANs are highly abundant in *IDH* WT gliomas and BrMs and have a marked inflammatory phenotype compared with PBNs. This phenotype shares similarities with TANs in primary lung cancer[66] and inflammatory disease.[67] Importantly, independent of tumor type, and even in the absence of a tumor, neutrophils that infiltrate into the brain adapt transcriptionally to this unique organ microenvironment. The type of brain tumor confers additional, more pronounced transcriptional alterations, with BrM TANs showing the most substantial differences, including enrichment in multiple pro-inflammatory signaling networks. While BrM TANs share some transcriptional similarities to TANs in primary extracranial tumors, additional pro-inflammatory pathways are induced in BrM TANs, indicating an important contribution of TAN imprinting by both the tumor type and the local brain TME. Although neutrophil tissue specificity had previously been demonstrated for other tissue types (mostly in murine models), we demonstrate for the first time that this is also the case in human brain tissue. This discovery that the disease-specific TME imprints a unique layer of alterations onto TANs, in addition to brain-tissue-driven changes, shows interesting parallels to analyses of other brain TME populations including MG, MDMs[10,11,68] and T cells.[69,70] Our findings thereby underscore the necessity to not only investigate neutrophils within the specific organ of interest but also by additional stratification into distinct tumor subtypes.

We have addressed how the brain TME drives the observed TAN alterations, phenotypes, and functions, through a series of *ex vivo* assays and spatial analyses of patient samples, in parallel with interrogation of neutrophil behavior in mouse models. One notably pronounced effect of the brain TME on neutrophils, both in direct contact and via soluble factors, is the increased lifespan of TANs compared with matched PBNs. Prolonged TAN survival has similarly been observed in the context of several extracranial cancers.[71,72] We found that secreted factors in the brain TME can recapitulate the TAN phenotype and prolonged lifespan, when supplied exogenously to PBNs, and block ROS production. In extracranial tumors, both pro- and anti-tumoral effects of ROS have been reported.[40,41,43,73] In the intracranial setting, increased ROS production by tumor cells led to enhanced cytotoxicity in a glioma model,[14] Similarly, administration of engineered chimeric antigen receptor-neutrophils, with increased ROS production, resulted in glioma cell killing.[74] Taken together with our findings herein, this supports the triggering of a tumor-protective response by the brain TME via suppression of these damaging molecules.

Spatial analyses of the brain TME revealed perivascular and myeloid cell niches, in which TANs interact with these specific

Figure 7. Neutrophils interact with the myeloid compartment

(A) Proportion cells of live cells in *ex vivo* MEC ($n_{IDH\ mut}$ = 5, $n_{IDH\ WT}$ = 7, n_{BrM} = 13) at 0, 24 h (mean and SD).

(B) Mean proportions of immune cell populations as percent of $CD45^+$ cells from cultures shown in (A).

(C) Heatmap of gene expression levels in major TME populations for MEC-CM specific upregulated proteins depicted in Figure 6D. T cells include both $CD4^+$ and $CD8^+$ T cells. Clustering by overarching protein pathways based on Ward's method.

(D) Representative IF image and cell type quantification by QuPath in lung-BrM showing tumor cells (pan-cadherin$^+$), TANs ($CD45^+$,$CD15^+$), MG ($CD45^+$,CD68/$P2RY12^+$,$CD49D^-$), MDMs ($CD45^+$,CD68/$P2RY12^+$,$CD49D^+$) and "Other" (all remaining cells). Scale bars: 50 μm.

(E) Mean proportion of cell types identified in 20 μm radius around $TANs_{(n = 62,709)}$ in $BrM_{(n = 20)}$ and *IDH* WT $glioma_{(n = 7)}$.

(F) Normalized log_2-transformed expression of neutrophil-recruiting cytokines in different brain TME populations.

See also Figure S7.

cell types. The myeloid niche drives neutrophil recruitment into the brain via IL-8 and granulocyte-colony stimulating factor (G-CSF,encoded by *CXCL8* and *CSF3*, respectively). A previous study in a BrM mouse model similarly identified tumor cell-derived G-CSF as a recruiter of immunosuppressive PD-L1^{+} neutrophils.[18] The contribution of myeloid cells was, however, not investigated in this earlier study. Importantly, even though the expression of recruitment factors is effectively higher in myeloid cells, their overall abundance is lower by comparison to tumor cells. Thus, glioma and BrM tumor cells may additionally contribute to TAN recruitment. We also found angiogenesis pathways enriched in TANs and closely associated with deformed tumor vessels, which likely contribute to the continuous efflux of cells from the peripheral circulation. Indeed, spatial analyses combined with interrogation of secreted cytokines indicated critical immune-suppressive mechanisms of TANs at play within the brain TME. Of note, as peripheral T cells have not been primed to recognize tumor cells, and brain tumor-infiltrating lymphocytes have an exhausted phenotype[70] elucidating the immunosuppressive contribution of human brain TANs in *ex vivo* assays is challenging. Nonetheless, in several extracranial cancers, TANs have been demonstrated to similarly confer a direct inhibitory effect on T cells through their PD-L1 expression.[71,75] We show herein that immunosuppressive capacity appears to be a critical property of TANs in both gliomas and BrMs.

Investigation of the transition of PBNs to brain-TANs revealed an intricate network of predominantly pro-inflammatory mediators, including TNF-α. Given that the brain TME is rich in secreted TNF-α, and with TANs (particularly in BrM) showing a clear elevation of TNF-α signaling pathways, our data indicate that this cytokine is a critical mediator of the complex multifactorial neutrophil alterations herein. In the context of inflammation and cancer, TNF-α has been associated with induction of either an anti-, [31] or pro-tumoral[76] inflammatory TAN phenotype. Thus, its role in instructing TANs is highly context dependent; however, this function appears to be shared between gliomas and BrMs. Moreover, the TAN alterations we identified can in part be attributable to CP, as well as TNF-α. These two soluble factors were specifically found in MEC-CM, and RNA-seq analysis identified myeloid cells as the major source of these and other pro-inflammatory mediators. Integrating their capacity to recruit neutrophils and induce the PBN-to-TAN conversion, positions myeloid cells at the center of the TME networks critical for brain cancer development.

In summary, this study reports the first multifaceted interrogation of TANs across a large series of diverse human brain tumors. This revealed prolonged survival and extensive pro-inflammatory alterations of neutrophils within the brain tumor milieu, which is associated with T cell-suppressive and pro-angiogenic phenotypes. Moreover, we also present the first *in vivo* analyses of neutrophil dynamics in cancer, taking advantage of neutrophil-reporter mice[20] and multiple immune-competent cancer models. Together, our findings highlight the potential benefit of targeting soluble mediators produced within the myeloid niche that dictate the pro-inflammatory TAN phenotypes in brain cancers. Future studies, including in preclinical models, will be of considerable interest to investigate the efficacy of such therapeutic approaches.

Limitations of the study

In this study, we investigated TANs in both human and murine brain tumors. As analyzing neutrophils *in vivo* within patient brain tumors is technically not possible, we developed strategies enabling us to mimic the brain TME *ex vivo*. Nevertheless, there are some technical limitations as there is no immune cell recruitment in these MEC cultures and cell death gradually increases over time. Moreover, we are aware that our isolation methods, while carefully optimized and controlled, could activate TANs. Thus, we assessed the phenotype, and functional alteration of TANs both in isolated neutrophils and whole-tumor MEC cultures. No evident differences were observed; however, we cannot exclude that there are alterations to other functions and/or phenotypes that were not investigated herein.

Using *ex vivo* MEC-CM experiments, we established that soluble factors produced by the complete brain TME induce PBN-to-TAN alterations. A protein array (1,000 proteins) helped narrow down the responsible factors to 51 MEC-CM specific mediators, from which 5 cytokines (TNF-α, CP, GLO-1, IL-6, and IL-9) were studied in depth. None of these, either alone or in combination, could induce the complete TAN phenotype, indicating that additional factors are likely required. A larger unbiased screen would thus be needed to assess the potential contribution of other MEC-CM-specific molecules, including lipids and metabolites. In addition, it is crucial to validate the inhibition of these TME-secreted factors *in vivo*, given the limitations of *ex vivo* assays stated above.

Finally, the human and murine brain tumors used in this study represented late-stage tumors. Thus, it is important to note that neutrophil function and phenotype may differ at earlier stages of brain tumor formation. *In vivo* models will be required to address the complex neutrophil-tumor crosstalk over the temporal course of brain cancer development and progression.

STAR★METHODS

Detailed methods are provided in the online version of this paper and include the following:

- KEY RESOURCES TABLE
- RESOURCE AVAILABILITY
  - Lead contact
  - Materials availability
  - Data and code availability
- EXPERIMENTAL MODEL AND STUDY PARTICIPANT DETAILS
  - Human subjects
  - Primary cell cultures
- METHOD DETAILS
  - Human brain (tumor) enzymatic digestion
  - Flow cytometry and FACS
  - Immunofluorescence staining of tissue sections
  - Image analysis and cell type identification
  - Mouse tumor models
  - Mouse tissue analysis
  - Mathematical modeling of mean neutrophil lifetime
  - Murine PBN and TAN isolation
  - Human PBN and TAN isolation

- Reactive oxygen species (ROS) detection
- T cell cytokine array
- Annexin V apoptosis analysis
- UMAP and trajectory analysis
- Microenvironmental culture (MEC)-conditioned media (CM) collection and analysis
- Conditioned media (CM) generation from cell lines and primary cells
- CM education experiments
- Whole exome sequencing (WES)
- Protein array
- Recombinant protein treatment
- Software and visualization

- QUANTIFICATION AND STATISTICAL ANALYSIS

SUPPLEMENTAL INFORMATION

Supplemental information can be found online at https://doi.org/10.1016/j.cell.2023.08.043.

ACKNOWLEDGMENTS

We thank the Departments of Neurosurgery, Neuro-oncology, and Pathology at CHUV Lausanne; Dr. Florian Klemm; members of Prof. Hegi's lab; and Prof. Ron Stoop for generous collaboration in obtaining and processing patient samples. We thank Dr. Benoit Duc for helping collect HD blood and Dr. Spencer Watson and Paola Guerrero for insightful advice on QuPath image quantification. We gratefully acknowledge all current and former members of Prof. Joyce's lab, and members of the laboratories of Profs. Tacchini-Cottier, Meylan, De Palma, Petrova and Pittet, for insightful discussions and advice. We thank V. Noguet Brechbühl (Mouse Pathology Facility) for expert preparation of tissue sections; all members of the Epalinges and Agora animal facilities; P. Baumgartner and A.-C. Thierry for advice and technical support on multiplex cytokine arrays; and all members of the UNIL Flow Cytometry Facility for expert guidance in designing panels and performing FAC-sorting. We used Biorender to prepare the graphical abstract and several figure infographics. This research was supported by the Breast Cancer Research Foundation, Carigest Foundation, Fondation ISREC, Ludwig Institute for Cancer Research, Swiss Bridge Award, Swiss National Science Foundation Advanced Grant TMAG-3_209224, and University of Lausanne (to J.A.J.). K.S. was funded by an Erwin-Schrödinger Fellowship from the Austrian Science Fund (FWF, J4343-B28); M.M. received funding from AIRC and European Union's Horizon 2020 research and innovation programme under the Marie Skłodowska Curie (grant agreement 800924); S.G. was supported by Fondation Leenaards and Fondation ISREC; A.F.A.-P. was supported by an EMBO Long-Term Postdoctoral Fellowship (EMBO ALTF 654-2019) and a Marie Skłodowska Curie Actions Individual Fellowship (MSCA-IF 890933); G.F.C. is supported by MCIN/AEI/10.13039/501100011033 (grant PID2019-110895RB-I00) and by Junta de Comunidades de Castilla-La Mancha (SBPLY/19/180501/000211); R.S.M. is supported by the European Union's Horizon 2020 research and innovation program under the Skłodowska Curie grant agreement (grant agreement 955951, Evomet ITN); L.B. was supported by the European Molecular Biology Organisation (ALTF 1193-2018) and the Human Frontier Science Program (LT000038/2019); A.H. is funded by FET-OPEN (no. 861878) from the European Commission. The CNIC is supported by the MCIN and the Pro CNIC Foundation and is a Severo Ochoa Center of Excellence (CEX2020-001041-S). Our particular gratitude is extended to all patients and healthy volunteers who generously donated tissue for analyses, and without whom this study would not have been possible.

AUTHOR CONTRIBUTIONS

Conceptualization, R.R.M., K.S., and J.A.J.; methodology, R.R.M., K.S., M.M., S.G., M.K., and G.F.C.; formal analysis, R.R.M., N.F., J. Lourenco., A.F.A.-P., R.M., P.W., and G.F.C.; investigation, R.R.M., K.S., M.M., S.G., M.K., V.W., D.C., A.F.A.-P., D.N.M., J. Lilja, R.S.M., P.A., and L.B.; resources, A.H., I.B., A.F.H., J.-P.B., R.T.D., and M.E.H.; writing – original draft, R.R.M., K.S., S.G., and J.A.J.; writing – review & editing, all authors reviewed, edited, or commented on the manuscript; visualization, R.R.M., N.F., S.G., K.S., and G.F.C.; supervision, J.A.J.; funding acquisition, J.A.J., R.R.M., and K.S.

DECLARATION OF INTERESTS

D.C. has received consulting fees from Seed Biosciences S.A.; P.W. has provided consulting for Almax, Bayer, Sanofi, and Genentech. A.H. is a paid consultor for Flagship Pioneering, Inc. for matters unrelated to this study; M.E.H. has an advisory role at TME Pharma; J.A.J. received an honorarium for speaking at a Bristol Meyers Squibb research symposium and previously served on the scientific advisory board of Pionyr Immunotherapeutics.

Received: October 26, 2022
Revised: July 11, 2023
Accepted: August 31, 2023
Published: September 27, 2023

REFERENCES

1. Louis, D.N., Perry, A., Wesseling, P., Brat, D.J., Cree, I.A., Figarella-Branger, D., Hawkins, C., Ng, H.K., Pfister, S.M., Reifenberger, G., et al. (2021). The 2021 WHO classification of tumors of the central nervous system: a summary. Neuro. Oncol *23*, 1231–1251. https://doi.org/10.1093/neuonc/noab106.
2. Achrol, A.S., Rennert, R.C., Anders, C., Soffietti, R., Ahluwalia, M.S., Nayak, L., Peters, S., Arvold, N.D., Harsh, G.R., Steeg, P.S., et al. (2019). Brain metastases. Nat. Rev. Dis. Primers *5*, 5. https://doi.org/10.1038/s41572-018-0055-y.
3. Sperduto, P.W., Mesko, S., Li, J., Cagney, D., Aizer, A., Lin, N.U., Nesbit, E., Kruser, T.J., Chan, J., Braunstein, S., et al. (2020). Survival in patients with brain metastases: summary report on the updated diagnosis-specific graded prognostic assessment and definition of the eligibility quotient. J. Clin. Oncol. *38*, 3773–3784. https://doi.org/10.1200/JCO.20.01255.
4. Mohile, N.A., Messersmith, H., Gatson, N.T., Hottinger, A.F., Lassman, A., Morton, J., Ney, D., Nghiemphu, P.L., Olar, A., Olson, J., et al. (2022). Therapy for diffuse astrocytic and oligodendroglial tumors in adults: ASCO-SNO guideline. J. Clin. Oncol. *40*, 403–426. https://doi.org/10.1200/JCO.21.02036.
5. Cloughesy, T.F., Mochizuki, A.Y., Orpilla, J.R., Hugo, W., Lee, A.H., Davidson, T.B., Wang, A.C., Ellingson, B.M., Rytlewski, J.A., Sanders, C.M., et al. (2019). Neoadjuvant anti-PD-1 immunotherapy promotes a survival benefit with intratumoral and systemic immune responses in recurrent glioblastoma. Nat. Med. *25*, 477–486. https://doi.org/10.1038/s41591-018-0337-7.
6. Goldberg, S.B., Schalper, K.A., Gettinger, S.N., Mahajan, A., Herbst, R.S., Chiang, A.C., Lilenbaum, R., Wilson, F.H., Omay, S.B., Yu, J.B., et al. (2020). Pembrolizumab for management of patients with NSCLC and brain metastases: long-term results and biomarker analysis from a non-randomised, open-label, phase 2 trial. Lancet Oncol. *21*, 655–663. https://doi.org/10.1016/S1470-2045(20)30111-X.
7. Desbaillets, N., and Hottinger, A.F. (2021). Immunotherapy in glioblastoma: a clinical perspective. Cancers (Basel) *13*. https://doi.org/10.3390/cancers13153721.
8. Sampson, J.H., Gunn, M.D., Fecci, P.E., and Ashley, D.M. (2020). Brain immunology and immunotherapy in brain tumours. Nat. Rev. Cancer *20*, 12–25. https://doi.org/10.1038/s41568-019-0224-7.
9. Quail, D.F., and Joyce, J.A. (2017). The microenvironmental landscape of brain tumors. Cancer Cell *31*, 326–341. https://doi.org/10.1016/j.ccell.2017.02.009.
10. Klemm, F., Maas, R.R., Bowman, R.L., Kornete, M., Soukup, K., Nassiri, S., Brouland, J.P., Iacobuzio-Donahue, C.A., Brennan, C., Tabar, V., et al.

(2020). Interrogation of the microenvironmental landscape in brain tumors reveals disease-specific alterations of immune cells. Cell *181*, 1643–1660.e17. https://doi.org/10.1016/j.cell.2020.05.007.

11. Friebel, E., Kapolou, K., Unger, S., Núñez, N.G., Utz, S., Rushing, E.J., Regli, L., Weller, M., Greter, M., Tugues, S., et al. (2020). Single-cell mapping of human brain cancer reveals tumor-specific instruction of tissue-invading leukocytes. Cell *181*, 1626–1642.e20. https://doi.org/10.1016/j.cell.2020.04.055.
12. Andersen, B.M., Faust Akl, C., Wheeler, M.A., Chiocca, E.A., Reardon, D.A., and Quintana, F.J. (2021). Glial and myeloid heterogeneity in the brain tumour microenvironment. Nat. Rev. Cancer *21*, 786–802. https://doi.org/10.1038/s41568-021-00397-3.
13. Magod, P., Mastandrea, I., Rousso-Noori, L., Agemy, L., Shapira, G., Shomron, N., and Friedmann-Morvinski, D. (2021). Exploring the longitudinal glioma microenvironment landscape uncovers reprogrammed protumorigenic neutrophils in the bone marrow. Cell Rep. *36*, 109480. https://doi.org/10.1016/j.celrep.2021.109480.
14. Yee, P.P., Wei, Y., Kim, S.Y., Lu, T., Chih, S.Y., Lawson, C., Tang, M., Liu, Z., Anderson, B., Thamburaj, K., et al. (2020). Neutrophil-induced ferroptosis promotes tumor necrosis in glioblastoma progression. Nat. Commun. *11*, 5424. https://doi.org/10.1038/s41467-020-19193-y.
15. Liang, J., Piao, Y., Holmes, L., Fuller, G.N., Henry, V., Tiao, N., and de Groot, J.F. (2014). Neutrophils promote the malignant glioma phenotype through S100A4. Clin. Cancer Res. *20*, 187–198. https://doi.org/10.1158/1078-0432.CCR-13-1279.
16. Jiguet-Jiglaire, C., Boissonneau, S., Denicolai, E., Hein, V., Lasseur, R., Garcia, J., Romain, S., Appay, R., Graillon, T., Mason, W., et al. (2022). Plasmatic MMP9 released from tumor-infiltrating neutrophils is predictive for bevacizumab efficacy in glioblastoma patients: an AVAglio ancillary study. Acta Neuropathol. Commun. *10*, 1. https://doi.org/10.1186/s40478-021-01305-4.
17. Liu, Y., Kosaka, A., Ikeura, M., Kohanbash, G., Fellows-Mayle, W., Snyder, L.A., and Okada, H. (2013). Premetastatic soil and prevention of breast cancer brain metastasis. Neuro. Oncol *15*, 891–903. https://doi.org/10.1093/neuonc/not031.
18. Zhang, L., Yao, J., Wei, Y., Zhou, Z., Li, P., Qu, J., Badu-Nkansah, A., Yuan, X., Huang, Y.W., Fukumura, K., et al. (2020). Blocking immunosuppressive neutrophils deters pY696-EZH2-driven brain metastases. Sci. Transl. Med. *12*. https://doi.org/10.1126/scitranslmed.aaz5387.
19. Eruslanov, E.B., Singhal, S., and Albelda, S.M. (2017). Mouse versus human neutrophils in cancer: a major knowledge gap. Trends Cancer *3*, 149–160. https://doi.org/10.1016/j.trecan.2016.12.006.
20. Ballesteros, I., Rubio-Ponce, A., Genua, M., Lusito, E., Kwok, I., Fernández-Calvo, G., Khoyratty, T.E., van Grinsven, E., González-Hernández, S., Nicolás-Ávila, J.Á., et al. (2020). Co-option of neutrophil fates by tissue environments. Cell *183*, 1282–1297.e18. https://doi.org/10.1016/j.cell.2020.10.003.
21. Hedrick, C.C., and Malanchi, I. (2022). Neutrophils in cancer: heterogeneous and multifaceted. Nat. Rev. Immunol. *22*, 173–187. https://doi.org/10.1038/s41577-021-00571-6.
22. Quail, D.F., Amulic, B., Aziz, M., Barnes, B.J., Eruslanov, E., Fridlender, Z.G., Goodridge, H.S., Granot, Z., Hidalgo, A., Huttenlocher, A., et al. (2022). Neutrophil phenotypes and functions in cancer: a consensus statement. J. Exp. Med. *219*. https://doi.org/10.1084/jem.20220011.
23. Maas, R.R., Soukup, K., Klemm, F., Kornete, M., Bowman, R.L., Bedel, R., Marie, D.N., Álvarez-Prado, Á.F., Labes, D., Wilson, A., et al. (2021). An integrated pipeline for comprehensive analysis of immune cells in human brain tumor clinical samples. Nat. Protoc. *16*, 4692–4721. https://doi.org/10.1038/s41596-021-00594-2.
24. Cupp, M.A., Cariolou, M., Tzoulaki, I., Aune, D., Evangelou, E., and Berlanga-Taylor, A.J. (2020). Neutrophil to lymphocyte ratio and cancer prognosis: an umbrella review of systematic reviews and meta-analyses of observational studies. BMC Med. *18*, 360. https://doi.org/10.1186/s12916-020-01817-1.
25. Starzer, A.M., Steindl, A., Mair, M.J., Deischinger, C., Simonovska, A., Widhalm, G., Gatterbauer, B., Dieckmann, K., Heller, G., Preusser, M., et al. (2021). Systemic inflammation scores correlate with survival prognosis in patients with newly diagnosed brain metastases. Br. J. Cancer *124*, 1294–1300. https://doi.org/10.1038/s41416-020-01254-0.
26. Shaul, M.E., and Fridlender, Z.G. (2019). Tumour-associated neutrophils in patients with cancer. Nat. Rev. Clin. Oncol. *16*, 601–620. https://doi.org/10.1038/s41571-019-0222-4.
27. Zhang, L., Hu, Y., Chen, W., Tian, Y., Xie, Y., and Chen, J. (2020). Pre-stereotactic radiosurgery neutrophil-to-lymphocyte ratio is a predictor of the prognosis for brain metastases. J. Neurooncol. *147*, 691–700. https://doi.org/10.1007/s11060-020-03477-w.
28. Coffelt, S.B., Kersten, K., Doornebal, C.W., Weiden, J., Vrijland, K., Hau, C.S., Verstegen, N.J.M., Ciampricotti, M., Hawinkels, L.J.A.C., Jonkers, J., et al. (2015). IL-17-producing γδ T cells and neutrophils conspire to promote breast cancer metastasis. Nature *522*, 345–348. https://doi.org/10.1038/nature14282.
29. Wellenstein, M.D., Coffelt, S.B., Duits, D.E.M., van Miltenburg, M.H., Slagter, M., de Rink, I., Henneman, L., Kas, S.M., Prekovic, S., Hau, C.S., et al. (2019). Loss of p53 triggers WNT-dependent systemic inflammation to drive breast cancer metastasis. Nature *572*, 538–542. https://doi.org/10.1038/s41586-019-1450-6.
30. Peng, Z., Liu, C., Victor, A.R., Cao, D.Y., Veiras, L.C., Bernstein, E.A., Khan, Z., Giani, J.F., Cui, X., Bernstein, K.E., et al. (2021). Tumors exploit CXCR4(hi)CD62L(lo) aged neutrophils to facilitate metastatic spread. Oncoimmunology *10*, 1870811. https://doi.org/10.1080/2162402X.2020.1870811.
31. Finisguerra, V., Di Conza, G., Di Matteo, M., Serneels, J., Costa, S., Thompson, A.A., Wauters, E., Walmsley, S., Prenen, H., Granot, Z., et al. (2015). MET is required for the recruitment of anti-tumoural neutrophils. Nature *522*, 349–353. https://doi.org/10.1038/nature14407.
32. Glodde, N., Bald, T., van den Boorn-Konijnenberg, D., Nakamura, K., O'Donnell, J.S., Szczepanski, S., Brandes, M., Eickhoff, S., Das, I., Shridhar, N., et al. (2017). Reactive neutrophil responses dependent on the receptor tyrosine kinase c-MET limit cancer immunotherapy. Immunity *47*, 789–802.e9. https://doi.org/10.1016/j.immuni.2017.09.012.
33. Bodac, A., and Meylan, E. (2021). Neutrophil metabolism in the cancer context. Semin. Immunol. *57*, 101583. https://doi.org/10.1016/j.smim.2021.101583.
34. García-Navas, R., Gajate, C., and Mollinedo, F. (2021). Neutrophils drive endoplasmic reticulum stress-mediated apoptosis in cancer cells through arginase-1 release. Sci. Rep. *11*, 12574. https://doi.org/10.1038/s41598-021-91947-0.
35. Wang, J.F., Wang, Y.P., Xie, J., Zhao, Z.Z., Gupta, S., Guo, Y., Jia, S.H., Parodo, J., Marshall, J.C., and Deng, X.M. (2021). Upregulated PD-L1 delays human neutrophil apoptosis and promotes lung injury in an experimental mouse model of sepsis. Blood *138*, 806–810. https://doi.org/10.1182/blood.2020009417.
36. Zilionis, R., Engblom, C., Pfirschke, C., Savova, V., Zemmour, D., Saatcioglu, H.D., Krishnan, I., Maroni, G., Meyerovitz, C.V., Kerwin, C.M., et al. (2019). Single-cell transcriptomics of human and mouse lung cancers reveals conserved myeloid populations across individuals and species. Immunity *50*, 1317–1334.e10. https://doi.org/10.1016/j.immuni.2019.03.009.
37. Salcher, S., Sturm, G., Horvath, L., Untergasser, G., Kuempers, C., Fotakis, G., Panizzolo, E., Martowicz, A., Trebo, M., Pall, G., et al. (2022). High-resolution single-cell atlas reveals diversity and plasticity of tissue-resident neutrophils in non-small cell lung cancer. Cancer Cell *40*, 1503–1520.e8. https://doi.org/10.1016/j.ccell.2022.10.008.
38. Alvarez-Breckenridge, C., Markson, S.C., Stocking, J.H., Nayyar, N., Lastrapes, M., Strickland, M.R., Kim, A.E., de Sauvage, M., Dahal, A., Larson, J.M., et al. (2022). Microenvironmental landscape of human melanoma brain metastases in response to immune checkpoint inhibition.

Cancer Immunol. Res. *10*, 996–1012. https://doi.org/10.1158/2326-6066.CIR-21-0870.

39. Álvarez-Prado, Á.F., Maas, R.R., Soukup, K., Klemm, F., Kornete, M., Krebs, F.S., Zoete, V., Berezowska, S., Brouland, J.P., Hottinger, A.F., et al. (2023). Immunogenomic analysis of human brain metastases reveals diverse immune landscapes across genetically distinct tumors. Cell Rep. Med. *4*, 100900. https://doi.org/10.1016/j.xcrm.2022.100900.

40. Gershkovitz, M., Caspi, Y., Fainsod-Levi, T., Katz, B., Michaeli, J., Khawaled, S., Lev, S., Polyansky, L., Shaul, M.E., Sionov, R.V., et al. (2018). TRPM2 mediates neutrophil killing of disseminated tumor cells. Cancer Res. *78*, 2680–2690. https://doi.org/10.1158/0008-5472.CAN-17-3614.

41. Granot, Z., Henke, E., Comen, E.A., King, T.A., Norton, L., and Benezra, R. (2011). Tumor entrained neutrophils inhibit seeding in the premetastatic lung. Cancer Cell *20*, 300–314. https://doi.org/10.1016/j.ccr.2011.08.012.

42. Takeshima, T., Pop, L.M., Laine, A., Iyengar, P., Vitetta, E.S., and Hannan, R. (2016). Key role for neutrophils in radiation-induced antitumor immune responses: potentiation with G-CSF. Proc. Natl. Acad. Sci. USA *113*, 11300–11305. https://doi.org/10.1073/pnas.1613187113.

43. Rice, C.M., Davies, L.C., Subleski, J.J., Maio, N., Gonzalez-Cotto, M., Andrews, C., Patel, N.L., Palmieri, E.M., Weiss, J.M., Lee, J.M., et al. (2018). Tumour-elicited neutrophils engage mitochondrial metabolism to circumvent nutrient limitations and maintain immune suppression. Nat. Commun. *9*, 5099. https://doi.org/10.1038/s41467-018-07505-2.

44. Schmielau, J., and Finn, O.J. (2001). Activated granulocytes and granulocyte-derived hydrogen peroxide are the underlying mechanism of suppression of T-cell function in advanced cancer patients. Cancer Res. *61*, 4756–4760.

45. Singhal, S., Bhojnagarwala, P.S., O'Brien, S., Moon, E.K., Garfall, A.L., Rao, A.S., Quatromoni, J.G., Stephen, T.L., Litzky, L., Deshpande, C., et al. (2016). Origin and role of a subset of tumor-associated neutrophils with antigen-presenting cell features in early-stage human lung cancer. Cancer Cell *30*, 120–135. https://doi.org/10.1016/j.ccell.2016.06.001.

46. De Palma, M., Biziato, D., and Petrova, T.V. (2017). Microenvironmental regulation of tumour angiogenesis. Nat. Rev. Cancer *17*, 457–474. https://doi.org/10.1038/nrc.2017.51.

47. Hao, Q., Chen, Y., Zhu, Y., Fan, Y., Palmer, D., Su, H., Young, W.L., and Yang, G.Y. (2007). Neutrophil depletion decreases VEGF-induced focal angiogenesis in the mature mouse brain. J. Cereb. Blood Flow Metab. *27*, 1853–1860. https://doi.org/10.1038/sj.jcbfm.9600485.

48. Ajikumar, A., Long, M.B., Heath, P.R., Wharton, S.B., Ince, P.G., Ridger, V.C., and Simpson, J.E. (2019). Neutrophil-derived microvesicle induced dysfunction of brain microvascular endothelial cells in vitro. Int. J. Mol. Sci. *20*. https://doi.org/10.3390/ijms20205227.

49. Qiu, Y.M., Zhang, C.L., Chen, A.Q., Wang, H.L., Zhou, Y.F., Li, Y.N., and Hu, B. (2021). Immune cells in the BBB disruption after acute ischemic stroke: targets for immune therapy? Front. Immunol. *12*, 678744. https://doi.org/10.3389/fimmu.2021.678744.

50. Winkler, F., Kozin, S.V., Tong, R.T., Chae, S.S., Booth, M.F., Garkavtsev, I., Xu, L., Hicklin, D.J., Fukumura, D., di Tomaso, E., et al. (2004). Kinetics of vascular normalization by VEGFR2 blockade governs brain tumor response to radiation: role of oxygenation, angiopoietin-1, and matrix metalloproteinases. Cancer Cell *6*, 553–563. https://doi.org/10.1016/j.ccr.2004.10.011.

51. Izumi, Y., Xu, L., di Tomaso, E., Fukumura, D., and Jain, R.K. (2002). Tumour biology: herceptin acts as an anti-angiogenic cocktail. Nature *416*, 279–280. https://doi.org/10.1038/416279b.

52. Arvanitis, C.D., Ferraro, G.B., and Jain, R.K. (2020). The blood-brain barrier and blood-tumour barrier in brain tumours and metastases. Nat. Rev. Cancer *20*, 26–41. https://doi.org/10.1038/s41568-019-0205-x.

53. Wang, S., Song, R., Wang, Z., Jing, Z., Wang, S., and Ma, J. (2018). S100A8/A9 in inflammation. Front. Immunol. *9*, 1298. https://doi.org/10.3389/fimmu.2018.01298.

54. Quintero-Fabián, S., Arreola, R., Becerril-Villanueva, E., Torres-Romero, J.C., Arana-Argáez, V., Lara-Riegos, J., Ramírez-Camacho, M.A., and Alvarez-Sánchez, M.E. (2019). Role of matrix metalloproteinases in angiogenesis and cancer. Front. Oncol. *9*, 1370. https://doi.org/10.3389/fonc.2019.01370.

55. Summers, C., Rankin, S.M., Condliffe, A.M., Singh, N., Peters, A.M., and Chilvers, E.R. (2010). Neutrophil kinetics in health and disease. Trends Immunol. *31*, 318–324. https://doi.org/10.1016/j.it.2010.05.006.

56. Adrover, J.M., Nicolás-Ávila, J.A., and Hidalgo, A. (2016). Aging: a temporal dimension for neutrophils. Trends Immunol. *37*, 334–345. https://doi.org/10.1016/j.it.2016.03.005.

57. Brostjan, C., and Oehler, R. (2020). The role of neutrophil death in chronic inflammation and cancer. Cell Death Discov. *6*, 26. https://doi.org/10.1038/s41420-020-0255-6.

58. Comen, E., Wojnarowicz, P., Seshan, V.E., Shah, R., Coker, C., Norton, L., and Benezra, R. (2016). TNF is a key cytokine mediating neutrophil cytotoxic activity in breast cancer patients. npj Breast Cancer *2*, 16009. https://doi.org/10.1038/npjbcancer.2016.9.

59. Vieira, S.M., Lemos, H.P., Grespan, R., Napimoga, M.H., Dal-Secco, D., Freitas, A., Cunha, T.M., Verri, W.A., Jr., Souza-Junior, D.A., Jamur, M.C., et al. (2009). A crucial role for TNF-alpha in mediating neutrophil influx induced by endogenously generated or exogenous chemokines, KC/CXCL1 and LIX/CXCL5. Br. J. Pharmacol. *158*, 779–789. https://doi.org/10.1111/j.1476-5381.2009.00367.x.

60. Chapman, A.L., Mocatta, T.J., Shiva, S., Seidel, A., Chen, B., Khalilova, I., Paumann-Page, M.E., Jameson, G.N., Winterbourn, C.C., and Kettle, A.J. (2013). Ceruloplasmin is an endogenous inhibitor of myeloperoxidase. J. Biol. Chem. *288*, 6465–6477. https://doi.org/10.1074/jbc.M112.418970.

61. Golenkina, E.A., Viryasova, G.M., Galkina, S.I., Gaponova, T.V., Sud'ina, G.F., and Sokolov, A.V. (2018). Fine regulation of neutrophil oxidative status and apoptosis by ceruloplasmin and its derivatives. Cells *7*. https://doi.org/10.3390/cells7010008.

62. Xue, M., Rabbani, N., Momiji, H., Imbasi, P., Anwar, M.M., Kitteringham, N., Park, B.K., Souma, T., Moriguchi, T., Yamamoto, M., et al. (2012). Transcriptional control of glyoxalase 1 by Nrf2 provides a stress-responsive defence against dicarbonyl glycation. Biochem. J. *443*, 213–222. https://doi.org/10.1042/BJ20111648.

63. Chowdhury, K., Kumar, U., Das, S., Chaudhuri, J., Kumar, P., Kanjilal, M., Ghosh, P., Sircar, G., Basyal, R.K., Kanga, U., et al. (2018). Synovial IL-9 facilitates neutrophil survival, function and differentiation of Th17 cells in rheumatoid arthritis. Arthritis Res. Ther. *20*, 18. https://doi.org/10.1186/s13075-017-1505-8.

64. Xiao, Y., Cong, M., Li, J., He, D., Wu, Q., Tian, P., Wang, Y., Yang, S., Liang, C., Liang, Y., et al. (2021). Cathepsin C promotes breast cancer lung metastasis by modulating neutrophil infiltration and neutrophil extracellular trap formation. Cancer Cell *39*, 423–437.e7. https://doi.org/10.1016/j.ccell.2020.12.012.

65. Zha, C., Meng, X., Li, L., Mi, S., Qian, D., Li, Z., Wu, P., Hu, S., Zhao, S., Cai, J., et al. (2020). Neutrophil extracellular traps mediate the crosstalk between glioma progression and the tumor microenvironment via the HMGB1/RAGE/IL-8 axis. Cancer Biol. Med. *17*, 154–168. https://doi.org/10.20892/j.issn.2095-3941.2019.0353.

66. Eruslanov, E.B., Bhojnagarwala, P.S., Quatromoni, J.G., Stephen, T.L., Ranganathan, A., Deshpande, C., Akimova, T., Vachani, A., Litzky, L., Hancock, W.W., et al. (2014). Tumor-associated neutrophils stimulate T cell responses in early-stage human lung cancer. J. Clin. Invest. *124*, 5466–5480. https://doi.org/10.1172/JCI77053.

67. Fortunati, E., Kazemier, K.M., Grutters, J.C., Koenderman, L., and Van den Bosch v, J. (2009). Human neutrophils switch to an activated phenotype after homing to the lung irrespective of inflammatory disease. Clin.

Exp. Immunol. *155*, 559–566. https://doi.org/10.1111/j.1365-2249.2008.03791.x.

68. Gonzalez, H., Mei, W., Robles, I., Hagerling, C., Allen, B.M., Hauge Okholm, T.L., Nanjaraj, A., Verbeek, T., Kalavacherla, S., van Gogh, M., et al. (2022). Cellular architecture of human brain metastases. Cell *185*, 729–745.e20. https://doi.org/10.1016/j.cell.2021.12.043.
69. Sudmeier, L.J., Hoang, K.B., Nduom, E.K., Wieland, A., Neill, S.G., Schniederjan, M.J., Ramalingam, S.S., Olson, J.J., Ahmed, R., and Hudson, W.H. (2022). Distinct phenotypic states and spatial distribution of CD8(+) T cell clonotypes in human brain metastases. Cell. Rep. Med. *3*, 100620. https://doi.org/10.1016/j.xcrm.2022.100620.
70. Wischnewski, V., Maas, R.R., Aruffo, P.G., Soukup, K., Galletti, G., Kornete, M., Galland, S., Fournier, N., Lilja, J., Wirapati, P., et al. (2023). Phenotypic diversity of T cells in human primary and metastatic brain tumors revealed by multiomic interrogation. Nat. Cancer *4*, 908–924. https://doi.org/10.1038/s43018-023-00566-3.
71. Wang, T.T., Zhao, Y.L., Peng, L.S., Chen, N., Chen, W., Lv, Y.P., Mao, F.Y., Zhang, J.Y., Cheng, P., Teng, Y.S., et al. (2017). Tumour-activated neutrophils in gastric cancer foster immune suppression and disease progression through GM-CSF-PD-L1 pathway. Gut *66*, 1900–1911. https://doi.org/10.1136/gutjnl-2016-313075.
72. Wu, L., Saxena, S., Goel, P., Prajapati, D.R., Wang, C., and Singh, R.K. (2020). Breast cancer cell-neutrophil interactions enhance neutrophil survival and pro-tumorigenic activities. Cancers (Basel) *12*. https://doi.org/10.3390/cancers12102884.
73. Mensurado, S., Rei, M., Lança, T., Ioannou, M., Gonçalves-Sousa, N., Kubo, H., Malissen, M., Papayannopoulos, V., Serre, K., and Silva-Santos, B. (2018). Tumor-associated neutrophils suppress pro-tumoral IL-17+ $\gamma\delta$ T cells through induction of oxidative stress. PLoS Biol. *16*, e2004990. https://doi.org/10.1371/journal.pbio.2004990.
74. Chang, Y., Cai, X., Syahirah, R., Yao, Y., Xu, Y., Jin, G., Bhute, V.J., Torregrosa-Allen, S., Elzey, B.D., Won, Y.Y., et al. (2023). CAR-neutrophil mediated delivery of tumor-microenvironment responsive nanodrugs for glioblastoma chemo-immunotherapy. Nat. Commun. *14*, 2266. https://doi.org/10.1038/s41467-023-37872-4.
75. Xue, R., Zhang, Q., Cao, Q., Kong, R., Xiang, X., Liu, H., Feng, M., Wang, F., Cheng, J., Li, Z., et al. (2022). Liver tumour immune microenvironment subtypes and neutrophil heterogeneity. Nature *612*, 141–147. https://doi.org/10.1038/s41586-022-05400-x.
76. Shan, Z.G., Chen, J., Liu, J.S., Zhang, J.Y., Wang, T.T., Teng, Y.S., Mao, F.Y., Cheng, P., Zou, Q.M., Zhou, W.Y., et al. (2021). Activated neutrophils polarize protumorigenic interleukin-17A-producing T helper subsets through TNF-alpha-B7-H2-dependent pathway in human gastric cancer. Clin. Transl. Med. *11*, e484. https://doi.org/10.1002/ctm2.484.
77. Szklarczyk, D., Morris, J.H., Cook, H., Kuhn, M., Wyder, S., Simonovic, M., Santos, A., Doncheva, N.T., Roth, A., Bork, P., et al. (2017). The STRING database in 2017: quality-controlled protein-protein association networks, made broadly accessible. Nucleic Acids Res. *45*, D362–D368. https://doi.org/10.1093/nar/gkw937.
78. Croci, D., Santalla Méndez, R., Temme, S., Soukup, K., Fournier, N., Zomer, A., Colotti, R., Wischnewski, V., Flögel, U., van Heeswijk, R.B., et al. (2022). Multispectral fluorine-19 MRI enables longitudinal and noninvasive monitoring of tumor-associated macrophages. Sci. Transl. Med. *14*, eabo2952. https://doi.org/10.1126/scitranslmed.abo2952.
79. Holland, E.C., Hively, W.P., DePinho, R.A., and Varmus, H.E. (1998). A constitutively active epidermal growth factor receptor cooperates with disruption of G1 cell-cycle arrest pathways to induce glioma-like lesions in mice. Genes Dev. *12*, 3675–3685. https://doi.org/10.1101/gad.12.23.3675.
80. Bankhead, P., Loughrey, M.B., Fernández, J.A., Dombrowski, Y., McArt, D.G., Dunne, P.D., McQuaid, S., Gray, R.T., Murray, L.J., Coleman, H.G., et al. (2017). QuPath: open source software for digital pathology image analysis. Sci. Rep. *7*, 16878. https://doi.org/10.1038/s41598-017-17204-5.
81. Schmidt, U., Weigert, M., Broaddus, C., and Myers, G. (2018). Cell detection with star-convex polygons. In Medical Image Computing and Computer Assisted Intervention – MICCAI 2018 : 21st International Conference (Springer International Publishing), pp. 265–273.
82. Dobin, A., Davis, C.A., Schlesinger, F., Drenkow, J., Zaleski, C., Jha, S., Batut, P., Chaisson, M., and Gingeras, T.R. (2013). STAR: ultrafast universal RNA-seq aligner. Bioinformatics *29*, 15–21. https://doi.org/10.1093/bioinformatics/bts635.
83. Li, B., and Dewey, C.N. (2011). RSEM: accurate transcript quantification from RNA-seq data with or without a reference genome. BMC Bioinformatics *12*, 323. https://doi.org/10.1186/1471-2105-12-323.
84. Baddeley, A., Rubak, E., and Turner, R. (2015). Spatial point patterns: methodology and applications with (R (CRC press).
85. Robinson, M.D., McCarthy, D.J., and Smyth, G.K. (2010). edgeR: a Bioconductor package for differential expression analysis of digital gene expression data. Bioinformatics *26*, 139–140. https://doi.org/10.1093/bioinformatics/btp616.
86. Ritchie, M.E., Phipson, B., Wu, D., Hu, Y.F., Law, C.W., Shi, W., and Smyth, G.K. (2015). limma powers differential expression analyses for RNA-sequencing and microarray studies. Nucleic Acids Res. *43*, e47. https://doi.org/10.1093/nar/gkv007.
87. Leek, J.T., and Storey, J.D. (2007). Capturing heterogeneity in gene expression studies by surrogate variable analysis. PLoS Genet. *3*, 1724–1735. https://doi.org/10.1371/journal.pgen.0030161.
88. Wu, T.Z., Hu, E.Q., Xu, S.B., Chen, M.J., Guo, P.F., Dai, Z.H., Feng, T.Z., Zhou, L., Tang, W.L., Zhan, L., et al. (2021). clusterProfiler 4.0: a universal enrichment tool for interpreting omics data. Innovation (Camb) *2*, 100141. https://doi.org/10.1016/j.xinn.2021.100141.
89. Blighe, K. (2021). scDataviz: single cell dataviz and downstream analysesR package version 1.2.0 (Bioconductor. https://doi.org/10.18129/B9.bioc.scDataviz.
90. Wickham, H. (2016). ggplot2: Elegant Graphics for Data Analysis (Springer-Verlag).
91. Trapnell, C., Cacchiarelli, D., Grimsby, J., Pokharel, P., Li, S., Morse, M., Lennon, N.J., Livak, K.J., Mikkelsen, T.S., and Rinn, J.L. (2014). The dynamics and regulators of cell fate decisions are revealed by pseudotemporal ordering of single cells. Nat. Biotechnol. *32*, 381–386. https://doi.org/10.1038/nbt.2859.
92. Street, K., Risso, D., Fletcher, R.B., Das, D., Ngai, J., Yosef, N., Purdom, E., and Dudoit, S. (2018). Slingshot: cell lineage and pseudotime inference for single-cell transcriptomics. BMC Genomics *19*, 477. https://doi.org/10.1186/s12864-018-4772-0.
93. Martin, M. (2011). Cutadapt removes adapter sequences from high-throughput sequencing reads. EMBnet.journal *17*, 10–12. https://doi.org/10.14806/ej.17.1.200.
94. Li, H., and Durbin, R. (2009). Fast and accurate short read alignment with Burrows-Wheeler transform. Bioinformatics *25*, 1754–1760. https://doi.org/10.1093/bioinformatics/btp324.
95. Danecek, P., Bonfield, J.K., Liddle, J., Marshall, J., Ohan, V., Pollard, M.O., Whitwham, A., Keane, T., McCarthy, S.A., Davies, R.M., et al. (2021). Twelve years of SAMtools and BCFtools. GigaScience *10*. https://doi.org/10.1093/gigascience/giab008.
96. McLaren, W., Gil, L., Hunt, S.E., Riat, H.S., Ritchie, G.R., Thormann, A., Flicek, P., and Cunningham, F. (2016). The Ensembl variant effect predictor. Genome Biol. *17*, 122. https://doi.org/10.1186/s13059-016-0974-4.
97. Gu, Z.G., Eils, R., and Schlesner, M. (2016). Complex heatmaps reveal patterns and correlations in multidimensional genomic data. Bioinformatics *32*, 2847–2849. https://doi.org/10.1093/bioinformatics/btw313.
98. Csardi, G., and Nepusz, T. (2006). The igraph software package for complex network research. InterJournal Complex Systems *1695*, 1–9.
99. Bates, D., Mächler, M., Bolker, B.M., and Walker, S.C. (2015). Fitting linear mixed-effects models using lme4. J. Stat. Softw. *67*, 1–48. https://doi.org/10.18637/jss.v067.i01.

100. Kuznetsova, A., Brockhoff, P.B., and Christensen, R.H.B. (2017). lmerTest package: tests in linear mixed effects models. J. Stat. Softw. *82*, 1–26. https://doi.org/10.18637/jss.v082.i13.

101. Ozawa, T., Riester, M., Cheng, Y.K., Huse, J.T., Squatrito, M., Helmy, K., Charles, N., Michor, F., and Holland, E.C. (2014). Most human non-GCIMP glioblastoma subtypes evolve from a common proneural-like precursor glioma. Cancer Cell *26*, 288–300. https://doi.org/10.1016/j.ccr.2014.06.005.

102. Becher, O.J., Hambardzumyan, D., Fomchenko, E.I., Momota, H., Mainwaring, L., Bleau, A.M., Katz, A.M., Edgar, M., Kenney, A.M., Cordon-Cardo, C., et al. (2008). Gli activity correlates with tumor grade in platelet-derived growth factor-induced gliomas. Cancer Res. *68*, 2241–2249. https://doi.org/10.1158/0008-5472.CAN-07-6350.

103. Gut, G., Herrmann, M.D., and Pelkmans, L. (2018). Multiplexed protein maps link subcellular organization to cellular states. Science *361*. https://doi.org/10.1126/science.aar7042.

104. Sternberg, S.R. (1983). Biomedical image processing. Computer *16*, 22–34.

105. Baddeley, A., and Turner, R. (2005). spatstat: an R package for analyzing spatial point patterns. J. Stat. Softw. *12*, 1–42. https://doi.org/10.18637/jss.v012.i06.

106. Pyonteck, S.M., Akkari, L., Schuhmacher, A.J., Bowman, R.L., Sevenich, L., Quail, D.F., Olson, O.C., Quick, M.L., Huse, J.T., Teijeiro, V., et al. (2013). CSF-1R inhibition alters macrophage polarization and blocks glioma progression. Nat. Med. *19*, 1264–1272. https://doi.org/10.1038/nm.3337.

107. Hambardzumyan, D., Amankulor, N.M., Helmy, K.Y., Becher, O.J., and Holland, E.C. (2009). Modeling adult gliomas using RCAS/t-va technology. Transl. Oncol. *2*, 89–95. https://doi.org/10.1593/tlo.09100.

STAR★METHODS

KEY RESOURCES TABLE

REAGENT or RESOURCE	SOURCE	IDENTIFIER
Antibodies		
FCM: Annexin V PE	Thermo Fisher Scientific	Cat# 88-8102-72, RRID:AB_2575183
FCM: Arginase 1 PE-Cyanine7, rat monoclonal anti-human (clone A1exF5), dilution 1:80	Thermo Fisher Scientific	Cat# 25-3697-80, RRID:AB_2734840
FCM: CD11b APC, rat monoclonal anti-human/mouse (clone M1/70), dilution 1:300	Thermo Fisher Scientific	Cat# 17-0112-82, RRID:AB_469343
FCM: CD11B BUV661, rat monoclonal anti-human/mouse (clone M1/70), dilution 1:1280	BD Bioscience	Cat# 612977, RRID:AB_2870249
FCM: CD11B BUV737, rat monoclonal anti-human/mouse (clone M1/70), dilution 1:1280	BD Bioscience	Cat# 612800, RRID:AB_2870127
FCM: CD11B BV421, rat monoclonal anti-human/mouse (clone M1/70), dilution 1:1280	BioLegend	Cat# 101251, RRID:AB_2562904
FCM: CD11C BV605, mouse monoclonal anti-human (clone 3.9), dilution 1:320	BioLegend	Cat # 301636, RRID:AB_2563796
FCM: CD127 BV510, mouse monoclonal anti-human (clone A019D5), dilution 1:160	BioLegend	Cat # 351332, RRID:AB_2562304
FCM: CD14 AF488, mouse monoclonal anti-human (clone HCD14), dilution 1:640	BioLegend	Cat # 325610, RRID:AB_830683
FCM: CD15 BV510, mouse monoclonal anti-human (clone W6D3), dilution 1:640	BioLegend	Cat # 323028, RRID:AB_2563400
FCM: CD16 BUV737 mouse monoclonal anti-human (clone 3G8), dilution 1:640	BD Bioscience	Cat # 612786, RRID:AB_2833077
FCM: CD16 BV421 mouse monoclonal anti-human (clone 3G8), dilution 1:1280	BioLegend	Cat # 302037, RRID:AB_10898112
FCM: CD16 BV510 mouse monoclonal anti-human (clone 3G8), dilution 1:1280	BioLegend	Cat # 302048, RRID:AB_2562085
FCM: CD16 BV785 mouse monoclonal anti-human (clone 3G8), dilution 1:640	BioLegend	Cat# 360734, RRID:AB_2800994
FCM: CD19 BUV563, mouse monoclonal anti-human (clone SJ25C1), dilution 1:320	BD Bioscience	Cat # 612916, RRID:AB_2870201
FCM: CD25 PE, mouse monoclonal anti-human (clone BC96), dilution 1:80	BioLegend	Cat # 302606, RRID:AB_314276
FCM: CD274 (PD-L1) BV711 mouse monoclonal anti-human (clone 29E.2A3), dilution 1:60	BioLegend	Cat# 329722, RRID:AB_2565764
FCM: CD3 PerCP/Cy5.5 mouse monoclonal anti-human (clone HIT3a), dilution 1:80	BioLegend	Cat# 300328, RRID:AB_1575008
FCM: CD4 BV650 mouse monoclonal anti-human (clone OKT4), dilution 1:200	BioLegend	Cat# 317436, RRID:AB_2563050
FCM: CD45 AF700 mouse monoclonal anti-human (clone HI30), dilution 1:640	BioLegend	Cat# 304023, RRID:AB_493760
FCM: CD45 AF700 rat monoclonal anti-mouse (clone 30-F11), dilution 1:500	BioLegend	Cat# 103128, RRID:AB_493715
FCM: CD45 BV605 mouse monoclonal anti-human (clone HI30), dilution 1:640	BioLegend	Cat# 304042, RRID:AB_2562106

(*Continued on next page*)

Continued

REAGENT or RESOURCE	SOURCE	IDENTIFIER
FCM: CD49D APC mouse monoclonal anti-human (clone 9F10), dilution 1:320	BioLegend	Cat# 304308, RRID:AB_2130041
FCM: CD56 PE/Dazzle 594 mouse monoclonal anti-human (clone HDC56), dilution 1:640	BioLegend	Cat# 318348, RRID:AB_2563564
FCM: CD62L BV421 rat monoclonal anti-mouse (clone MEL-14), dilution1:400	BioLegend	Cat# 104435, RRID:AB_10900082
FCM: CD62L PerCP/Cyanine5.5 mouse monoclonal anti-human (clone DREG-56), dilution 1:500	BioLegend	Cat# 304824, RRID:AB_2239105
FCM: CD66B AF700 mouse monoclonal anti-human (clone G10F5), dilution 1:100	BioLegend	Cat# 305114, RRID:AB_2566038
FCM: CD66B PE mouse monoclonal anti-human (clone 4/60c), dilution 1:200	BioLegend	Cat# 392904, RRID:AB_2750202
FCM: CD66B PE/Cyanine7 mouse monoclonal anti-human (clone G10F5), dilution 1:640	BioLegend	Cat# 305116, RRID:AB_2566605
FCM: CD8a PE/Cyanine7 mouse monoclonal anti-human (clone HIT8a), dilution 1:320	BioLegend	Cat# 300914, RRID:AB_314118
FCM: CD80 PE/Cyanine7 mouse monoclonal anti-human (clone L307.4), dilution 1:160	BD Bioscience	Cat# 561135, RRID:AB_10561688
FCM: CD86 Pacific Blue mouse monoclonal anti-human (clone IT2.2), dilution 1:160	BioLegend	Cat# 305418, RRID:AB_493663
FCM: cMET AF647 mouse monoclonal anti-human (clone 3D6), dilution 1:40	BD Bioscience	Cat# 566014, RRID:AB_2739459
FCM: CD181 (CXCR1) BV711 mouse monoclonal anti-human (clone 5A12), dilution 1:80	BD Bioscience	Cat# 743423, RRID:AB_2741496
FCM: CD182 (CXCR2) AF488 mouse monoclonal anti-human (clone 5E8/CXCR2), dilution 1:80	BioLegend	Cat# 320712, RRID:AB_492938
FCM: CXCR4 PE mouse monoclonal anti-human (clone 12G5), dilution 1:25	R&D Systems	Cat# FAB170P, RRID:AB_357076
FCM: CD184 (CXCR4) PerCP-eFluor710 rat monoclonal anti-human/mouse (clone 2B11), dilution 1:60	Thermo Fisher Scientific	Cat# 46-9991-82, RRID:AB_10670489
FCM: HLA-ABC APC mouse monoclonal anti-human (clone W6/32), dilution 1:400	BioLegend	Cat# 311409, RRID:AB_314878
FCM: HLA-DR BV711 mouse monoclonal anti-human (clone L243), dilution 1:320	BioLegend	Cat# 307644, RRID:AB_2562913
FCM: Ly6C BV711 rat monoclonal anti-mouse (clone HK1.4), dilution 1:800	BioLegend	Cat# 128037, RRID:AB_2562630
FCM: Ly6G BV605 rat monoclonal anti-mouse (clone 1A8), dilution 1:160	BioLegend	Cat# 127639, RRID:AB_2565880
FCM: Ly6G FITC rat monoclonal anti-mouse (clone 1A8), dilution 1:300	BioLegend	Cat# 127605, RRID:AB_1236488
FCM: MMP9 AF488 mouse monoclonal anti-human (clone 56129), dilution 1:80	R&D Systems	Cat# IC9111F, RRID:AB_2144867
FCM/IF: MRP-14 (S100A9) PE mouse monoclonal anti-human (clone MRP1H9), dilution 1:640 (FCM), 1:100 (IF)	BioLegend	Cat# 350706, RRID:AB_2564008
IF: anti-chicken IgG (H+L) AF647, dilution 1:500	Jackson ImmunoResearch	Cat# 703-605-155, RRID:AB_2340379
IF: anti-goat DyLight 755, dilution 1:500	Thermo Fisher Scientific	Cat# SA5-10091, RRID:AB_2556671
IF: anti-goat IgG (H+L) AF488, dilution 1:500	Thermo Fisher Scientific	Cat# A32814, RRID:AB_2762838

(*Continued on next page*)

Continued

REAGENT or RESOURCE	SOURCE	IDENTIFIER
IF: anti-mouse IgG (H+L) AF555, dilution 1:500	Thermo Fisher Scientific	Cat# A-32773, RRID:AB_2762848
IF: anti-mouse IgG (H+L) AF647, dilution 1:500	Thermo Fisher Scientific	Cat# A-31571, RRID:AB_162542
IF: anti-rabbit IgG (H+L) AF555, dilution 1:500	Thermo Fisher Scientific	Cat# A-32794, RRID:AB_2762834
IF: anti-rabbit IgG (H+L) AF755, dilution 1:500	Thermo Fisher Scientific	Cat# SA5-10043, RRID:AB_2556623
IF: anti-rat IgG (H+L) AF647, dilution 1:500	Abcam	Cat# ab150155, RRID:AB_2813835
IF: anti-sheep IgG (H+L) AF488, dilution 1:500	Thermo Fisher Scientific	Cat# A11015, RRID:AB_2534082
IF: CD15 mouse monoclonal anti-human (clone MMA), dilution 1:100	Abcam	Cat# ab17080, RRID:AB_443635
IF: CD3 mouse monoclonal anti-human (clone UCHT1), dilution 1:50	BioLegend	Cat# 300401, RRID:AB_314055
IF: CD3 FITC mouse monoclonal anti-human (clone UCHT1), dilution 1:100	BioLegend	Cat# 300406, RRID:AB_314060
IF: CD31 sheep polyclonal anti-human, dilution 1:100	R&D Systems	Cat# AF806, RRID:AB_355617
IF: CD4 rabbit monoclonal anti-human (clone EPR6855), dilution 1:100	Abcam	Cat# ab133616, RRID:AB_2750883
IF: CD45 goat polyclonal anti-human, dilution 1:100	LSBio	Cat# LS-B14248-300, RRID:AB_2889893
IF: CD45 AF647 mouse monoclonal anti-human (clone HI30), dilution 1:100	BioLegend	Cat# 304018, RRID:AB_389336
IF: CD49D rat monoclonal anti-human (clone PS/2), dilution 1:100	Bio X Cell	Cat# BE0071, RRID:AB_1107657
IF: CD68 mouse monoclonal anti-human (clone KP1), dilution 1:100	Abcam	Cat# ab955, RRID:AB_307338
IF: CD8 mouse monoclonal anti-human (clone 4B11), dilution 1:100	Bio-rad	Cat# MCA1817T, RRID:AB_323534
IF: FOXP3 rabbit monoclonal anti-human (clone SP97), dilution 1:100	Thermo Fisher Scientific	Cat# MA5-16365, RRID:AB_2537884
IF: HIF1a goat polyclonal anti-human, dilution 1:100	R&D Systems	Cat# AF1935, RRID:AB_355064
IF: HIF2a rabbit polyclonal anti-human, dilution 1:100	Abcam	Cat# ab109616, RRID:AB_11156727
IF: Ki67 AF647 rat monoclonal anti-human (clone SolA15), dilution 1:100	Thermo Fisher Scientific	Cat# 17-5698-82, RRID:AB_2688057
IF: P2RY12 rabbit polyclonal anti-human, dilution 1:600	Sigma-Aldrich	Cat# HPA014518, RRID:AB_2669027
IF: Pan-cadherin rabbit polyclonal anti-human, dilution 1:100	Abcam	Cat# ab16505, RRID:AB_443397
IF: PD-L1 rabbit monoclonal anti-human (clone SP142), dilution 1:50	Abcam	Cat# ab228462, RRID:AB_2827816
IF: CD279 (PD-1) AF647 mouse monoclonal anti-human (clone NAT105), dilution 1:100	BioLegend	Cat# 367419, RRID:AB_2721353
In vitro: Human TNF-α Neutralizing (clone D1B4) Rabbit mAb	Cell Signaling Technology	Cat# 7321S, RRID:AB_10925386
In vitro: Human/Primate IL-6 Antibody (clone 6708)	R&D Systems	Cat# MAB206, RRID:AB_2127617
In vitro: Human IL-9 Antibody, polyclonal	R&D Systems	Cat# AF209, RRID:AB_2296123
Biological samples		
Non-tumor, glioma, and brain metastasis tissue, along with matched patient blood	Centre Hospitalier Universitaire Vaudois, Lausanne, Switzerland	N/A

(*Continued on next page*)

Continued

REAGENT or RESOURCE	SOURCE	IDENTIFIER
Non-tumor, glioma and brain metastasis tissue	Memorial Sloan Kettering Cancer Center, New York, NY, USA	N/A
Buffy coats from healthy donors	Transfusion Interrégionale Croix-Rouge Suisse, Epalinges, Switzerland	N/A
Healthy donor blood	Université de Lausanne, Lausanne, Switzerland	N/A
Healthy donor blood	New York Blood Bank, New York, NY, USA	N/A
Chemicals, peptides, and recombinant proteins		
DMEM-F12 (1:1), GlutaMAX	Gibco, Thermo Fisher	Cat# 31331028
HBSS	Gibco, Thermo Fisher	Cat# 14175-095
DMEM-F12 w/o phenol red	Gibco, Thermo Fisher	Cat# 21041-025
Penicillin/Streptomycin	Gibco, Thermo Fisher	Cat# 15140122
Fetal Bovine Serum (FBS)	Gibco, Thermo Fisher	Cat# 31331028
Trypsin-EDTA (0.05%), phenol red	Gibco, Thermo Fisher	Cat# 25300062
PBS	Gibco, Thermo Fisher	Cat# 20012027
RBC Lysis Buffer (10X)	Biolegend	Cat# *00-4333-57*
Ultrapure distilled water	Invitrogen	Cat# 10977-035
Ficoll-Paque Premium	GE	Cat# 17-5442-02
Tissue-Tek® O.C.T. Compound	Tissue-Tek, Sakura Finetek	Cat# 4583
CS&T beads	BD Bioscience	Cat# 656504
2-methylbutane	Sigma-Aldrich	Cat# 50970
Methanol, 99.9%	Thermo Fisher	Cat# 176840025
Neutral Buffered Formalin	Fisher scientific, EprediaTM 5701	Cat# 22-050-104
Trizol LS	Thermo Fisher Scientific	Cat# 10296028
Tween 20	Applied Chemicals	Cat# A4974
Triton X-100	Applied Chemicals	Cat# A4975
Blocking Reagent (PNB)	Perkin Elmer	Cat# FP1020
SlowFade Diamond Antifade Mountant	Invitrogen	Cat# S36972
Fluorescence Mounting Medium	Dako, Agilent	Cat# S302380
TCEP tris(2-carboxyethyl)phosphine	Sigma	Cat# C4706
Urea	Panreac Applichem ITW reagents	Cat# A1360
Guanidium Chloride	Carl Roth	Cat# 0037.1
Glycine	Panreac Applichem ITW reagents	Cat# A1067
Bovine Serum Albumin	Jackson ImmunoResearch	Cat# 001-000-162
UltraPure™ 0.5M EDTA	Invitrogen	Cat# 15575020
Normal donkey serum	SigmaAldrich	Cat# S30-M
Luminol	Sigma	Cat# A8511-5G
Diphenyleneiodonium chloride (DPI)	Sigma	Cat# D2926-10mg
Phorbol-12-myristat-13-acetate (PMA)	Abcam	Cat# abb120297
Endothelial Cell Medium	ScienCell	Cat# 1001
Astrocyte Medium	ScienCell	Cat# 1801
Trypsin Neutralization Solution	ScienCell	Cat# 0113
Recombinant human CSF-1	R&D Systems	Cat# 216-MC-025
RLT buffer	Qiagen DNAeasy Blood&Tissue kit	Cat# 69504
Brilliant Stain Buffer	BD Bioscience	Cat# 563794

(*Continued on next page*)

Continued

REAGENT or RESOURCE	SOURCE	IDENTIFIER
Corning® Matrigel® Growth Factor Reduced (GFR) Basement Membrane Matrix, Phenol Red-free, LDEV-free	Corning	Cat# 356231
Attane™ Isoflurane	Attane	N/A
2% lidocaïne	Streuli Pharma	Cat# 784734
Bupivacaine 0.5%	Carbostesin; Aspen Pharma Schweiz	Cat# 972430
Buprenorphine 0.3 mg/ml (Temgesic)	Eumedica Pharmaceuticals AG	Cat# 6664853
Bepanthen cream	Bayer	N/A
HEPES (1M)	Gibco, Thermo Fisher	Cat# 15630056
Collagenase/Dispase®	Sigma-Aldrich	Cat# 10269638001
DNase I	Sigma-Aldric	Cat# 11284932001
Pentobarbital	CHUV Hospital, Lausanne, Switzerland	NA
Tamoxifen, ≥99%	Sigma-Aldrich	Cat# T5648
BrBzGCp2 (GLO-1 inhibitor)	MedChemExpress	Cat# HY-136684
Recombinant Human TNF-α	PreproTech	Cat# 300-01A
Recombinant Human Glyoxalase I Protein, CF	R&D Systems	Cat# 4959-GL
Interleukin-6 human	Sigma-Aldrich	Cat# SRP3096
Recombinant Human IL-9 Protein	R&D Systems	Cat# 209-ILB
Ceruloplasmin human	Sigma-Aldrich	Cat# C4519-100UN
Critical commercial assays		
Brain Tumor Dissociation Kit (P)	Miltenyi	Cat# 130-095-942
Tumor Dissociation Kit, human	Miltenyi	Cat# 130-095-929
Tumor Dissociation Kit, mouse	Miltenyi	Cat# 130-096-730
Myelin Removal Beads II kit	Miltenyi	Cat# 130-096-433
CD14 MicroBeads, human	Miltenyi	Cat# 130-050-201
Human TruStain FcX	BioLegend	Cat# 422302
Zombie NIR Fixable Viability Kit	BioLegend	Cat# 423106
eBioscience™ Foxp3 / Transcription Factor Staining Buffer Set	Thermo Fischer Scientific	Cat# 00-5523-00
CellROX™ Green Reagent, for oxidative stress detection	Thermo Fischer Scientific	Cat# C10444
4', 6- Diamidino-2-Phenylindole, Dihydrochloride (DAPI)	Life Technologies	Cat# D1306
MACSxpress Whole Blood Neutrophil Isolation Kit	Miltenyi	Cat# 130-104-434
CD66b Antibody, anti-human, Biotin, REAfinity™	Miltenyi	Cat# 130-118-983
Anti-Biotin MicroBeads UltraPure	Miltenyi	Cat# 130-105-637
Anti-Ly-6G MicroBeads UltraPure	Miltenyi	Cat# 130-120-337
Easy HLA Chimerism Whole Blood CD3 positive selection kit	Stemcell	Cat# 17871
DNeasy Blood & Tissue Kit	Qiagen	Cat# 69504
eBioscience™ Annexin V Apoptosis Detection Kits	Thermo Fischer Scientific	Cat# 88-102-72
Assay Diluent	MSD	Cat# K151AEL-1
U-PLEX Immuno-Oncology Group 1 (hu) assay	MSD	Cat# K151AEL-1
L1000 Glass Slide Human Antibody Array	RayBiotech Life	Cat# AAH-BLG-1000-4
Deposited data		
Raw data	This paper	https://joycelab.shinyapps.io/braintime/

(*Continued on next page*)

Continued

REAGENT or RESOURCE	SOURCE	IDENTIFIER
Human reference genome hg38, GENCODE v36	Gencode	https://www.gencodegenes.org/human/release_36.html
scRNA-seq NSCLC TAN dataset	Zilionis et al.[36]	https://singlecell.broadinstitute.org/single_cell/study/SCP739/single-cell-transcriptomics-of-human-and-mouse-lung-cancers-reveals-conserved-myeloid-populations-across-individuals-and-species
scRNA-seq NSCLC TAN dataset	Salcher et al.[37]	https://zenodo.org/record/7227571
scRNA-seq Melanoma-BrM TAN dataset	Alvarez-Breckenridge et al.[38]	https://singlecell.broadinstitute.org/single_cell/study/SCP1493/microenvironmental-correlates-of-immune-checkpoint-inhibitor-response-in-human-melanoma-brain-metastases-revealed-by-t-cell-receptor-and-single-cell-rna-sequencing
STRING Protein-Protein-Interaction database, version 11.5	Szklarczyk et al.[77]	https://string-db.org
Experimental models: Cell lines		
Human: human brain microvascular endothelial cells (HBMEC)	ScienCell	Cat# 1000
Human: Primary human astrocytes (HA)	ScienCell	Cat# 1800
Human: human umbilical vein endothelial cells (HUVEC)	Prof. T. Petrova	N/A
MMTV-PyMT (murine mammary tumor virus; Polyoma middle T antigen) 99LN BrM3	Croci et al.[78] Prof. J.A. Joyce	Available upon request
PDGFB-HA: DF1 chicken fibroblasts (ATCC) with RCAS viral vector expressing PDGFB-HA	Dr. Tatsuya Ozawa and Dr. Eric Holland	N/A
shP53 DF1: DF1 chicken fibroblasts (ATCC) with a short hairpin against murine p53 (shP53)	Dr. Tatsuya Ozawa and Dr. Eric Holland	N/A
Experimental models: Organisms/strains		
C57BL/6J mice	The Jackson Laboratory	RRID:IMSR_JAX:000664
Ly6G^{CreERT2} mice (C57BL/6J background)	Ballesteros et al.[20]	N/A
Nestin-Tv-a mice (C57BL/6J background)	Holland et al.[79]	N/A
Software and algorithms		
FlowJo, version 10.8.2	BD bioscience	https://www.flowjo.com/
GraphPad Prism v9.4.1	GraphPad Software	https://www.graphpad.com/scientific-software/prism/
ZEN software	Zeiss	https://www.zeiss.com/microscopy/en/products/software.html
VIS Image Analysis, version 2022.04	Visiopharm	https://www.visiopharm.com/
QuPath version 0.3.2	Bankhead et al.[80]	https://qupath.github.io/
StarDist	Schmidt et al.[81]	https://github.com/stardist/stardist
Python version 3.9	Python	https://www.pyhton.org
R environment, version 4.1.1	The R Foundation	https://www.r-project.org/
RStudio, version 2023.03.0	RStudio	https://www.posit.co/
Matlab (R2022a)	MathWorks	https://www.mathworks.com/products/matlab.html
STAR aligner, version 2.7.7a	Dobin et al.[82]	https://github.com/alexdobin/STAR

(*Continued on next page*)

Continued

REAGENT or RESOURCE	SOURCE	IDENTIFIER
RSEM version 1.3.3	Li and Dewey[83]	https://deweylab.github.io/RSEM/
Spatstat R package version 2.3-4	Baddeley et al.[84]	http://spatstat.org
edgeR version 3.32.1	Robinson et al.[85]	https://bioconductor.org/packages/release/bioc/html/edgeR.html
limma version 3.46.0	Ritchie et al.[86]	https://bioconductor.org/packages/release/bioc/html/limma.html
sva version 3.38.0	Leek and Storey[87]	https://bioconductor.org/packages/release/bioc/html/sva.html
ClusterProfiler R package version 3.18.1	Wu et al.[88]	https://bioconductor.org/packages/release/bioc/html/clusterProfiler.html
scDataviz R package	Blighe [89]	https://github.com/kevinblighe/scDataviz
ggplot2 R package version 3.3.6	Wickham[90]	https://ggplot2.tidyverse.org
Monocle3 R package version 1.0.0	Trapnell et al.[91]	https://cole-trapnell-lab.github.io/monocle3/
Slingshot R package version 2.2.0	Street et al.[92]	https://github.com/kstreet13/slingshot
Cutadapt version 2.3	Martin[93]	https://github.com/marcelm/cutadapt/blob/v2.3/doc/index.rst
Burrows-Wheeler aligner version 0.7.17	Li and Durbin[94]	https://github.com/lh3/bwa
SAMtools version 1.8	Danecek et al.[95]	https://github.com/samtools/samtools/
Picard tools version 2.9.0	Broad Institute	https://broadinstitute.github.io/picard/
ENSEMBL Variant Effect Predictor version 96	McLaren et al.[96]	https://www.ensembl.org/info/docs/tools/vep/index.html
ComplexHeatmap R package version 2.10.0	Gu et al.[97]	https://jokergoo.github.io/ComplexHeatmap-reference/book/
iGraph R package version 1.2.6	Csardi and Nepush[98]	https://igraph.org
lme4 R package version 1.1-32	Bates et al.[99]	https://github.com/lme4/lme4/
lmerTest R package version 3.1-3	Kuznetsova et al.[100]	https://github.com/runehaubo/lmerTestR
Other		
gentleMACS Octo Dissociator	Miltenyi	Cat# 130-095-937
gentleMACS C Tubes	Miltenyi	Cat# 130-096-334
LS Columns	Miltenyi	Cat# 130-042-401
SepMate-50 tubes	StemCell	Cat# 85450
PermaLife Cell Culture Bags	OriGen Biomedical	Cat# PL30-2G
LSR II flow cytometer	BD Bioscience	N/A
Fortessa flow cytometer	BD Bioscience	N/A
FACSAria III, flow cytometer & cell sorter	BD Bioscience	N/A
Axio Scan.Z1 slide scanner	Zeiss	N/A
Omni Tissue Homogenizer (TH)	Omni International	Cat# TH220
Tissue-Tek Cryomold	Sakura	Cat# 4557
Hydrophobic pen	Daido Sangyo, Plano	Cat# 22304
Coverslip	ThermoFisher	Cat# BB02400500A113FST0
Microscope slide	Fisherbrand	Cat# 12-550-15
Illumina NovaSec 6000 sequencer	Illumina	N/A
MESO QuickPlex SQ120 instrument	Meso Scale Discovery	N/A
Nunc™ MicroWell™ 96-Well, Nunclon Delta-Treated, White Flat-Bottom Microplate	ThermoFisher	Cat# 136101
Microplate reader Infinite® 200 PRO Tecan	Tecan	N/A

(*Continued on next page*)

Continued

REAGENT or RESOURCE	SOURCE	IDENTIFIER
Trucount Absolute Counting Tubes	BD Bioscience	Cat# 340334
Corning® 96-well Clear Round Bottom TC-treated Microplate, Individually Wrapped, with Lid, Sterile	Corning	Cat# 3799
Corning® 96-well Clear Flat Bottom Polystyrene TC-treated Microplates, Individually Wrapped, with Lid, Sterile	Corning	Cat# 3596
BD Vacutainer	BD Bioscience	Cat# 368861
Vetbond tissue adhesive	3M	Cat# 1469SB

RESOURCE AVAILABILITY

Lead contact

Further information and requests for resources and reagents should be directed to and will be fulfilled by the lead contact, Prof. Johanna Joyce (johanna.joyce@unil.ch).

Materials availability

This study did not generate new unique reagents.

Data and code availability

Bulk RNA-seq count data generated and used for this study can be queried and downloaded at: https://joycelab.shinyapps.io/braintime/

Due to strict privacy protection, the raw RNA-seq data will be made available when possible. Future users can contact the corresponding author for access to the raw, unprocessed RNA-seq data, and those requests will then be individually reviewed by the relevant institutional committees. This paper does not report original code.

EXPERIMENTAL MODEL AND STUDY PARTICIPANT DETAILS

Human subjects

All procedures in this study involving the use of tissues derived from human participants were in accordance with the ethical standards of the national research committees and the declaration of Helsinki.

For detailed information related to the cohort of human participants (e.g. sex, age, and treatment), please see Tables S1A–S1C. Informed consent was obtained for all human subjects participating in this study. The processing of non-tumor and tumor tissue at the Biobank of the Brain and Spine Tumor Center (BB_031_BBLBGT) at the Centre Hospitalier Universitaire Vaudois (CHUV, Lausanne, Switzerland), was approved by the Commission cantonale d'éthique de la recherche sur l'être humain (CER-VD, protocol PB 2017-00240, F25 / 99). Similarly, the processing of tumor tissue collected at Memorial Sloan Kettering Cancer Center (MSKCC, New York, NY, USA) was approved by the institutional review board (IRB, protocols #IRB #06-107, #14-230). Non-tumor brain surgeries were performed on patients with therapy-resistant focal epilepsy, as part of the clinical management. Brain tumor resections were performed to either aid in diagnosing the origin of the lesion or as part of the therapeutic strategy. Diagnostic identification of the brain (tumor) tissue was performed by a trained pathologist as part of the standard of care at the CHUV or MSKCC.

Matched blood of brain tumor-bearing patients was collected at the time of the brain surgery as part of the ethical permit stated above (CER-VD, protocol PB 2017-00240, F25 / 99). Whole blood collection from identified healthy donor volunteers was approved by CER-VD (protocol 2018-00492). Buffy coats from anonymous voluntary donors were obtained from the Transfusion Interrégionale, Croix-Rouge Suisse (Epalinges/Lausanne, Switzerland).

All tissue specimens were coded before further handling in accordance with patient privacy regulations.

Primary cell cultures

Human

Brain tumor-derived cell lines were generated by plating single-cell suspensions of dissociated tumors in a cell culture flask at a density of 2 x 10^6 cells per ml in DMEM-F12 (1:1) +Glutamax (Gibco, cat. no. 31331028) +10% FCS (Gibco, ThermoFisher, cat. no. 10270106) +1% penicillin/streptomycin (P/S, Gibco, cat. no. 15140122) in an incubator at 37°C and 5% CO_2. Cells were passaged using 0.05% Trypsin-EDTA (Gibco, cat. no. 25300062) once the cells reached 70% confluency in the cell culture flask. Cell lines were validated using whole exome sequencing (WES) of both snap frozen tumor tissue and matched tumor cell lines. For detailed information (e.g. sex, age, treatment) related to brain tumor-derived cell lines, please see Table S1C.

Primary human astrocytes (HA; ScienCell, cat. no. #1800) and human brain microvascular endothelial cells (HBMEC; ScienCell, cat. no. #1000) were cultured according to the vendor's instructions. Human umbilical vein endothelial cells (HUVECs) were kindly provided by the laboratory of Prof. T. Petrova, and were cultured in DMEM-F12 (1:1) +GlutaMAX +10% FBS +1% P/S. Healthy donor monocyte-derived macrophages (MDMs) were derived from peripheral blood mononuclear cells (PBMCs) from buffy coats, isolated using a Ficoll (GE Healthcare, cat. no. 17-1440-02) gradient and SepMate tubes (StemCell, cat. no. 85450). Monocytes were selected using MACsorting by CD14 MicroBeads (Miltenyi, cat. no. 130-050-201) and differentiated into macrophages by culture in Teflon-coated bags (OriGen Biomedical, cat. no. PL30-2G) for 7 days in DMEM-F12 (1:1) +GlutaMAX +10% FBS +1% P/S with the addition of 10 ng/ml recombinant human CSF-1 (R&D Systems, cat. no. 216-MC-025).

Murine

To generate murine breast-to-brain metastasis (BrM) a brain-homing breast tumor cell line, MMTV-PyMT (murine mammary tumor virus; Polyoma middle T antigen)-BrM3, was used (C57BL/6J background).[78] This cell line was initially derived from a murine breast-to-lymph node metastasis and consequently passaged three times *in vivo* in female C57BL/6J WT mice for brain-homing capacity via intracardiac injections. The PyMT-BrM3 cell line was maintained in DMEM-F12 (1:1) +GlutaMAX medium +10% FCS +1% P/S and passaged using 0.05% Trypsin-EDTA once the cells reached 70% confluency.

Transfected DF1 chicken fibroblasts

DF1 chicken fibroblasts (ATCC), which were previously transfected with an RCAS viral vector expressing PDGFB-HA or a short hairpin against murine p53 (shP53) were kindly provided by Dr. Tatsuya Ozawa and Dr. Eric Holland.[101,102] The PDGFB-HA and p53 DF1 cells were cultured in DMEM-F12 (1:1) +GlutaMAX medium +10% FCS +1% P/S under standard conditions.

Mouse models

All experiments performed in this study were approved by the local Institutional Animal Care and Use Committees of the University of Lausanne and the Canton Vaud, Switzerland (protocol numbers VD3314, VD3444, VD3688). Experiments involving the development of breast(-BrM) tumors were performed in 6-10-week-old female *Ly6G*^{CreERT2} mice in a C57BL/6J background[20] (generously provided by Prof. Andrés Hidalgo) or in female C57BL/6J wildtype mice. Experiments involving the development of gliomas were performed in 4.5–7-week-old male and female *Ly6G*^{CreERT} C57BL/6J mice bred to Nestin-Tv-a mice or in Nestin-Tv-a wildtype mice[79] (generously provided by Dr. Eric Holland). All mice were housed in the Agora In Vivo Center (AIVC) animal facility in individually ventilated cages. Mice were housed under a 12-hour light/dark schedule at 22°C, in the presence of 2-5 cage mates. Standard autoclaved lab diet and water were provided.

METHOD DETAILS

Human brain (tumor) enzymatic digestion

Single cell suspensions of human non-tumor and brain tumor tissue were obtained after enzymatic digestion as described in Maas et al.[23] (Module 2). In brief, enzymatic digestion was performed using the "Brain Tumor Dissociation Kit (P)" (BTDK, Miltenyi, cat. no. 130-095-942) for non-tumor brain tissue and gliomas, for BrMs the "Tumor Dissociation Kit, human" (Miltenyi, cat. no. 130-095-929) was used according to the manufacturer's protocol. For non-tumor brain and glioma samples, enzymatic digestion was followed by myelin removal using Myelin Removal Beads II according to the manufacturer's protocol (Miltenyi, cat. no. 130-096-433). Both tumor single cell suspensions and whole blood were RBC-lysed prior to downstream processing using 1x RBC lysis buffer (Biolegend, cat. no. 00-4333-57, diluted to 1X in deionized water) according to the manufacturer's protocol. Single-cell suspensions were used for flow cytometric (FCM) analysis, bulk-RNA sequencing (RNA-seq) after fluorescence-activated cell (FAC)-sorting, *ex vivo* functional analysis as well as the generation of tumor-derived cell lines.

Flow cytometry and FACS

FCM and FACS were performed as described in Maas et al.[23] (Module 2a, see key resources table for the antibodies used). In brief, cells were stained in 100ul ZombieNIR Fixable Viability dye (Biolegend, cat. no. 423106) for 20 min at RT in the dark, followed by 10 min incubation at RT in the dark with Fc receptor blocking solution (5 ul added per sample, BioLegend, cat. no. 422302). Next, 1-5 ul of 2x antibody staining mix in Brilliant Stain Buffer (BD; cat. no. 563794) was added and incubated for 15 min at 4 °C in the dark. After washing the cells with FACS buffer (PBS (Gibco, ThermoFisher, cat. no. 20012027), 0.5% BSA (Jackson ImmunoResearch, cat. no. 001-000-162), 2mM EDTA (Thermo Fischer Scientific, cat. no. 15575020)) samples were either directly acquired using a flow cytometer or fixed according to the manufacturer's protocol (eBioscience Foxp3 / Transcription Factor Staining Buffer Set, Thermo Fischer Scientific, cat. no. 00-5523-00). The desired cell populations were directly purified using FACS in 750 ul Trizol LS (Sigma-Aldrich, cat. no. T3934) and snap-frozen in liquid nitrogen. Validation of the sorting purity (>97%) was assessed by re-acquisition of the sorted populations by FCM.[23] Technical consistency of the flow cytometer setup, allowing for comparison of data across different timepoints, was ensured by saving a baseline measurement on the flow cytometer used on the first day of acquisition. On consecutive dates, the baseline was reloaded and adapted based on the read-out of the acquired CS&T beads (BD, cat. no. 656504) in the different channels, maximizing a consistent read-out. For the measurement of ROS by FCM CellROX green (Thermo Fischer Scientific, cat. no. C10444) was used according to the manufacturer's protocol.

Immunofluorescence staining of tissue sections

Human tissue was frozen in optimal cutting temperature (OCT) compound (Tissue-Tek, Sakura Finetek, cat. no. 4583) as described in Maas et al.[23] (Module 1). In short, a 2-methylbutane (Sigma-Aldrich, cat. no. 50970) container was placed on dry ice to ensure a temperature of -80˚C. Tumor tissue (minimum size of 8mm^3) was placed in a cryomold with OCT and dipped in chilled 2-methylbutane for 2-3min. OCT blocks were stored at -80˚C until they were sectioned using a cryostat. 10-um thick frozen sections were used for both standard single-round immunofluorescence (IF) staining, as well as sequential IF. Standard single-round IF was performed on non-tumor brain tissue, *IDH* mut and WT gliomas, and BrMs, and described in Maas et al.[23] (Module 1, and below) and for sequential IF up to 7 rounds, frozen tissue slides from *IDH* WT gliomas and BrMs were used. Sections were air-dried for 20-30 min in a laminar flow hood. Slides for single-round IF were fixed for 10 min in 99.9% methanol (Thermo Fisher, cat. no. 176840025), prechilled to -20˚C. Slides used for sequential IF were fixed in 10% Neutral Buffered Formalin (Fisher Scientific, Epredia™ 5701, Cat. No. 22-050-104) for 40 min at RT. For both single round and sequential IF the slides were then rehydrated and washed 3x 5 min in PBS while gently rocking. A ring was drawn around the tissue using a hydrophobic pen (Daido Sangyo, Plano, cat. no. 22304). Any potential autofluorescence signal was quenched by adding 100 ul glycine 10mM (Panreac Applichem ITW reagents, A1067) diluted in PBS for 10 min at RT. Slides were washed 2x 5 min in PBS-0.2%Tween (PanReac AppliChem cat. no. A4974). Tissue was permeabilized with PBS-0.2%Triton (PanReac AppliChem, cat. no. A4975) for 3h at RT if non-tumor brain and *IDH* mut gliomas slides were included for the study, otherwise a 10 min permeabilization sufficed for *IDH* WT and BrM slides. Next, slides were washed 2x 5 min with PBS-0.2%Tween. The slides were incubated with blocking buffer (1x Blocking Reagent (PerkinElmer, cat. no. FP1012; 'PNB') + 0.5% Tween + 10% normal donkey serum (SigmaAldrich, cat.no. S30-M) + 2% BSA (Jackson ImmunoResearch, cat. no. 001-000-162)) filtered through a 0.22-um filter, for 1 hour in a humidified chamber. Primary antibodies (see key resources table for the antibodies used) were diluted in antibody dilution buffer (1x PNB + 0.5% Tween + 10% normal donkey serum; 0.22-um filtered before use) for 3h in a humidified chamber on a shaker at RT. Slides were then washed 3x 5 min, before adding fluorophore-conjugated secondary antibodies and a nuclear detection marker 4', 6- Diamidino-2-Phenylindole, Dihydrochloride (DAPI, Life technologies, D1306) in antibody dilution buffer to the slides (see key resources table for the antibodies used). Slides were placed in a humidified chamber for 1 hour at RT. Staining with secondary antibodies alone was used as the control. The slides were washed 6x 10 min with PBS-0.2%Tween, and a final wash was performed with PBS.To mount the slides for single-round IF, 2 drops of fluorescence mounting media (Dako, cat. no. S302380) were added to the tissue. Sequential IF slides were mounted by adding 20 ul SlowFade Diamond Antifade Mountant (Thermo Fischer Scientific, cat. no. S36972) to each tissue. Then a coverslip (ThermoFisher, cat. no. BB02400500A113FST0) was carefully placed on top of the slides. The fluorescent signal was acquired using the Axio Scan.Z1 slide scanner (Zeiss), with a Colibri 7 LED light source (Zeiss) and a Plan-Apochromat 20x/0.8 DIC M27 cover slip-corrected objective (Zeiss). For sequential IF, the coverslip was carefully removed after acquisition by leaving the slide upright in PBS to let the coverslip slide off. The slides were washed 3x 5 min in PBS, prior to elution in freshly prepared tris(2-carboxyethyl)phosphine (TCEP)-based elution buffer (0.5 M glycine + 3 M guanidium chloride (Carl Roth, cat. no. 0037.1) + 2 M urea (Panreac Applichem ITW reagents, cat. no. A1360) + 40 mM TCEP (Sigma, cat. no. C4706) in ddH_2O) for 5 min on a rocker at RT.[103] Finally, slides were washed 3x 5 min in PBS-Tween, before restarting the staining process by returning to adding blocking buffer to the slides, and following all the consecutive steps detailed above.

Image analysis and cell type identification

Standard single-round IF

Image quantification was performed using the VIS Image Analysis software (Visiopharm, v2022.04) on preprocessed images applying ZEN software (stitching and z-stacking of the images). Cellular identification, as well as perivascular niche (PVN) characterization, were performed as described in Klemm et al.[10] Briefly, the tissue outline was detected by applying a 21 pixel mean DAPI filter. Nuclear detection was based on the DAPI watershed signal and filtered by area to exclude anomalies. The nuclear label was expanded by 5 pixels to capture nuclear and cytoplasmic fluorescent signal. A hierarchical decision tree with manually set thresholds was applied to identify the different cell types. Vessels were identified using a separate mask based on pixel intensity of the CD31 signal. Nuclear classifiers were excluded unless their signal exceeded the threshold for CD31. By generating an ROI around the vessels at a 20 um distance, a perivascular niche (PVN) region was created.

Sequential IF

Image preprocessing was performed using ZEN software. The images of different rounds of staining were stitched, and background subtraction was performed using the rolling ball method with a radius of 75.[104] Using the signal obtained from single staining of the tissue with DAPI alone allowed for the subsequent subtraction of autofluorescence signal. Autofluorescence subtraction and alignment of the final image made from the sequential rounds of staining were performed in a Python (v3.9) library script (Watson, Joyce et al., unpublished data).

Image quantification was performed using QuPath (v0.3.2) open-source image analysis software.[80] Tumor tissue was detected within each sample using the "Pixel classifier" command. First, a training image made of single regions of interest (ROIs) drawn in each sample was generated. The "Pixel classifier" was trained on these images, using a positive detection class for tissue detection. Then, the trained pixel classifier was applied to the entire image dataset, followed by cleanup of the resulting binary image by morphological operations. Nucleus detection was performed by StarDist, a deep-learning-based method from Schmidt et al., using the dsb2018_heavy_augment.pb model.[81] A cell expansion value of 3 was used and subsequently, area identification (PVN and

vessels) was performed with the ''Pixel classifier'' command according to the same method described above. Finally, cell identification was performed using QuPath's ''Object classifier'' command. Training was performed on 40% of the ROIs and validated on the remaining 60%. A classifier was generated from one or several mutually exclusive markers. Training of the classifier was based on annotations (minimum 10 annotations per class). Selected features for training included all marker measurements. Composite classifiers generated from sequentially added classifiers were created to allow final cell identification. These classifiers were applied to the entire project and data export in.csv format for subsequent analysis in R (v4.4.1). Filtering of cells using a diameter size of > 4 um and < 12.5 um, detected nuclei probability > 0.65, as well as filtering of the relevant final cell populations, was performed in R.

Nearest neighbor distance and neighborhood analysis of sequential IF data

Nearest neighbor distance from different T cell populations and $CD8^+$ T cells stratified by PD-1 expression to TANs in *IDH* WT gliomas and BrMs, was assessed using the spatstat R package (v2.3-4).[105] Neighborhood analysis of PD-1^+ $CD8^+$ T cells and TANs was performed based on the occurrence of cells within a 20μm radius of the border of the nuclei, calculated using the radius of individual nuclei.

RNA-seq analysis

Isolation and sequencing of RNA was performed by Genewiz (South Plainfield, New Jersey, USA) using chloroform extraction and isopropanol precipitations as previously described.[10,23] The SMART-Seq preparation kit (CloneTech) was used to generate RNA-seq libraries and fragmented using the Nextera XT kit (Illumina). Sequencing of paired end, 100 or 150 base pair and single end 100 base pair, was performed on an Illumina HiSeq 2500 (Illumina).

Alignment of RNA-seq reads was performed using STAR (v2.7.7a)[82] and quantified using RSEM (v1.3.3).[83] Human genome v38 was used with GENCODE v36 annotation. Raw counts of transcripts with the same gene symbol were pooled. All genes were hierarchically clustered using Ward distance, and the expression heatmap was visually examined to identify a major branch containing a non-informative expression pattern. Non-protein coding genes, pseudogenes, predicted genes, genes with less than 1 FPKM in at least one sample in a sample group (tissue/disease group), and genes with low variance were filtered out. A total of 16,052 genes were retained and their expression was normalized between samples using the TMM method (edgeR v3.32.1[85]) and $\log_2$ transformed with voom (limma v3.46.0[86]). Batch effect was corrected for with ComBat (sva v3.38.0[87]). Differential expression was computed using limma (v3.46.0).[86] To reduce the potential bias introduced by any contaminating tumor cells ($CD45^-$ cells), genes with higher expression in the $CD45^-$ cells vs. neutrophils in the leading comparison group were filtered out if they additionally were found to be significantly differentially expressed in $CD45^-$ cells, $CD4^+$ T cells or $CD8^+$ T cells within the same comparison. Genes with p.adj value <0.05 and -1>LFC>1 are called significantly differentially expressed in all comparisons except when non-tumor brain (n=5) was one of the comparison groups, then genes with p-value <0.005 and -1>LFC>1 were called significantly differentially expressed. Pathway analyses (ORA and GSEA) were performed using clusterProfiler R package (v3.18.1).[88] For analysis across the major TME populations, T cells contain both $CD4^+$ T cells and $CD8^+$ T cells.

Mouse tumor models

Breast-BrM model

For the development of breast-BrMs in immunocompetent mice, 6-10-week-old female *Ly6G*^{CreERT2} mice or WT mice were anesthetized using isoflurane inhalation (O_2 + 2% isoflurane) and shaved on their chest. Mice were placed with their back down on a heating pad, and 1 x 10^5 PyMT-BrM3 cells resuspended in 100ul HBSS (Gibco, cat. no. 14175-095) were injected in the left cardiac ventricle. Mice were monitored weekly by magnetic resonance imaging (MRI).

Primary breast tumor model

6-10-week-old female *Ly6G*^{CreERT2} mice or WT mice were anesthetized using isoflurane inhalation (O_2 + 2% isoflurane) and placed with their back on a heating pad. 7 x 10^3 PyMT-BrM3 cells were resuspended in HBSS and mixed 1:1 with Matrigel (Corning, cat. no. 356231) in 100 ul total volume. Cells were injected in the right abdominal mammary fat pad (MFP). Mice were monitored 3x per week to assess the tumor size by calipers measurement.

Glioma tumor model

4.5 to 7 week-old male and female immunocompetent *Ly6G*^{CreERT};Nestin-Tv-a mice or Nestin-Tv-a mice were used to generate primary brain tumors using the RCAS system as previously described.[106,107] In brief, mice were anesthetized using isoflurane inhalation (O_2 + 2% isoflurane), and a mixture of 0.5% bupivacaine (Carbostesin; Aspen Pharma Schweiz, cat. no. 972430) and 2% lidocaïne (Streuli Pharma, cat. no. 784734) was applied as a local analgesic (50 ul per mouse), and 0.3 mg/ml buprenorphine (Temgesic; Eumedica Pharmaceuticals AG, cat. no. 6664853) was injected subcutaneously as a systemic analgesic (100 ul per mouse). Using a stereotactic apparatus, transfected DF1 cells were injected into the right frontal cortex (2 mm frontal, 1.5 mm lateral from bregma, 2 mm deep). Mice were injected with a 1:1 mixture of PDGFB-HA and shP53 DF1 cells, for a total of 3 x 10^5 DF1 cells intracranially. The skin of the skull was sealed using Vetbond tissue adhesive (3M, cat. no. 1469SB). The mouse was placed on a heating pad and monitored until fully recovered from anesthesia. Finally, Bepanthen cream (Bayer) was applied on the site of the incision prior to placing the animal back in the cage. Mice were carefully monitored, and tumor development was assessed by weekly MRI.

Tumor-bearing *Ly6G*^{CreERT} and *Ly6G*^{CreERT};Nestin-Tv-a mice were injected intraperitoneally with 400 ul of 10 mg/ml Tamoxifen (Sigma-Aldrich, cat. no. T5648), 0-8 days prior to sacrificing to follow the decay of iLy6G $TdTomato^+$ neutrophils in different organs.

Mouse tissue analysis

Whole blood was collected from mice prior to sacrifice via the submandibular vein. Mice were euthanized by terminal anesthesia by intraperitoneal injection of pentobarbital (150 mg/kg; CHUV Hospital, Lausanne, Switzerland), followed by transcardial perfusion with PBS. Spleen, femur, lungs, mammary fat pad and brain were resected from each mouse and placed on ice. Single cell suspensions of the different organs were obtained using the following methods: i) The spleen was smashed through a 70-um cell strainer. ii) The bone marrow was flushed out of the femur by cutting off the crown of the bone on one end, placing the bone upside-down into a pierced 0.2 mL vial inside a 1.5 mL vial and centrifuging for 10s at maximum velocity in an Eppendorf centrifuge. iii) Lung tissue was cut in 1 mm^3 pieces, resuspended in digestion mix (HEPES buffer (Gibco, cat. no. 15630056) + 2mg/ml Collagenase D (Sigma-Aldrich, cat. no. 10269638001) + 80U/ml DNase I (Sigma-Aldrich, cat. no. 11284932001)) and transferred to a gentleMACS™ C tube (Miltenyi, cat. no. 130-096-334). The C tube was placed in the gentleMACS Dissociator (Miltenyi, cat. no. 130-096-427) and following programs were run consecutively: "m_lung_02_01" (165 rounds per run (rpr) for 0.36 s at RT), 1500 rpr for 30 min at 37°C and finally 2079 rpr for 37s at RT. The digested tissue was filtered through a 70-um cell strainer. iv) Brain (tumor) and MFP (tumor) tissue was cut in 1 mm^3 pieces, placed in a C-tube and resuspended in Tumor Dissociation Kit, mouse (TDK, Miltenyi, cat. no. 130-096-730), according to the manufacturer's instructions. The C tube was placed in the GentleMACS dissociator and the "37C_m_TDK_1" (1081 rpr at 37°C for ~41 min) digestion program was run. The digested (tumor) tissue was filtered through a 40-um cell strainer. For healthy brain tissue, subsequent myelin removal using the Myelin Removal Beads II kit (Miltenyi, cat no. 130-096-433) was performed according to the manufacturer's instructions. Apart from healthy brain, all tissues were subjected to red blood cell lysis (Biolegend, cat. no. 00-4333-57, diluted to 1X in deionized water) prior to FCM staining.

Mathematical modeling of mean neutrophil lifetime

To assess neutrophil mean lifetimes, the proportion of $tdTomato^+$ neutrophils was normalized to the maximum proportion measured 0-8 days post tamoxifen injection. To track neutrophils in each tissue, an age-structured mathematical model was developed that incorporated the phenotypic heterogeneity of neutrophils. Let $u = u(t,a)$denote the density of neutrophils which, at time t, have an age a. The age varies in the interval$a \in [0, a_{max}]$, where $a_{max}$is the maximum age (or maximum life span) that a neutrophil could have. To describe the temporal dynamics of their age distribution, the following age-structured model, via a linear first-order partial differential equation, was used:

$$\frac{\partial u}{\partial t} + \frac{\partial u}{\partial a} = -\frac{u(t,a)}{\tau(a)} + \varphi(t,a). \quad \text{(Equation 1)}$$

The left-hand side of (Equation 1) represents the temporal change in the number of neutrophils and their age. The first term on the right-hand side accounts for neutrophil death. The death time, $\tau(a)$, generally depends on neutrophil age. The addition of the flux $\varphi(t, a)$addresses the net effect of neutrophils entering and/or leaving the tissue. The total number of neutrophils at time t, irrespective of age, is given by the following integral:

$$n(t) = \int_0^{a_{max}} u(t,a)\, da. \quad \text{(Equation 2)}$$

When calculating the mean lifetime, τ_{LT}, of neutrophils in the context of one synchronous wave of neutrophils after tamoxifen administration, the survival function $S(a)$, with $a \in [0, a_{max}]$ can be applied, yielding the fraction of neutrophils that survive to an exact age a:

$$\tau_{LT} = \int_0^{a_{max}} S(a)\, da. \quad \text{(Equation 3)}$$

As $S(a)$is not available, an effective probability density function has been introduced here based on the solution to (Equation 1):

$$\tau_{LT}(t) = \frac{\int_0^{a_{max}} a\, u(t,a)\, da}{n(t)}. \quad \text{(Equation 4)}$$

Since (Equation 4) depends on time t, computing a representative mean lifetime requires the temporal average of $\tau_{LT}(t)$ leading to the following final formula:

$$\langle \tau_{LT} \rangle = \frac{\int_0^{\infty} \tau_{LT}(t)\, n(t)\, dt}{\int_0^{\infty} n(t)\, dt}. \quad \text{(Equation 5)}$$

Assuming that at time $t = 0$ no neutrophils of any age have yet arrived at tissue i, we have the initial condition $u(0,a) = 0$. Thus, the exact solution to (Equation 1) is:

$$u(t,a) = e^{-\int_0^t \frac{d\xi}{\tau(a-\xi)}} \int_0^t \varphi(\xi, a - t + \xi)\, e^{\int_0^{\xi} \frac{d\eta}{\tau(a-t+\eta)}}\, d\xi. \quad \text{(Equation 6)}$$

In the nonlinear regressions shown in Figures 5D, 5E, and S5E, we used for the neutrophil death time $\tau(a) = \tau_i$. Furthermore, to describe the synchronous wave of neutrophils recruited at tissue i, a bivariate Gaussian profile was assumed for the flux function in (Equation 1):

$$\varphi(t,a) = \varphi_0 \exp\left[-\frac{1}{2(1-\rho^2)}\left(\frac{(t-t_i)^2}{\sigma_t^2} - \frac{2\rho(t-t_i)(a-a_i)}{\sigma_t\sigma_a} + \frac{(a-a_i)^2}{\sigma_a^2}\right)\right]. \quad \text{(Equation 7)}$$

The parameter set, comprising τ_i, t_i, a_i, σ_t, σ_a and ρ (notice that $\varphi_0$was not needed), was estimated from the measured data for the proportion of tdTomato$^+$ neutrophils in both non-tumor and PyMT-BrM3-bearing mouse brains, together with the model Equations 1, 2, 3, 4, 5, 6, and 7 described above. The standard deviation $\delta\tau_{LT}$ of the mean lifetime $\langle\tau_{LT}\rangle$ was computed via

$$\delta\tau_{LT}{}^2 = \frac{\int_0^\infty (\tau_{LT}(t) - \langle\tau_{LT}\rangle)^2\, n(t)\, dt}{\int_0^\infty n(t)\, dt}. \quad \text{(Equation 8)}$$

To perform the regression analysis, we defined a mean squared error function in terms of the normalized total number of neutrophils for the different datasets and the values predicted by our model Equation 2 at the specific measured times. When using the neutrophil death time $\tau(a) = \tau_i$, exact closed-form expressions for (Equation 6) were obtained. All remaining integrals entering in Equations 2, 5 and 8 were computed numerically using Matlab (R2022a) global adaptive quadrature function integral.

Murine PBN and TAN isolation

Whole blood from healthy and tumor-bearing mice was collected by intracardiac aspiration into a BD Vacutainer tube (BD, cat. no. 368861) after post-terminal anesthesia was administered. Whole blood and enzymatically digested brain tumors were lysed via red blood cell lysis (Biolegend, cat. no. 00-4333-57, diluted to 1X in deionized water) for 10min at RT. Neutrophils were isolated using Magnetic-activated cell sorting (MACS) where samples were subjected to positive selection via anti-Ly-6G MicroBeads UltraPure magnetic bead isolation (Miltenyi, cat. no. 130-120-337) according to the manufacturer's instructions. This allowed to extract both peripheral blood neutrophils (PBNs) from whole blood and tumor-associated neutrophils (TANs) from the dissociated brain tumors.

Human PBN and TAN isolation

Whole blood from healthy donors (HD) and patients was collected in BD Vacutainer tubes (BD 368861). PBNs were isolated using the MACSxpress Whole Blood Neutrophil Isolation Kit (Miltenyi, 130-104-434) according to the manufacturer's instructions, followed by red blood cell lysis for 10 min at RT (Biolegend, 00-4333-57, diluted to 1X in deionized water). TANs were isolated from enzymatically digested human brain tumors using Magnetic-activated cell sorting (MACS) as described in Maas et al.[23] (Module 3). Briefly, a positive selection method was applied by adding 1 ul anti-human CD66B-Biotin antibody (Miltenyi, cat. no. 130-118-983) to 100 ul of the enzymatically digested brain tumor suspension and incubated for 10 min at 4 ℃. After washing with FACS buffer 1 x 10^8 cells were resuspended in 80 ul FACS buffer. 20 ul Anti-Biotin MicroBeads UltraPure (Miltenyi, cat. no. 130-105-637) were added per 1 x 10^7 cells, mixed well, and incubated for 15 min at 4 ℃. The cell suspension was washed in 1-2 ml of FACS buffer and up to 1 x 10^8 cells resuspended in 500 ul FACS buffer. MACS of TANs, defined as CD66B$^+$ cells, was performed with LS columns (Miltenyi, cat. no. 130-042-401) according to the manufacturer's protocol.

Reactive oxygen species (ROS) detection

Isolated PBNs were resuspended at 5 x 10^6 cells/ml in starved media (DMEM-F12 w/o phenol red, Gibco, 21041-025) and 1 x 10^4 murine PBN/TANs were plated in 100ul serum-starved media in a white flat bottom 96-well plate (ThermoFisher, 136101). For human HD and patient PBNs 5 x 10^5 cells were plated in 100 ul per well. For human PBN/TAN co-cultures, 5 x 10^4 neutrophils were plated per well and CD66B$^-$ TME cells were added at a ratio 5:1 in 100 ul final volume. Luminol (Sigma, A8511-5G) was added to a final concentration of 100 uM. Inhibition of ROS production by PBNs was achieved by adding diphenyleneiodonium chloride (DPI, Sigma, D2926-10mg) at a final concentration of 50 uM; stimulation of ROS production was achieved by adding phorbol-12-myristat-13-acetate (PMA, abcam, abb120297) at a final concentration of 4 uM. The plate was gently shaken prior to read-out by measuring all wavelengths in a luminescence plate-reader (Microplate reader Infinite® 200 PRO Tecan) at an interval of 5min for 2h.

T cell cytokine array

Peripheral CD3$^+$ T cells were isolated from patient whole blood using the Easy HLA Chimerism Whole Blood CD3 positive selection kit (Stemcell, cat. no. 17871) according to the manufacturer's protocol. 1 x 10^5 viable peripheral CD3$^+$ T cells or 2.5 x 10^5 viable CD66B$^-$ TME cells were plated in complete media in a flat bottom 96-well plate (Corning, cat. no. 3596), in the presence or absence of 1 x 10^5 PBNs/TANs in a final volume of 100ul. After 96 h, the plate was spun at 300G for 10 min, and the supernatant collected and frozen at -20°C until further use. Supernatants were thawed at 4°C and diluted 2x in Assay Diluent (MSD, cat. no K151AEL-1). A customized cytokine panel assay containing Granzyme B, IFN-γ and IL-12p70 (U-PLEX Immuno-Oncology Group 1 (hu) assay, MSD, Cat. no. K151AEL-1) was performed according to the manufacturer's instructions. Cytokine detection was performed using the MESO QuickPlex SQ120 instrument (Meso Scale Discovery).

Annexin V apoptosis analysis

PBNs were cultured with whole tumor MEC at a ratio of 1:1 in complete media (DMEM-F12 + 10% FBS + 1% P/S) at 37°C and 5% CO_2. Cells were collected after 24h or 48h and incubated in PBS with Human TruStain FcX Fc receptor blocking solution (FC block; 1:100) (BioLegend, cat. no. 422302) for 10 min at RT. The 2x concentrated FCM antibody mix was added to the cells for 15 min at 4°C in the dark (see key resources table for the antibodies used). Cells were washed with 1x binding buffer (Thermo Fischer Scientific, Cat no. 88-102-72) and stained with a 1:100 dilution of Annexin V-PE (Thermo Fischer Scientific, 88-102-72) in binding buffer. The cells were incubated for 15 min at RT in the dark, before washing in binding buffer. Cells were resuspended in binding buffer containing 2 ug/ml DAPI (Life Technologies, cat. no. D1306). Flow cytometric acquisition was performed within 4hrs after the staining.

UMAP and trajectory analysis

The manually gated PBN/TAN FCM population was exported as a separate FCS file. Variables with low variance were removed, data was randomly down-sampled to 50'000 events, and transformed (asinh(x)) using the R package scDataviz.[89] Dimensional reduction with UMAP as well as clustering analysis were performed using the monocle3 R package (v1.0.0).[91] Normalization was performed by size factor using principal component analysis. Unsupervised clustering was performed using the Leiden community detection method with the number of nearest neighbours (k) set to 100. Trajectory analysis was performed using the slingshot R package (v2.2.0).[92] Cluster 2 was selected as the origin. Multiple, disjoint trajectories were permitted by setting the omega parameter to TRUE.

Microenvironmental culture (MEC)-conditioned media (CM) collection and analysis

The generation and collection of whole-tumor microenvironmental culture-conditioned media (MEC-CM) from murine and patient tumors was performed as described in Maas et al.[23] (Module 3a). In brief, enzymatically dissociated tumor tissue was resuspended in complete media at a concentration of 2 x 10^6 cells/ml in a tissue culture flask and incubated at 37°C, 5% CO_2 and 95% humidity. CM was collected after 24h, spun for 10 min at 300 g, and stored at -80 °C until further use. For the generation of MEC-CM for ROS detection, media without phenol red was used. The immune landscape of MECs was characterized by FCM at 0h, 24h and 48h after the start of culture. Survival of immune populations over time was assessed by absolute viable cell counts using Trucount Absolute Counting Tubes (BD Biosciences, cat. no. 340334) by FCM. For detailed clinical information please see Table S1C.

Conditioned media (CM) generation from cell lines and primary cells

Tumor cell lines were derived from brain tumor MEC by passaging the cells at least 3 times prior to submission for validation by WES. Validated tumor cells were plated at 2 x 10^6 cells/ml in a tissue flask for the creation of CM. For detailed clinical information please see Table S1C.

HBMEC (ScienCell, Cat. no 1000) were cultured in Endothelial Cell Medium (ScienCell, 1001) and HA (ScienCell, Cat. no 1800) were cultured in Astrocyte Medium (ScienCell, 1801) in accordance with vendor's recommendations. HUVECs were cultured in DMEM-F12 (1:1) +GlutaMAX +10% FBS +1% P/S. Cells were passaged when 70% confluency was reached. 0.25% Trypsin was added to the plates and trypsinization was stopped by adding Trypsin Neutralization Solution (ScienCell, 0113) according to manufacturer's instructions.

Differentiated MDMs from healthy donors were generated as described above and harvested from Teflon-coated bags at day 7, followed by plating at a density of 1 × 10^6 cells/well of a 6-well plate in DMEM +10% FBS +1% P/S.

For all cell lines, media was changed to complete media (DMEM +10% FBS + 1% P/S) when 70% confluency was reached. The supernatant of tumor cell lines (TCM) and non-tumor-associated primary cell lines (non-TCM) was collected after 24h, spun at 300G for 10 min and stored at -80°C until further use.

CM education experiments

MEC-CM, TCM and non-TCM were thawed at RT. Isolated human PBNs from HD were resuspended in CM and plated at 1 x 10^6 cells/ml in U-bottom 96-well plates (Corning, Cat no. 3799). Isolated murine PBNs were resuspended in MEC-CM and plated at 5 x 10^5 cells/ml. HD PBN cultured in MEC-CM were treated with human TNF-α neutralizing antibody (10ug/ml, Cell Signaling Technologies, cat. no. 7321S), GLO-1 inhibitor (10mM, MedChemExpress, cat. no. HY-136684), anti-IL-6 (10ug/ml, R&D, cat. no. MAB206), or anti-IL-9 (10ug/ml, R&D, cat. no. AF209). Cells were incubated at 37°C and 5% CO_2, until they were collected for phenotypic characterization by FCM (after 5–6 h) and cell survival assessment at 24h and 48h. For the assessment of ROS detection by FCM, the readout was performed immediately.

Whole exome sequencing (WES)

WES of snap-frozen and OCT-embedded frozen tumor tissue was performed as described in Maas et al.[23] and Álvarez-Prado et al.[39] (Module 1b). Briefly, tumor tissue (minimum size 3 mm^3) was placed on aluminum foil and snap-frozen by directly dipping it in pre-cooled 2-methylbutane (Sigma-Aldrich, cat. no. 50970) placed in bucket containing liquid nitrogen. Frozen tissues were directly transferred in a cryovial and stored at -80°C until further use. Tumor pieces (~1-2 mm3) were placed into a 2 ml round-bottom micro-centrifuge tube and 600 ul RLT buffer (Qiagen DNAeasy Blood&Tissue kit, cat. no. 69504) was added. The tissue was disrupted and homogenized using an Omni Tissue Homogenizer with a 5-7 mm probe for 1-3 min. The lysate was incubated at 55 °C in a heat block for 1 h. For the validation of tumor cell lines by WES, a cell pellet of 1 x 10^6 tumor cells, as well as matched PBMCs, were resuspended

in 600 ul RLT buffer and incubated at 55°C in a heating block for 1h. Genomic DNA was extracted from frozen tumor tissue, PBMCs, and tumor cells following manufacturer's instructions (Qiagen DNAeasy Blood&Tissue kit, cat. no. 69504). Sequencing of paired end, 150 base pair (2 x 150), was performed by Genewiz (South Plainfield, New Jersey, USA) on an Illumina NovaSeq 6000 sequencer (Illumina). Somatic variant calling was performed from WES data of paired tumor/cell line and PBMC samples. Raw reads (*fastq* files) were quality-control checked by FastQC and sequencing adaptors were removed by cutadapt (v2.3).[93] The resulting reads were then aligned to the hg38 (GRCh38.95) reference genome using the Burrows-Wheeler aligner (v0.7.17).[94] Aligned reads were sorted and written into BAM alignment files using SAMtools (v1.8)[95] and marked for duplicates using Picard tools (v2.9.0). Somatic mutation calling was performed using MuTect2 from the GenomeAnalysisTK-4.1.0.0 (GATK4) and GATK Resource Bundle GRCh38 following best practices for somatic variant calling as described by The Broad Institute (https://gatk.broadinstitute.org/hc/en-us/articles/360035894731-Somatic-short-variant-discovery-SNVs-Indels-). Somatic variants were filtered to only retain confident calls by using the GenomeAnalysisTK FilterMutectCalls function. VCF files containing only "PASS" (filtered) variants were generated by using GenomeAnalysisTK SelectVariants (parameters: –exclude-filtered) and filtered variants were annotated using ENSEMBL Variant Effect Predictor (v96).[96]

Protein array

Frozen CM was submitted to RayBiotech Life and analyzed by the manufacturer's in-house service using L1000 Glass Slide Human Antibody Array (RayBiotech Life, cat. no. AAH-BLG-1000-4). The threshold for protein detection was set to a two-fold standard deviation of the negative control, and expression values were normalized to those from complete media (DMEM-F12 + 10% FBS + 1% P/S).

Recombinant protein treatment

Isolated HD PBNs were resuspended at a concentration of 1 x 10^6 cells/ml in complete media (DMEM + 10% FBS + 1% P/S), and 100 ul of the cell suspension was placed in a U-bottom 96 well plate (Corning, Cat no. 3799). Cells were treated with Ceruloplasmin (0.5uM, Sigma-Aldrich, cat. no. C4519-100UN), TNF-α (10 ng/ml, PeproTech, cat. no. 300-01A), GLO-1 (50μg/ml, R&D, cat. no. 4959-GL), IL-6 (5ng/ml, Sigma-Aldrich, cat. no. SRP3096), and IL-9 (5ng/ml, R&D, cat. no. 209-ILB). For the measurement of phenotypic alterations using FCM, cells were incubated for 5-6h at 37°C and 5% CO2. For the measurement of ROS by FCM cells were incubated for 30min at 37°C and 5% CO2.

Software and visualization

FCM data was analyzed using FlowJo (v10.8.2). Graphs and plots were generated using either the ggplot2 (v3.3.6)[90] R package or GraphPad Prism (v9.4.1). Heatmaps were created using the ComplexHeatmap (v2.10.0)[97] R package. The protein interaction network was generated using the STRING platform (https://string-db.org)[77] and visualized with iGraph (v1.2.6)[98] R package.

QUANTIFICATION AND STATISTICAL ANALYSIS

All biostatistics analysis were performed within R (v4.1.1). Data was analyzed with the statistical test described in the corresponding figure legend. The 'n' value and the use of median and standard deviation (SD) values are defined in the accompanying figure legend. Mixed effect model calculations were performed with the R packages lme4 (v1.1-32)[99] and lmerTest (v3.1-3).[100] Statistical significance was depicted as the p-value for single comparisons and p.adj value for multiple comparisons unless otherwise stated: * <0.05, ** <0.01, *** <0.001, **** <0.0001, ns >0.05. P.adj values were obtained by correcting for multiple testing using the Benjamini-Hochberg method, unless otherwise stated.

CellPress
OPEN ACCESS

Supplemental figures

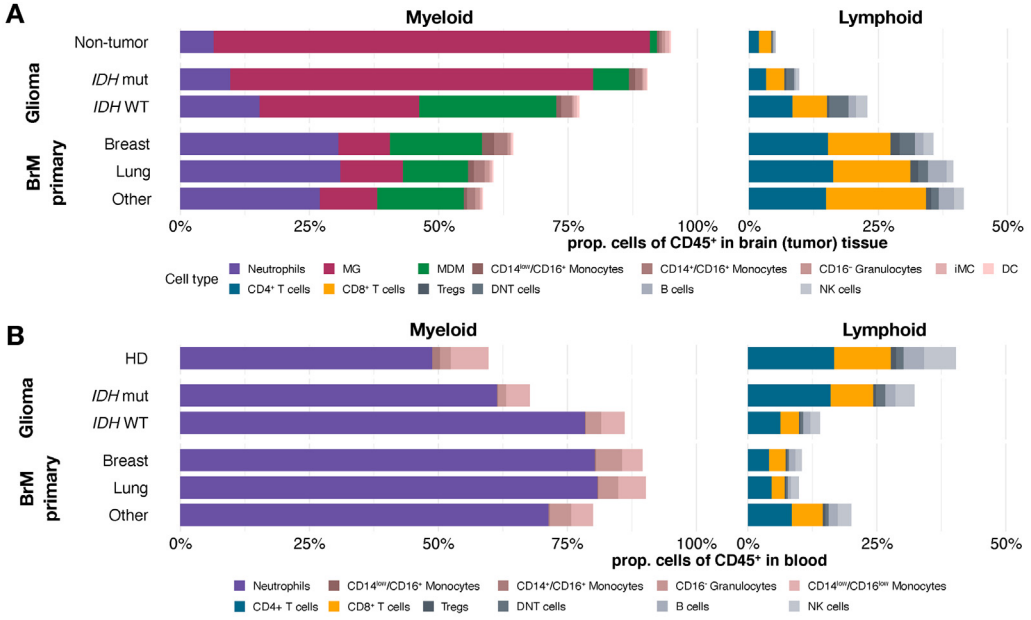

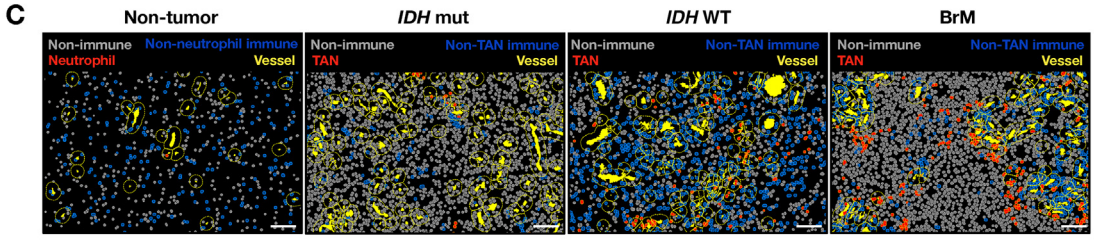

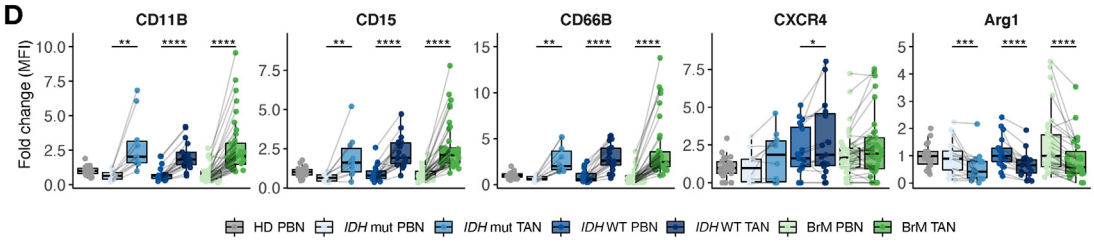

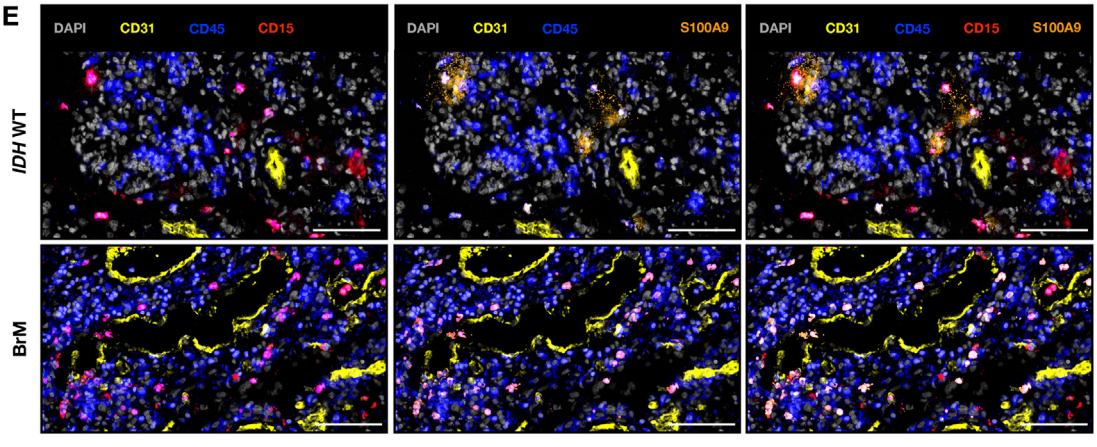

(legend on next page)

Figure S1. Neutrophil abundance in blood and brain tumor microenvironment and their phenotypic alterations, related to Figure 1

(A) Mean proportions of all $CD45^+$ immune cell populations in non-tumor (n = 11) and tumor tissue ($n_{IDH\ mut}$ = 31, $n_{IDH\ WT}$ = 70, $n_{Breast\text{-}BrM}$ = 15, $n_{Lung\text{-}BrM}$ = 41, $n_{Other\text{-}BrM}$ = 24) based on flow cytometry (FCM). Microglia (MG), monocyte-derived macrophages (MDMs), immature monocytes (iMCs), dendritic cells (DCs), T regulatory cells (Tregs), double negative T cells (DNT cells).

(B) Mean proportions of $CD45^+$ immune cells in whole blood from healthy donors (HD; n = 12) and brain tumor patients ($n_{IDH\ mut}$ = 20, $n_{IDH\ WT}$ = 43, $n_{Breast\text{-}BrM}$ = 8, $n_{Lung\text{-}BrM}$ = 25, $n_{Other\text{-}BrM}$ = 17) based on FCM.

(C) Cell-type identification of TANs ($CD45^+$,$CD15^+$), non-TAN immune cells ($CD45^+$,$CD15^-$), non-immune ($CD45^-$) and vessels ($CD31^+$) on tissues as shown in Figure 1E. Dashed yellow line indicates the border of the perivascular niche (PVN), corresponding to a 20 μm distance surrounding the vessel.

(D) Fold-change median fluorescence intensity (MFI) with SD of the indicated markers in matched PBNs and TANs from tumor-bearing patients ($n_{IDH\ mut}$ > 10, $n_{IDH\ WT}$ = 19, n_{BrM} > 31) normalized to HD PBNs (n > 14). Wilcoxon signed-rank test of matched patient neutrophils only. p.adj values: *p < 0.05, **p < 0.01, ***p < 0.001, ****p < 0.0001.

(E) Representative IF images of immune cells ($CD45^+$,$CD15^-$), neutrophils ($CD45^+$,$CD15^+$), and vessels ($CD31^+$) and their expression of S100A9 in *IDH* WT glioma and lung-BrM tissue. Scale bars: 100 μm.

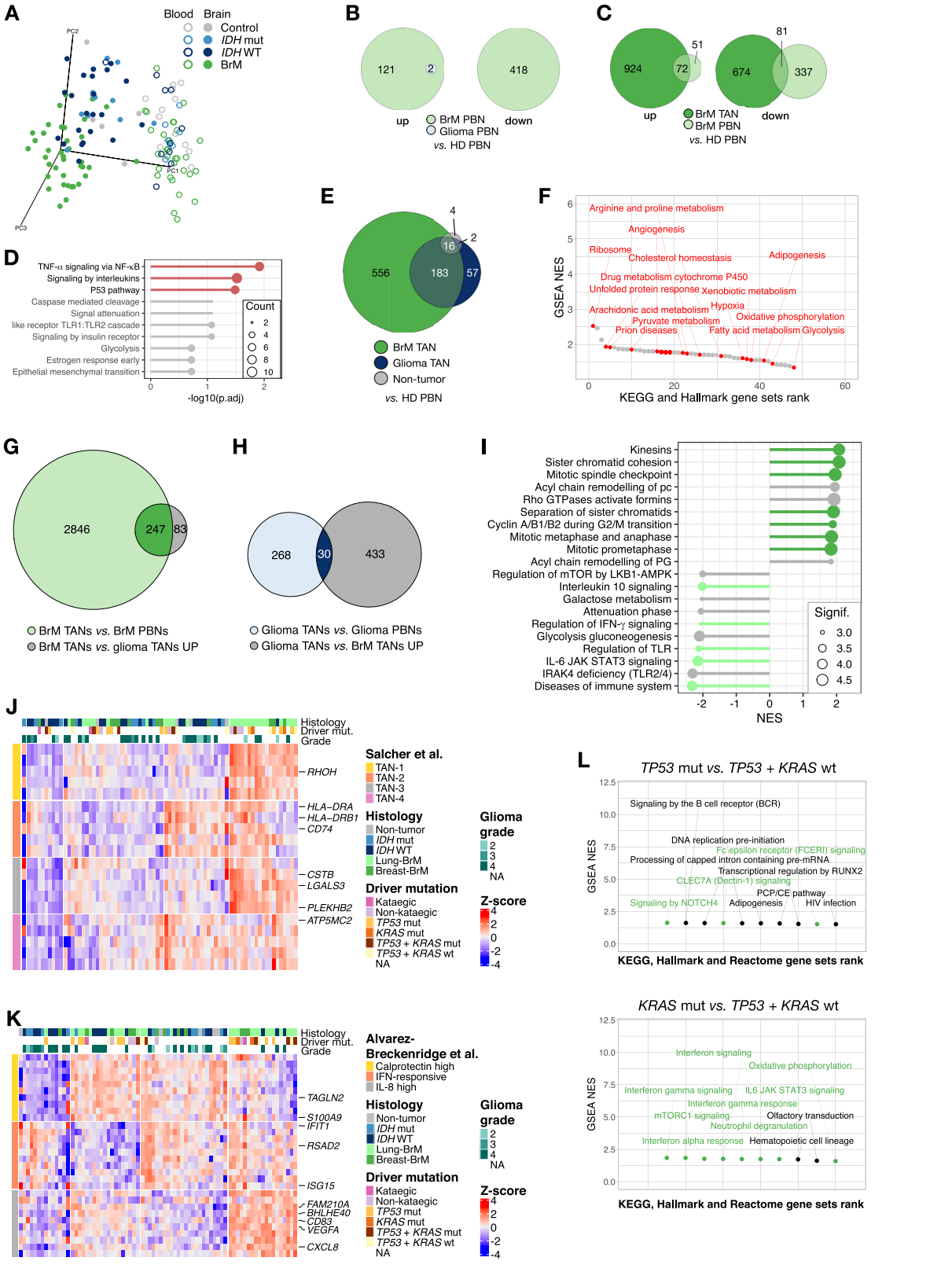

(legend on next page)

Figure S2. Neutrophils in human brain (tumor) tissue differ substantially from PBNs, related to Figure 2

(A) Principal component (PC) plot of neutrophil transcriptional profiles in blood (empty circles) and brain (tumor) tissue (filled circles), based on 1% most variable genes.

(B) Euler diagram showing the (absence of) overlap of up- and downregulated differentially expressed genes (DEGs) in glioma and BrM vs. HD PBNs from Figure S2D (cutoff: p.adj < 0. 05; LFC > 1 or < −1).

(C) Euler diagram depicting the intersect of up- and downregulated DEGs in BrM TANs and PBNs vs. HD PBNs (cutoff: p.adj < 0.05; LFC > 1 or < −1).

(D) Over-representation analysis (ORA) of pathways from KEGG and Reactome databases on upregulated DEGs shared between BrM PBNs and TANs vs. HD PBNs.

(E) Euler diagram showing the intersect of downregulated DEGs in BrM and glioma TANs, and non-tumor brain neutrophils vs. HD PBNs (cutoff: p.adj < 0.05; LFC < −1).

(F) Rank plot of gene set enrichment analysis (GSEA) using KEGG and Hallmark databases of non-tumor brain neutrophils vs. HD PBNs from (Figure 2C) (cutoff: p.adj < 0.05; NES > 0).

(G) Euler diagrams depicting the intersect of BrM vs. glioma TANs and BrM TANs vs. matched PBNs (cutoff: p.adj < 0.05; LFC > 1 or < −1).

(H) Euler diagrams depicting the intersect of glioma vs. BrM TANs and glioma TANs vs. matched PBNs (cutoff: p.adj < 0.05; LFC > 1 or < −1).

(I) Top 10 significant GSEA pathways using Hallmark, KEGG, and Reactome databases on DEGs in lung- vs. breast-BrM TANs. (cutoff: p.adj < 0.05; −1.5 > NES > 1.5). Highlighted in light green are lung-BrM TAN specific pro-inflammatory pathways, highlighted in dark green are breast-BrM TAN specific cell-cycle-associated pathways.

(J and K) (J) Heatmap depicting non-tumor neutrophils and brain TANs aligned to the top 5 most variable genes per cluster as defined by the Salcher[37] and (K) the top 10 most-variable genes per cluster as defined by the Alvarez-Breckenridge single cell RNA-seq dataset.[38] Genes of interest are indicated on the right. Samples were hierarchically clustered.

(L) GSEA using Hallmark, KEGG and Reactome databases to analyze DEGs in TANs isolated from *KRAS* mut vs. WT and, *TP53* mut vs. WT lung-BrM (cutoff: p.adj < 0.05; −1.5 > NES > 1.5). Pathways of interest are highlighted in green.

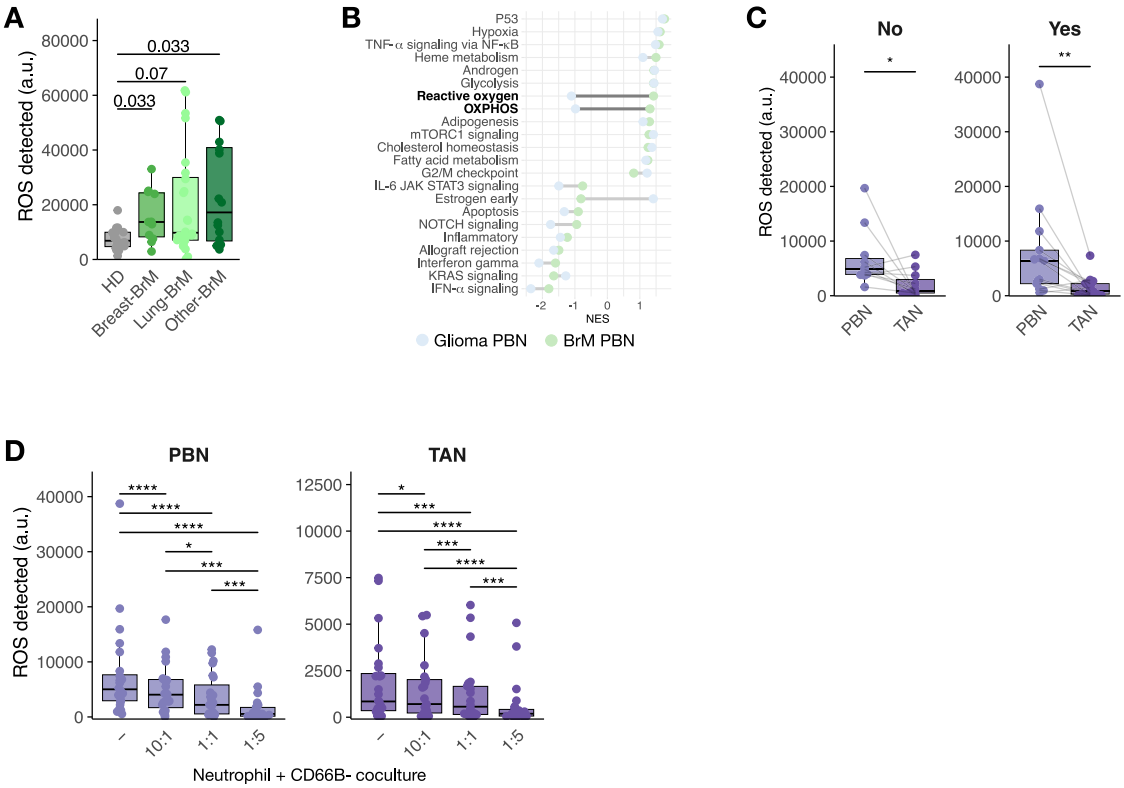

Figure S3. ROS levels are altered in human BrM PBNs and brain-TAN, related to Figure 3

(A) Reactive oxygen species (ROS) detected in PBNs from HD (n = 18), and BrM-bearing patients ($n_{Breast\text{-}BrM}$ = 11, $n_{Lung\text{-}BrM}$ = 24, $n_{Other\text{-}BrM}$ = 16). Wilcoxon rank-sum test. p.adj value as indicated.

(B) GSEA based on Hallmark database in glioma and BrM PBNs vs. HD PBNs. ROS-related pathways are highlighted in dark gray (cutoff: p value < 0.05).

(C) Detected ROS in matched PBNs and TANs, stratified by the absence "No" ($n_{IDH\ mut}$ = 5, $n_{IDH\ WT}$ = 5, n_{BrM} = 1) or presence "Yes" ($n_{IDH\ mut}$ = 1, $n_{IDH\ WT}$ = 4, n_{BrM} = 8) of previous oncologic treatment (e.g., immunotherapy, radiotherapy, chemotherapy, targeted therapy, hormone therapy, surgery, or corticosteroids). Wilcoxon signed-rank test, p value: *p < 0.05, **p < 0.01.

(D) Neutrophil ROS production in a titrated coculture with $CD66B^{-}$ TME population ($n_{IDH\ mut}$ = 6, $n_{IDH\ WT}$ = 9, n_{BrM} = 9). Wilcoxon signed-rank test. p.adj value: *p < 0.05, ***p < 0.001, ****p < 0.0001. Data in (A), (C), and (D) are represented as mean ± SD.

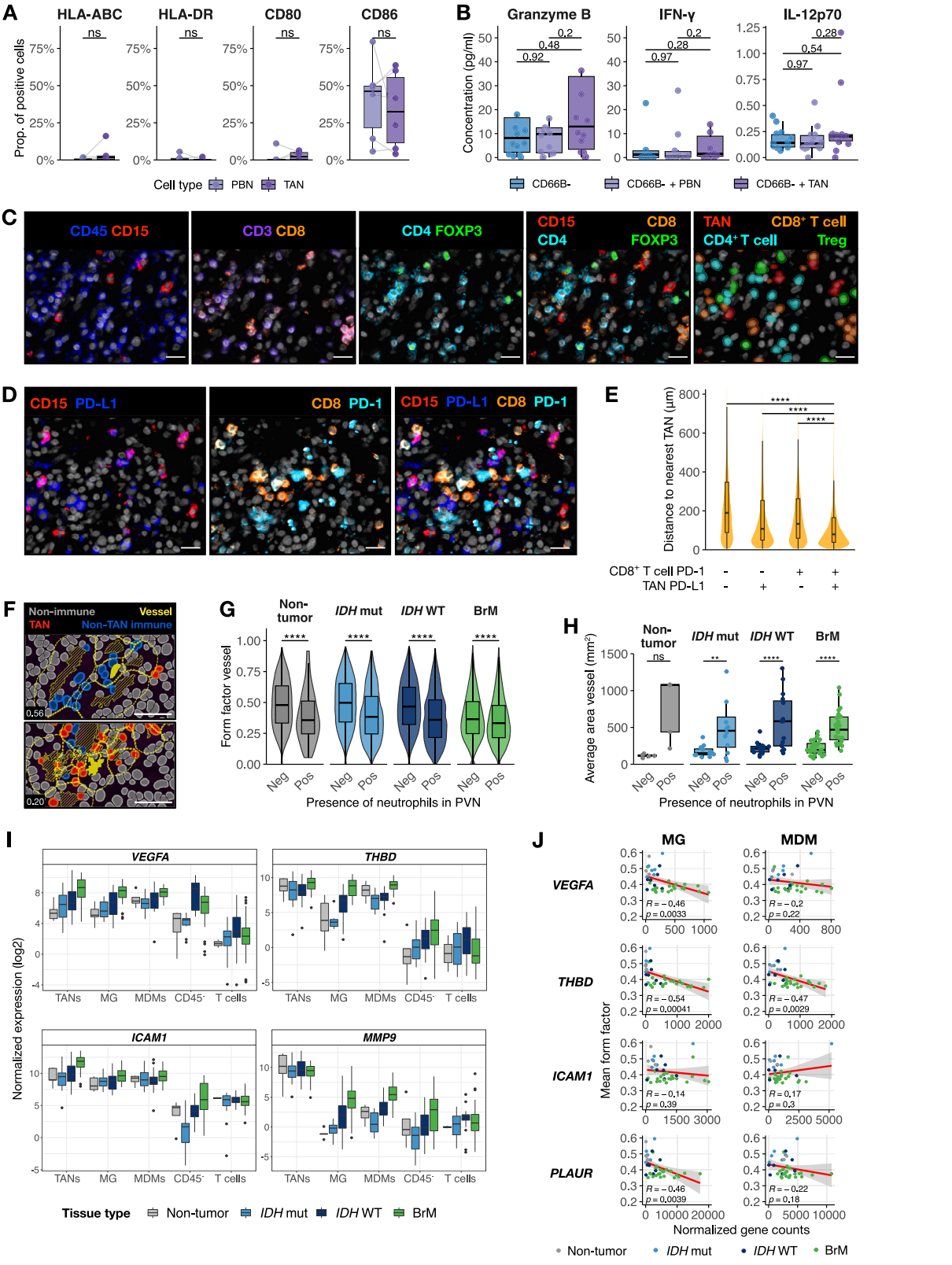

(legend on next page)

Figure S4. Brain TANs do not have evident T cell stimulatory capacity and reside in close proximity to deformed vessels, related to Figure 4

(A) Proportion of cells expressing markers associated with antigen presentation in matched PBNs and TANs ($n_{IDH\ WT} = 4$, $n_{BrM} = 2$). Wilcoxon signed-rank test.

(B) Cytokine concentration (pg/mL) in supernatant of $CD66B^-$ cells cocultured with either PBNs or TANs for 96 h ($n_{IDH\ mut} = 1$, $n_{IDH\ WT} = 7$, $n_{BrM} = 6$). Wilcoxon signed-rank test, p.adj values as shown.

(C) Representative IF images and cell type quantification of T cells and TANs in a lung-BrM, with cell type-specific identification of TANs ($CD45^+$,$CD15^+$), $CD8^+$ T cells ($CD45^+$,$CD3^+$,$CD4^-$,$CD8^+$), $CD4^+$ T cells ($CD45^+$,$CD3^+$,$CD4^+$,$CD8^-$,$FOXP3^-$) and Tregs ($CD45^+$,$CD3^+$,$CD4^+$,$CD8^-$,$FOXP3^+$).

(D) Representative IF images and cell type quantification of $CD8^+$ T cells ($CD45^+$,$CD3^+$,$CD8^+$), TANs ($CD45^+$,$CD15^+$), PD-L1 and PD-1 in a lung-BrM sample, corresponding to the quantification shown in Figure 4E. Scale bars in (C) and (D): 20 μm.

(E) Distance of individual $CD8^+$ T $cells_{(n\ =\ 54,495)}$ to TANs stratified by their respective expression of PD-1 and PD-L1 ($n_{BrM} = 20$, $n_{IDH\ WT} = 7$ analyzed together). Wilcoxon rank-sum test.

(F) Representative lung-BrM IF images of vessels ($CD31^+$); inserts on the lower left of each image show the form factor value of the highlighted vessel. Scale bars: 50 μm.

(G) Form factor of individual vessels grouped by absence (Neg, $n_{Non\text{-}tumor} = 35,078$, $n_{IDH\ mut} = 54,015$, $n_{IDH\ WT} = 62,261$, $n_{BrM} = 79,225$) or presence (Pos, $n_{Non\text{-}tumor} = 67$, $n_{IDH\ mut} = 1,630$, $n_{IDH\ WT} = 2,745$, $n_{BrM} = 37,242$) of neutrophils in the PVN from non-tumor (n = 5) and tumor tissue ($n_{IDH\ mut} = 12$, $n_{IDH\ WT} = 15$, $n_{BrM} = 27$). Wilcoxon signed-rank test.

(H) Mean vessel area in mm^2 stratified by the presence of neutrophils in the PVN on the same dataset shown in (G). Wilcoxon signed-rank test.

(I) Normalized log_2-transformed gene expression of pro-angiogenic genes across the major TME populations.

(J) Correlation between mean vessel form factor vs. normalized gene counts of angiogenesis-associated genes in non-tumor, glioma, and BrM MG and MDMs using the Pearson method. p.adj values in (A), (E), (G), and (H): $^{**}p < 0.01$, $^{***}p < 0.001$, $^{****}p < 0.0001$. Data in (A), (B), (E), and (G)–(I) are represented as mean ± SD.

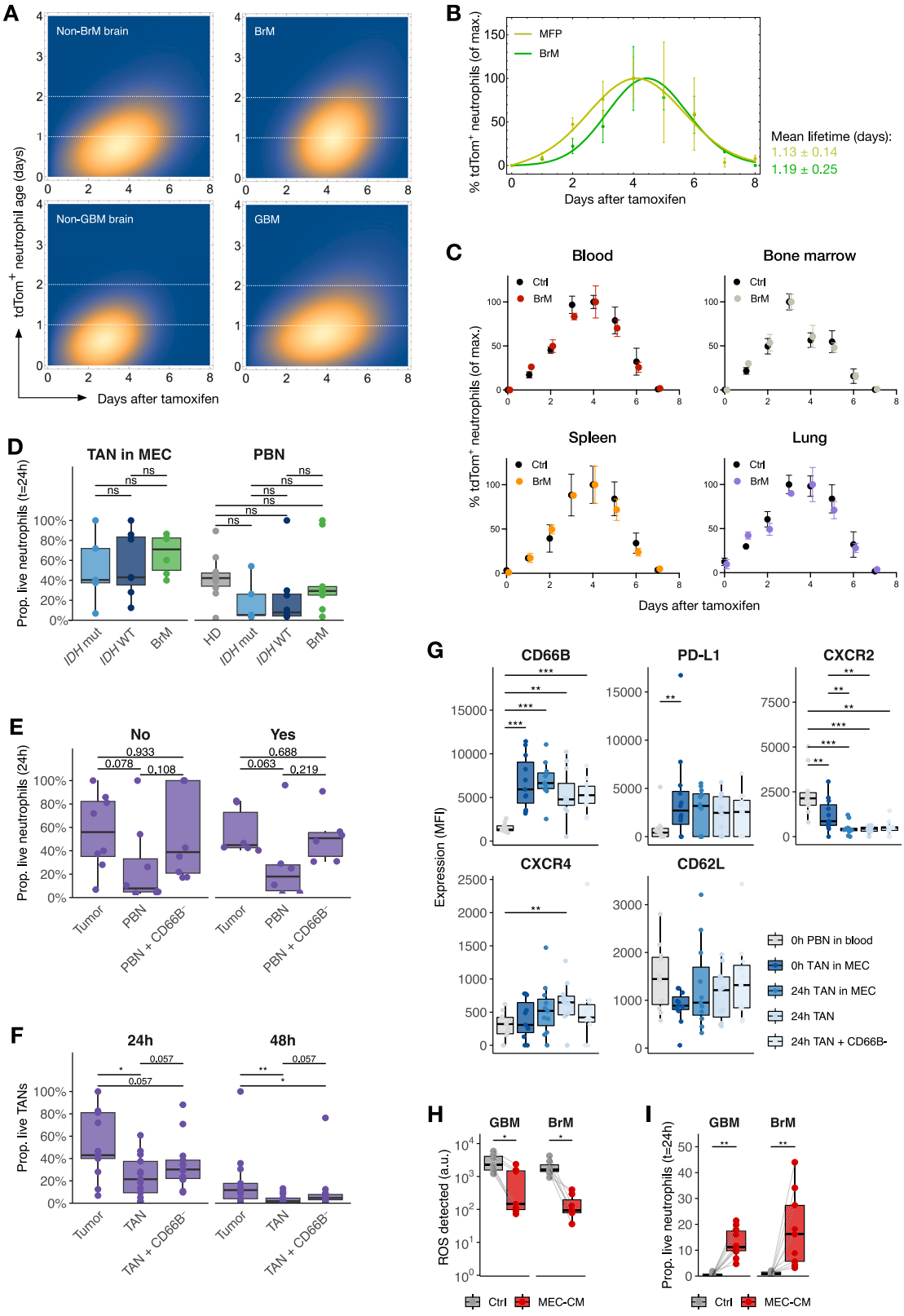

(legend on next page)

Figure S5. Phenotypic and lifespan alterations of TANs result from a combination of cell-intrinsic and microenvironment-mediated effects, related to Figure 5

(A) Density plots of the age distribution of mouse neutrophils in Ntv-a;iLy6G^{tdTomato} non-tumor brain and GBM as well as iLy6G^{tdTomato} non-tumor bearing brain and BrM mouse models over time.

(B) The proportion of tdTom^{+} neutrophils using iLy6G^{tdTomato} reporter mice normalized to the maximum in primary tumor-bearing mice (mammary fat pad [MFP] injection of the PyMT-BrM3 cell line) and BrM-bearing mice over an 8 day time course. A minimum of 3 mice from 6 independent experiments are shown per time point. Mean lifetime in days is shown on the right.

(C) Proportion of tdTom^{+} neutrophils normalized to the maximum in a series of different non-brain tissues isolated from non-tumor (Ctrl) and BrM-bearing iLy6G^{tdTomato} mice over 8 consecutive days. A minimum of 3 mice are shown per time point from 6 individual experiments.

(D) 24 h survival of patient TANs ($n_{IDH\ mut} = 5$, $n_{IDH\ WT} = 7$, $n_{BrM} = 6$), PBNs from HD (n = 10) and patient PBNs ($n_{IDH\ mut} = 5$, $n_{IDH\ WT} = 8$, $n_{BrM} = 9$). Wilcoxon rank-sum test.

(E) Proportion of live neutrophils after 24 h in whole tumor, PBNs and PBNs cocultured with CD66B^{-} TME stra PBNs and TANs, stratified by the absence "No" ($n_{IDH\ mut} = 4$, $n_{IDH\ WT} = 3$, $n_{BrM} = 1$) or presence "Yes" ($n_{IDH\ mut} = 1$, $n_{IDH\ WT} = 2$, $n_{BrM} = 3$) of previous oncologic treatment (e.g., immunotherapy, radiotherapy, chemotherapy, targeted therapy, hormone therapy, surgery, or corticosteroids). Wilcoxon signed-rank test, p.adj values as shown.

(F) Proportion of live TANs in matched whole tumor, isolated TANs and in coculture with CD66B^{-} TME populations after 24 and 48 h. Wilcoxon signed-rank test.

(G) MFI of neutrophil markers in PBNs in whole blood vs. TANs over time and in the presence of the CD66B^{-} TME ($n_{IDH\ mut} = 4$, $n_{IDH\ WT} = 5$, $n_{BrM} = 4$). Wilcoxon signed-rank test.

(H) Detected ROS in murine PBNs (n = 7) cultured in regular media (Ctrl) vs. MEC-CM from mouse GBMs or BrMs. Wilcoxon signed-rank test.

(I) Proportion of live murine PBNs after 24 h culture in regular media (Ctrl) vs. MEC-CM from mouse GBMs (n = 10) and BrM (n = 9). Wilcoxon signed-rank test. Data in (B)–(I) are represented as mean ± SD. p.adj values in (D), (F), and (G): ns > 0.05, *p < 0.05, **p < 0.01, ***p < 0.001. p value in (H) and (I): *p < 0.05, **p < 0.01.

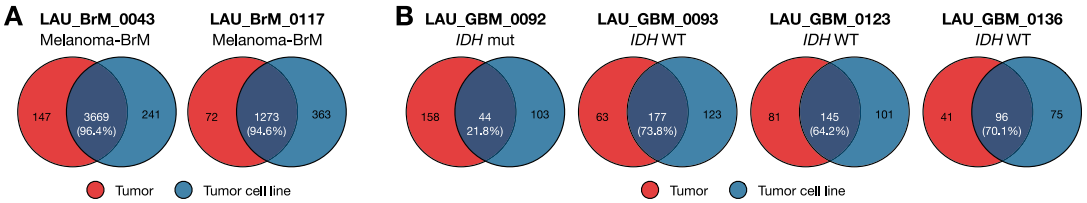

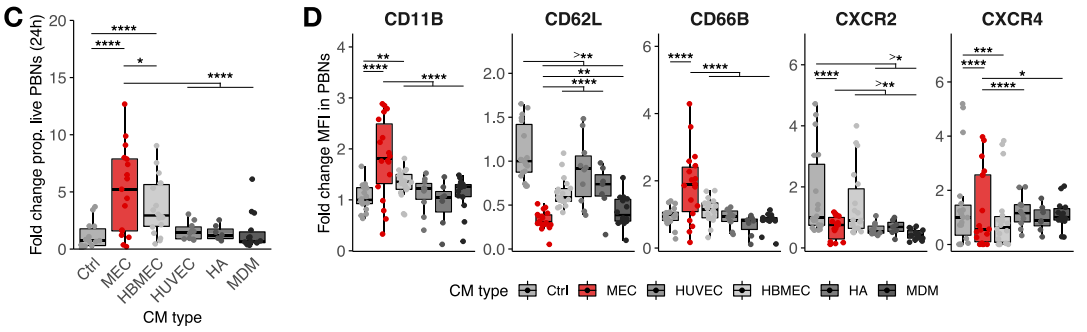

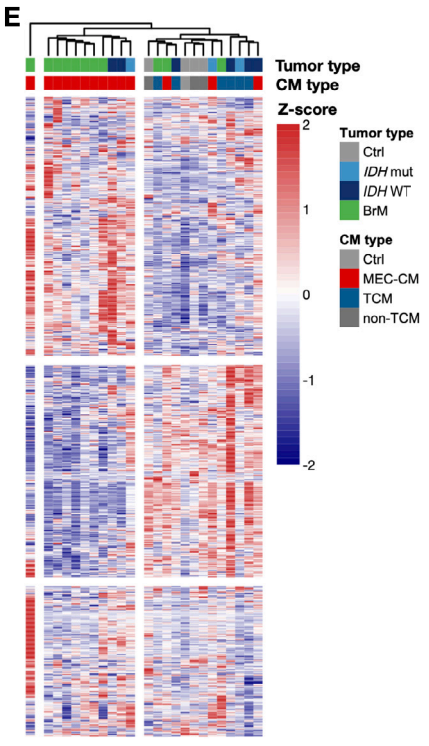

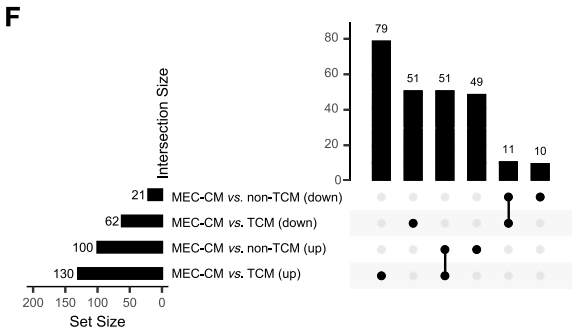

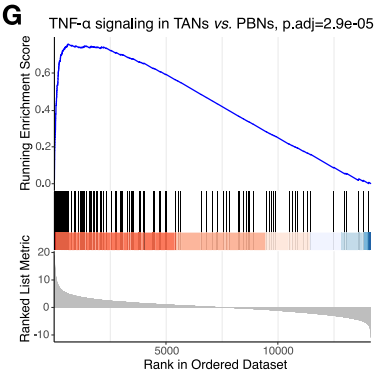

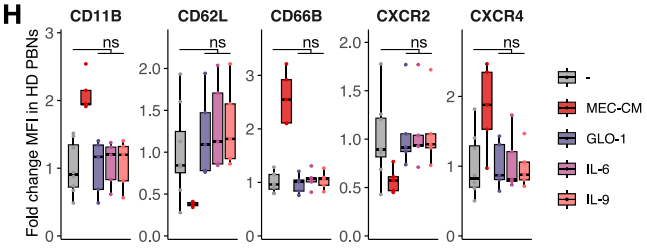

(legend on next page)

Figure S6. The brain TME is a rich source of soluble factors which alter neutrophil phenotype and lifespan, related to Figure 6

(A) Venn diagrams of somatic mutations identified by whole exome sequencing (WES) in matched BrM MEC and tumor cell lines (n = 2).

(B) Venn diagrams of somatic mutations identified by WES of *IDH* mut (n = 1) and *IDH* WT gliomas (n = 3) matched MEC and tumor cell lines.

(C) Fold-change in 24 h survival of HD PBNs (n = 25) cultured in conditioned media (CM) of tumor naive cell lines (non-TCM; $n_{HBMEC,\ HUVEC,\ HA} = 1$, $n_{MDM} = 3$) vs. control medium and MEC-CM ($n_{MEC} = 6$). Mixed-effect model using CM type as fixed effect and HD ID as random effect: ANOVA p value = 2.941×10^{7}.

(D) Fold-change MFI of the indicated proteins in HD PBN (n = 12) cultured for 6 h in CM ($n_{MEC} = 6$, $n_{HBMEC,\ HUVEC,\ HA} = 1$, $n_{MDM} = 3$) vs. control medium and MEC-CM. Mixed-effect model as in (C).

(E) Unsupervised heatmap of proteins detected in brain tumor MEC-CM, tumor cell-conditioned media (TCM), non-TCM, and control media. The sample outlier is breast-BrM LAU_BrM_0092, which was not characterized by any evident difference compared with other samples based on known clinical parameters, see also Table S1C.

(F) Visualization of differentially detected proteins in glioma and BrM MEC-CM vs. TCM and non-TCM. The unique $n_{proteins}$ found in individual groups and intersects are indicated on top of the bars (cutoff: $p < 0.05$).

(G) GSEA of TNF-α signaling pathways in glioma and BrM TANs compared with matched PBNs.

(H) Fold-change MFI of indicated markers measured in HD PBNs (n = 5) cultured in MEC-CM or treated with MEC-CM specific soluble factors. Wilcoxon signed-rank test. Data in (C), (D), and (H) are represented as mean ± SD, p.adj values: *$p < 0.05$, **$p < 0.01$, ***$p < 0.001$, ****$p < 0.0001$.

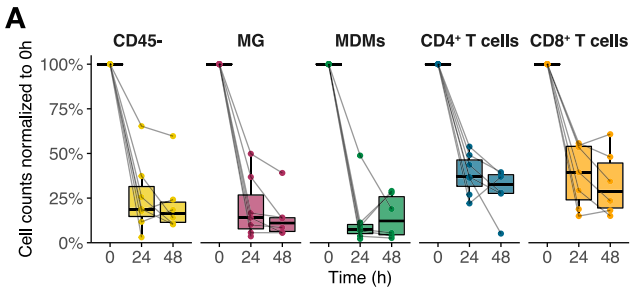

Figure S7. Survival of MEC populations in *ex vivo* culture, related to Figure 7

Normalized survival in % (compared with 0 h, mean ± SD) of microenvironmental culture (MEC) populations over time in culture ($n_{IDH\ mut} = 1$, $n_{IDH\ WT} = 3$, $n_{BrM} = 3$).